2019

Characterization of Rare-earth Doped Thermal Barrier Coatings for Phosphor Thermometry

Quentin Fouliard
University of Central Florida

CHARACTERIZATION OF RARE-EARTH DOPED THERMAL BARRIER COATINGS FOR PHOSPHOR THERMOMETRY

by

QUENTIN FOULIARD
B.S. École Polytechnique de l'Université de Nantes, 2014
M.S. École Polytechnique de l'Université de Nantes, 2016

A dissertation submitted in partial fulfillment of the requirements
for the degree of Doctor of Philosophy
in the Department of Mechanical and Aerospace Engineering
in the College of Engineering and Computer Science
at the University of Central Florida
Orlando, Florida

Fall Term
2019

Major Professor: Seetha Raghavan

ABSTRACT

Thermal Barrier Coatings have been extensively used to protect and insulate the metallic components in turbine engines from extreme environments to achieve higher turbine inlet temperatures, resulting in an increase in combined engine cycle efficiency, lowering NOx emissions and fuel consumption. Additionally, as the major failure mechanisms determining lifetime are thermally activated during engine operation, uncertainty in temperature measurements affects lifetime prediction. Early detection of Thermal Barrier Coatings spallation symptoms, associated with local delamination induced temperature changes, can reduce forced engine outages. Further improvements are envisioned with the development of more reliable measurement techniques. For this purpose, Phosphor Thermometry has been considered a promising method for precision monitoring of turbine blade coatings that contain embedded phosphor dopants. In this work, a modified four-flux Kubelka-Munk model for luminescent rare-earth doped Thermal Barrier Coating configurations supported the design and the fabrication of viable sensing coatings for potential industrial implementation. Phosphor Thermometry instrumentation was developed with the objective of expanding capabilities of the technique, using a synchronized

acquisition method on sensing coatings. Experiments on an innovative Erbium-Europium co-doped Yttria-Stabilized Zirconia coating have demonstrated the effectiveness of this advanced Phosphor Thermometry instrument with enhanced sensitivity and extended temperature range. Delamination progression monitoring was achieved for the first time using a Thermal Barrier Coating configuration subjected to indentation that includes a thin luminescent layer deposited on the surface and associating the multi-layer configuration with a predictive model that evaluates the advancement of the degradation of the coatings. To further ensure the integrity of the phosphor doped coatings, synchrotron X-ray diffraction was performed to characterize the specific residual strains and thermal expansion of the materials, determining mechanical robustness and compatibility with state-of-the-art Thermal Barrier Coatings. The outcomes of this work pave the way for *in-situ* temperature measurements on phosphor-doped turbine blade coatings with increased performance and accuracy.

This dissertation is dedicated to my grand parents who always believed that I could accomplish my biggest dreams. I will remember you forever.

ACKNOWLEDGMENTS

This dissertation is the product of the excellent support and guidance provided by my advisor, Dr. Seetha Raghavan. I would like to thank you for the experience and the great opportunities: Ambition, dedication and energy are the keys for success. My great recognition goes to Dr. Ranajay Ghosh, for the exceptional skills and for the valuable advice that you shared with me during my Ph.D. My sincere acknowledgments to Dr. Raj Vaidyanathan and Dr. Axel Schülzgen for being part of my committee.

My appreciation to the U.S. Department of Energy, National Energy Technology Laboratory, University Turbine Systems Research (UTSR): DE-FE00312282, for the financial support which gave me the chance to lead fascinating projects and high-impact research work throughout my entire Ph.D.

I would like to ackowledge my industry collaborators: Dr. Bauke Heeg (Lumium), for the great expertise with the instrumentation; Dr. Jeffrey Eldridge (NASA Glenn) and Dr. Douglas Wolfe (Penn State University) for the procurement of lumienscent samples to assess the developed models; Dr. Ramesh Subramanian (Siemens Energy) for the discussions and materials; Dr. Ed Hoffmann (GE aviation) and Joshua Salisbury (GE Global

Research) for the excellent support and guidance; Dr. Mary McCay, Frank Accornero and David Moreno (FIT Applied Research Laboratory) for the amazing help in the complex manufacturing process; Dr. Jonathan Almer and Dr. Jun Sang-Park (Argonne National Laboratory) for the valuable assistance with synchrotron experiments.

A special word to my friend, Dr. Alejandro Carrasco, for the inspiration and unconditional friendship. A particular attention to Estefania Bohorquez, for the caring and the strength that you gave me along the way. A huge thank you to Johnathan Hernandez, Matthew Northam, Valentin Baudrier, Corentin Piveteau, Pierre-Alexandre Jan, Manon Guyon and Muriel Talour for your encouragements during this journey. This herculean work would have been way more tedious without you all.

Finally, my greatest gratitude goes to my loving family, for your inestimable support, despite the distance, over the past few years.

TABLE OF CONTENTS

LIST OF FIGURES

LIST OF TABLES

CHAPTER 1
THERMAL BARRIER COATINGS

1.1 Introduction

1.1.1 Purpose and benefits

Efficiency of gas turbine systems has been increased since the apparition of turbine engines through the development and the optimization of advanced turbine blade configurations. The constituting superalloy materials compositions were optimized to better resist high-temperature oxidation. Thermal Barrier Coatings (TBCs), combined with air cooling tremendously boosted the thermal capabilities of the high-pressure turbine for operating the engines at higher turbine inlet temperatures [7, 8, 9], consequently lowering fuel consumption and NOx emissions [10, 11]. Both power generation and aeroengines have benefited from TBCs, that were proven to be very efficient for the insulation of the metallic components from the combustion gases, limiting creep, oxidation and thermal fatigue. TBCs protect turbine blades against extreme environments, allowing for greater efficiencies and extended lifetime of the engines. Figure 1.1 shows the location of the

TBC on the turbine blades in a typical aeroengine, in this case, on one of the most recent aircraft reactor from General Electric: the GE9X high-bypass turbofan, that is expected to equip the Boeing 777X starting in 2020.

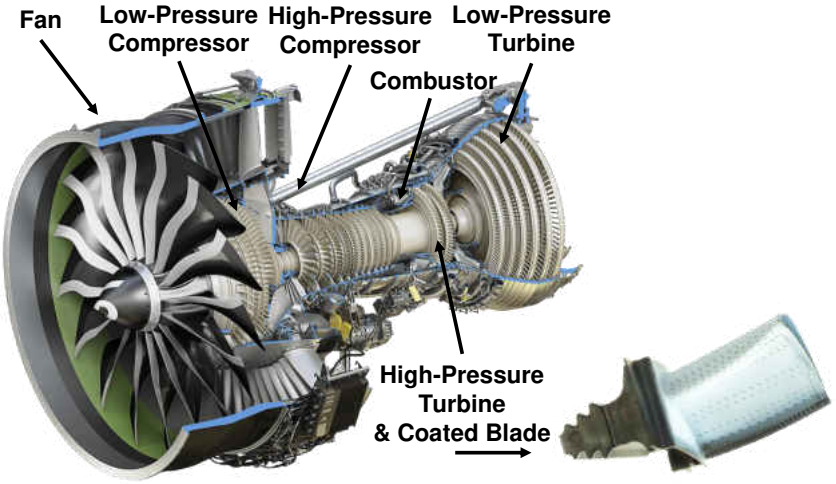

Figure 1.1: Cutout of a General Electric GE9X turbofan engine and turbine blade protected by a TBC.

The pressures and temperatures in a typical high-bypass turbofan were estimated using non-ideal isotropic equations for a 1D approximation of the extreme environment conditions, using a flight speed of Mach 0.9 and an altitude of 10 km [12]. The results are presented in Table 1.1. The harsh environment present in the high-pressure turbine, which corresponds to the location where TBCs are exposed to the highest temperatures and pressures, generally exceeds 1500°C and 20 bar. The temperature at the top surface of TBCs,

after being reduced by the air cooling film that covers turbine blades, is of the order of 1200 to 1400°C in this section of the turbomachinery [13, 14, 15, 16]. The very low thermal conductivity of the ceramic top coat allows an additional 150 - 200°C reduction through the TBC [17]. The race for increased performance of the engines forces the protective materials to operate close to their temperature limits, putting the mechanical properties of structural components at risk, which can eventually lead to rapid deterioration and failure [18].

Table 1.1: Estimated temperatures and pressures for a typical high-bypass turbofan at the inlet of each section of the turbine system.

Stage	**Inlet temperature (°C)**	**Inlet stagnation pressure (bar)**
Diffuser	-57	0.5
Compressor	-21	0.4
Combustor	817	24.1
Turbine	1727	23.1
Nozzle	1651	10.6

1.1.2 General structure of TBCs

TBCs are produced by the successive deposition of two layers on a prepared superalloy substrate. Figure 1.2 presents the general structure of TBCs. It can be noted that the top coat shown in this graph has a microstructure that is typical for aeroengine applications [19]. The ceramic top coat ensures thermal insulation of the underlying bond coat and

substrate materials [20]. The metallic bond coat is used to ensure good adhesion of the thermally protective ceramic layer, that is deposited at the top of the multilayered structure, to the substrate. The bond coat is also oxidation and hot corrosion resistant [21, 22]. During operation, the bond coat is further defended against oxidation through the passivation of the β-NiAl phase that creates an Al_2O_3 Thermally Grown Oxide (TGO) layer that is thermodynamically compatible with the top coat. The TGO forms from the reaction of aluminum and oxygen at the interface between the top coat and the bond coat and acts as a diffusion barrier. The thickness of this TGO increases following a logarithmic trend with time [23, 24, 25], due to the very low oxygen and aluminum diffusion into the TGO [26], that limits its maximum growth to a few microns. This trend was found to be due to a combination of factors including progressive transformation of Al_2O_3 isoforms to the stable α-Al_2O_3, the increase of the oxide grain size, and compressive stress that decreases the diffusion rate of vacancies [27]. The TGO generally extends further at its interface with the bond coat and the growth rate is controlled by the diffusion of oxygen through the oxide layer. Other TGO growth mechanisms, although less prominent, include the outward formation of TGO at the interface between the top coat and the TGO or at the TGO grain boundaries.

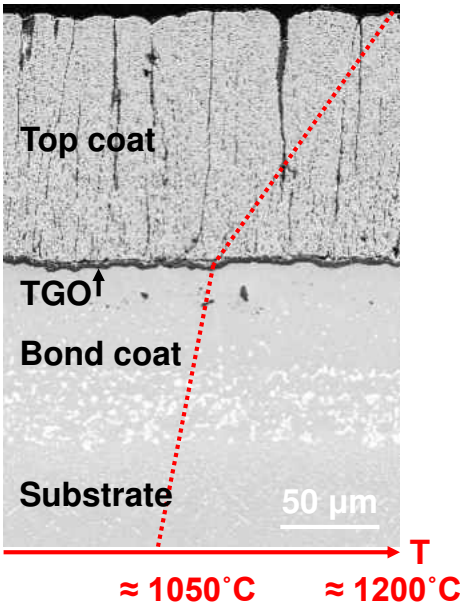

Figure 1.2: Typical TBC structure which allows a 150°C drop through the ceramic top coat.

1.2 Main materials and methods

1.2.1 Standard materials

The state-of-the-art TBC top coats are composed of 7-8 wt.% Yttria-Stabilized Zirconia (YSZ), chosen for its low thermal conductivity and high coefficient of thermal expansion [28]. Bond coats used for the production of TBCs include MCrAlY or Pt-aluminide compositions that are selected in function of the associated substrate and the deposition

method used for the overlying top coat, to ensure maximal corrosion and oxidation resistance as well as thermodynamic compatibility. Generally, Air Plasma Spray coatings are deposited onto MCrAlY bond coats and Electron Beam Physical Vapor Deposition coatings are deposited onto Pt-aluminide bond coats [29, 30]. For the substrate material that constitutes turbine blades, Nickel-based superalloys are commonly used and the specific composition depends on the application [31]. Continuous progress has been made to extend superalloy thermomechanical capabilities, resulting in overall improved oxidation and creep properties [32].

1.2.2 Air Plasma Spray (APS)

Air Plasma Spray is a versatile method used for the fast deposition of coatings, that is particularly appropriate for the deposition of coatings on large components with the possibility of using robotic arms to cover 3D areas. In this method, as it is described in Figure 1.3, a plasma torch releases both electrical and thermal energy to create as a powerful plasma jet [33]. The plasma temperature can exceed 10,000 K and the plasma flow velocity is around 10^3 m/s. Micron-size powder particles are injected and accelerated to velocities up to 30 - 500 m/s into the plasma jet [17], which result in their partial or full melting as they reach the substrate. The impact with the substrate flattens the

particles and they solidify rapidly, forming splat-like microstructures with a thickness in the range of 1 to 20 μm, often called lamellae [33] and a diameter of 200 to 400 μm [29]. The coating itself is then built as these lamellae pile up and spread laterally across the substrate surface or across the already-deposited particles. In practice, the APS method allows to control the deposition thickness with a precision level of the order of 20 μm, which makes it suitable for multilayer configurations. Generally, the thickness of APS coatings is comprised in the 100 - 3000 μm range. Millimeter-thick coatings allow for larger temperature gradients but are more likely to build up stress to critical levels due to the higher amount of elastic energy stored in the coating, which drives crack propagation [34]. Typical porosity for APS coatings is 3 - 20% and optimized values were found to be 14 - 15% [17]. Increasing the porosity can help to reduce the elastic modulus of the porous material which lowers the stored elastic energy for thicker layers but eventually contributes to decrease lifetime of the coatings [35]. The majority of pores in APS have a diameter smaller that 1 μm and up to 20% of the pores are in the 1 - 20 μm diameter range which increases with aging of the coating due to pore coarsening [36], which leads to a progressive increase of thermal conductivity and reduced toughness [37]. The as-deposited microstructure has a random distribution of porosity throughout the thickness, including voids, unmelted particles, oxide inclusions, intrasplat and interlamellar pores, resulting in

very low thermal conductivity [10, 38, 39, 40] and reduced stiffness [29]. APS coatings have a good strain tolerance which is essential for extended coating lifetime capabilities.

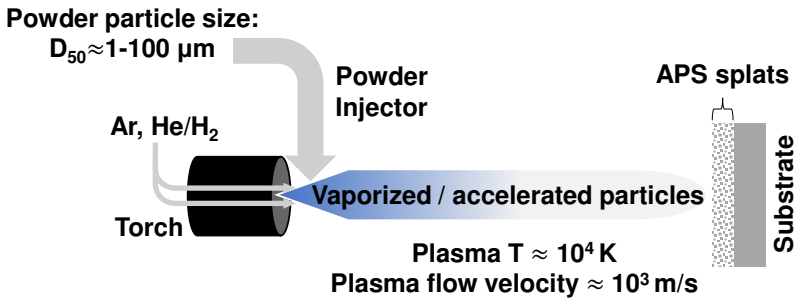

Figure 1.3: Air Plasma Spray method.

In the power generation industry, Air Plasma Spray is the preferred deposition method as land-based power generation turbine systems work under extended cycles and controlled environments. As a consequence, the coatings are not exposed to intense thermal cycling, which is known to reduce the lifetimes of APS coatings prohibitively [41, 42]. Additionally, the extreme temperatures produced in the plasma plume makes APS a desirable method for spraying refractory materials.

1.2.3 Electron Beam Physical Vapor Deposition (EB-PVD)

The standard process in the aerospace industry is Electron Beam Physical Vapor Deposition (EB-PVD). In practice, an electron beam is produced by a generator in a vacuum

chamber and is bent towards a positively charged ingot. The impacted atoms at the surface of the ingot are ejected, producing the successive melting and evaporation of the material. The control of the evaporation plume results in slow coating deposition onto the substrate [43]. The epitaxial growth of the adsorbed atoms on the surface of the substrate will form distinct structural morphologies which is determined by the working gas pressure in the chamber and the temperature of the substrate [44, 45]. These two parameters modify the mean free path of the particles as well as the kinetic energy of the ions reaching the substrate. To obtain the typical columnar grain structure for TBCs, a working gas pressure of about 10^{-6} atm and a substrate temperature of 1000°C can be used [46]. Figure 1.4 outlines the deposition method and its main characteristics. Batch deposition is generally done to compensate the low deposition rate of about 10 μm/min.

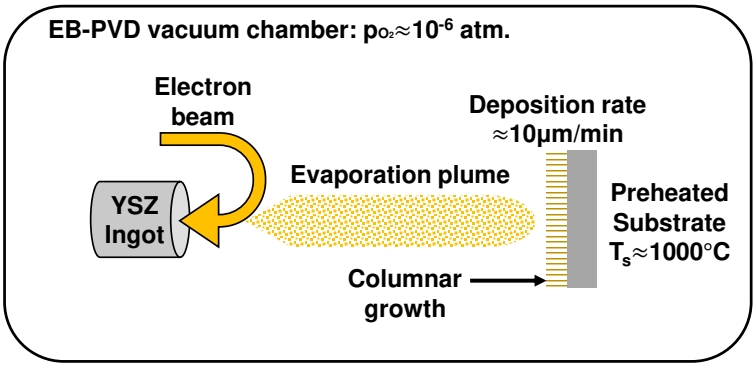

Figure 1.4: Electron Beam Physical Vapor Deposition method.

EB-PVD TBC coatings have a microstructure that is well-suited for thermal cycling, interdiffusion, hot corrosion and oxidation conditions [47], typically present in aero-engines. The coatings exhibit a characteristic microstructure that include columns that have a width of 2-10 μm. The intercolumnar spacing decreases drastically the in-plane elastic modulus [48], allowing for high thermal fatigue and strain resilience. Additionally, smooth interface between the top coat and the bond coat, as well as a smooth top surface, are advantageous for adherence and against particle erosion, respectively [49]. The intra-columnar feathery striations and fine pores contribute to a significant decrease of thermal conductivity with respect to bulk YSZ but direct thin air conduction paths contribute to the opposite effect. Typical thicknesses for EB-PVD coatings vary between 150 and 250 μm with a porosity from 5 to 25 %, which generally is a function of depth into the coating, going from a more compact microstructure closer to the bond coat and wider intercolumnar spaces closer to the top surface. EB-PVD has been shown to be superior to APS for aeroengine applications, due to the high strain tolerance of the typical columnar structure [50]. However, low rates of deposition and high investment costs compared to APS are generally listed as the main weaknesses of the technique for coating deposition. It can be added that components with complex geometries are also relatively challenging to coat with this method [51].

1.2.4 Thermomechanical properties

The typical material properties of industrial TBCs are as presented in Table 1.2. The deposition method used for the top layer affects the resulting properties and therefore the performance of the coatings.

Table 1.2: Thermomechanical properties of standard materials composing TBCs.

	Top coat		**TGO**	**Bond coat**
Typical composition	*7-8wt.% YSZ (APS)*	*7-8wt.% YSZ (EB-PVD)*	Al_2O_3	*NiCrAlY*
Thermal conductivity λ at 1100°C (W/(m·K))	1-2 [38, 52, 53]	2-3 [54]	5-6 [52, 55]	34 [53]
Coefficient of thermal expansion α ($\times 10^{-6}$ K^{-1})	11-13 [52, 56, 57]	11-13 [48]	7-10 [48, 56]	13-16 [48, 56]
Elastic modulus E (GPa)	10-50 [58]	0-100	320-434 [25, 48, 56]	110-240 [25, 48, 56]
Toughness K (MPa·$\sqrt{m}$)	0.7-2.2 [56, 37]		2.8-3.2 [56, 59]	>20 [56]
Poisson's ratio ν	0.2 [57]		0.2-0.25 [25, 57]	0.3-0.33 [25, 57]
Oxygen diffusivity at 1000°C (m^2/s)	10^{-11} [52]		10^{-20} [52, 55]	-
Crystal microstructure Phase stable up to (°C)	t' 1200-1250 [54]		α 1750	β, γ 1050

It can be highlighted in Table 1.2 that the rapid formation of the TGO creates an additional protection against oxidation of the bond coat. However, further oxide growth eventually leads to the progressive degradation of TBCs as a result of the accumulation of strains due to expansion mismatch with the surrounding materials, particularly during

thermal cycling. On the other hand, constant interactions between the layers control the durability of TBCs.

1.3 Thermally activated degradation mechanisms

1.3.1 Temperature effects on TGO growth

Extreme thermal loads induced during engine operation generate stresses that dissipate through crack propagation, delamination, spallation, and consequently determine coating lifetime [60, 61, 62]. A significant part of the accumulated stresses come from the formation of the TGO layer that produces lateral compressive stress and is responsible for the aluminum-depletion-induced volumetric changes [63]. The evolution of the TGO with thermal aging is associated with most of the major failure modes in TBCs [64, 65, 66]. Therefore, monitoring temperature at the TGO is crucial to better evaluate the oxide growth rate, estimate remaining coating lifetime and can be used as a key indicator of TBC degradation. The TGO growth process is highly sensitive to temperature: in a running turbine engine, a variation of 50°C usually results in the multiplication of the growth rate by a factor 2 or 3 [27, 67].

1.3.2 Phase stability of YSZ

The metastable tetragonal t' phase is desired in YSZ as it allows for cyclic operation up to 1200 - 1250°C with very high phase stability [68]. The optimal concentration of yttria to stabilize zirconia, by introducing oxygen vacancies into the crystal lattice, was found to be 7 - 8 wt.% (4 - 4.5 mol.%) [69, 35]. This percentage of stabilizer provides excellent thermal and mechanical properties. In practice, the preprocessing materials are sintered to temperatures around 2200°C which result in the crystallization of t' [70]. During operation, coating temperature can be directly correlated to the speed at which the materials degrade and the diffusion rate of species [71]. Rapid domain boundary segregation of Yttrium, facilitated at higher temperatures (typically exceeding 1250°C), results in the decomposition of the metastable tetragonal phase into a depleted-Yttrium tetragonal phase and a cubic phase with high Yttrium content [72, 73, 74, 75]. The cubic phase exhibits a lower fracture toughness which can be related to a facilitated crack propagation [34] and accelerated degradation of the coating. On the other hand, the tetragonal phase transforms to the monoclinic phase when temperature is reduced below 600°C in a thermal cycle, which leads to a 4% volume expansion of the crystal lattice [76, 34].

1.4 Motivations for accurate temperature measurements on TBCs

1.4.1 Possible efficiency improvements

Temperature measurement accuracy is a main concern for the optimization of engine efficiency in turbomachinary. In particular, the precise determination of the temperature in the high pressure turbine is crucial to adjust the equivalence fuel/oxidizer ratio to reach maximum efficiency. Currently, state-of-the-art TBCs are not being used to their highest potential because of uncertainties in temperature measurements at high-temperature [13, 77]. Safety margins as high as 200°C are used to accommodate the significant temperature error values [78], highlighting that a better monitoring of temperature would lead to greater efficiency, a more accurate lifetime prediction, as well as a mitigated degradation enabled by reliable and controlled temperature measurements [79, 80]. To give a perspective, a 1% efficiency increase can save $20m over the full lifespan of operation of a 400 - 500 MW combined cycle plant [81].

1.4.2 Enhanced lifetime monitoring of coatings

Turbine components are designed to operate for extended periods, for example, Siemens land-based gas turbine systems have generally a 30 - 40 years lifetime and hot

path components are expected to survive up to 100,000 hours or 3,000 starts [82]. Safe and reliable operation of engines, with reduced downtime, is facilitated by a more accurate control of temperature in extreme environments as it prevents from operating turbine blades in fast damaging conditions [83]. The determination of temperature, in particular at the top coat / bond coat interface is critical to better monitor the lifetime of the coatings.

1.4.3 Temperature measurement techniques for TBCs

Implementing an *in-situ* temperature measurement method in a high pressure turbine is often impractical due to high pressure and temperature conditions. Table 1.3 presents the existing techniques that are currently used to measure temperature on TBCs. Rotating blades running at high velocity, defined gas flow patterns and high operating temperatures limit the applicability of thermocouples, that uses the thermoelectric effect to generate a temperature-dependent voltage. Indeed, thermocouples can experience chemical diffusion that leads to significant measurement errors. This is without considering the meticulous labor required for the installation of thermocouple probes, attaching them at the surface of the turbine blades, creating defect points, or affecting the manufacturing process to integrate thermocouples below the top coat [84, 85].

Table 1.3: Existing temperature measurement techniques and associated features for turbine blade coatings.

Method	**Measured location**	**Range of temperature (°C)**	**Limits of the method**
Thermocouples	Point measurement	-250 to 2300	Intrusiveness Disrupting the flow [86] Chemical instability [87] Labor intensive
Thermal paints	Surface	150 to 1350	Low resolution [88, 89] Low maximum temperatures [90]
Infrared imaging	Surface	-50 to 2000	Sensitivity to stray light [91, 92] Sensitivity to emissivity variations induced by temperature or surface contamination [93, 94, 95]
Phosphor Thermometry	Surface or sub-surface	-250 to 1700	Weak signal at high temperatures [96, 97, 98, 99]

Among other options for TBC temperature measurements: thermal paints and thermal history sensors. These techniques have been applied in turbine environments, but are limited to off-line measurements. To reveal experienced temperature conditions, thermal paints use the thermochromism of pigments and thermal history sensors use the luminescence of sol-gel phosphor materials that evolves rapidly, after initial exposition of the as-fabricated material to high temperature, through recrystallization, phase transition, oxidation or diffusion processes [100, 101, 102]. These two techniques can record the peak temperatures of the TBC surface and potentially determine defect zones through hot spots.

Advanced monitoring techniques that ensure the integrity and durability of the TBC

are paramount to the structural integrity of the turbine blades. Optical methods are non-invasive and can potentially capture data under limited access to the hot-section of turbines. Infrared imaging stands out as one of the most prevalent technique for temperature measurements on TBCs. It is based on the collection of the thermal radiation, emitted by the materials in the infrared range. The ideal blackbody radiation can be predicted using Planck's law, which formula for spectral irradiance is given by Equation 1.1.

$$E_\lambda = \frac{8\pi hc^2}{\lambda^5} \frac{1}{e^{hc/\lambda kT} - 1} \tag{1.1}$$

where h is Planck's constant, c is the speed of light, λ is the wavelength, k is Boltzmann's constant, and T is the temperature.

In practice, materials have wavelength and temperature dependent emissivities that need to be considered when using thermal radiation based methods. The biggest advantage of this technique is its capability to perform non-contact real-time area temperature measurements with easy integration, but which precision is limited by the presence of emissions from the operation of the turbine engines and which accuracy is heavily susceptible to emissivity variation [94, 103, 104].

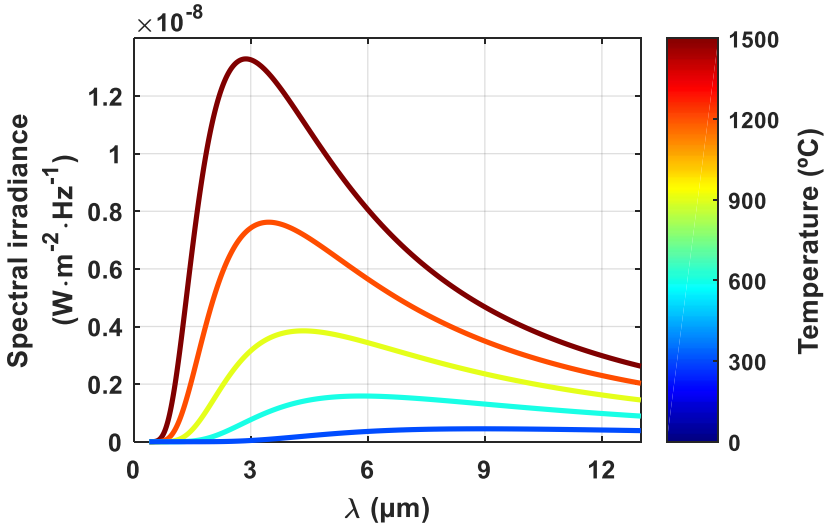

Figure 1.5: Blackbody radiation from 300°C to 1500°C.

Significant effort has been invested recently in developing TBCs that contain temperature sensors to use Phosphor Thermometry, a well-known technique that enables non-contact real-time measurements on TBCs, using temperature-dependent luminescence emitted from phosphors that produce robust and reproducible signal, with measurement capabilities that can overcome infrared measurements methods [105]. This technique has shown great potential for enhanced TBC temperature monitoring on operating engines [106, 107, 108, 109, 110]. It has the advantage of being versatile and its capabilities are still being extended for TBC characterization, in particular with the development of new material configurations with improved luminescence properties [111, 112]. Phosphor Thermometry allows for high accuracy of the temperature measurements with highly

sensitive phosphors. One of the biggest advantages of Phosphor Thermometry over the other techniques is its capability to measure temperatures under the surface of the coatings [113, 114], and closer to the interface between the top coat and the bond coat, which is the key location for the determination of TBC lifetime [115].

In this work, research has been focused on the development of novel temperature measurement material sensor configurations, instrumentation and methods, applied to TBCs, using Phosphor Thermometry. This technique is believed to be extremely promising for improved temperature measurement effectiveness in real operating conditions of turbine engines, and for further extension of temperature monitoring capabilities.

CHAPTER 2
PHOSPHOR THERMOMETRY FOR TEMPERATURE MONITORING OF THERMAL BARRIER COATINGS

Luminescence is a spontaneous process in which electrons returning to lower energy levels produce the emission of photons. Figure 2.1 describes the phenomenon. Electrons originally located at the ground state are pumped to an unstable energy level through the absorption of an external radiation source of specific wavelength that enables such transition. In the case of the existence of a slightly lower energy level, electrons rapidly transition to this level non-radiatively (phonon deexcitation). Subsequently, if the electrons remain in a metastable energy level that is separated with a large energy gap from lower energy levels, the return to the ground state will occur progressively following an exponential decrease trend which corresponds to the radiative relaxation of the electron population (photon emission).

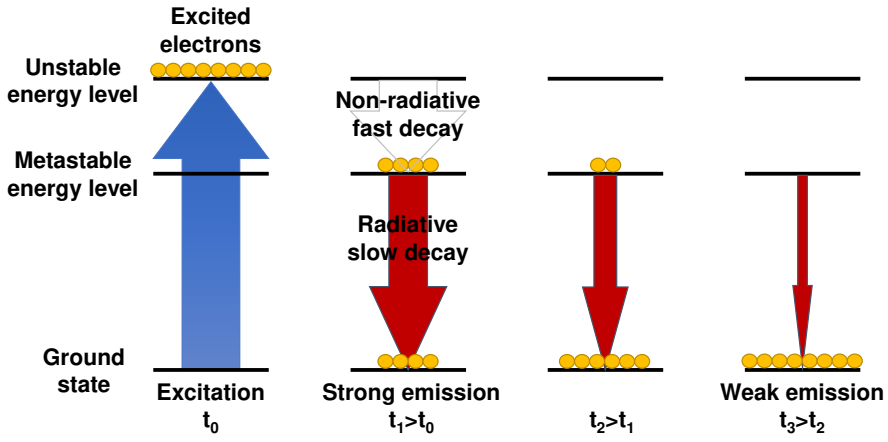

Figure 2.1: Deexcitation process leading to luminescence

Phosphor Thermometry is a non-invasive temperature measurement technique that utilizes the temperature-dependency of luminescence produced by embedded doping transition metals or rare-earth elements inserted into ceramic hosts. For rare-earth elements, it is well-known that the less energetic $5s$ and $5p$ orbitals shield the $4f$ valence electrons efficiently. As a consequence, the surrounding crystalline field does not destabilize the energy transitions of the rare-earth ions. The emission peaks produced in distinct hosts by a rare-earth ion, therefore possess very similar luminescence properties. This results also in elevated quenching temperatures that make rare-earth doped phosphors suitable for high temperature applications. Consequently, rare-earth based sensors are generally preferred over transition metals for TBC applications. Observable transitions occur for trivalent rare-earth ions between the $5d$ and $4f$ energy levels, or, in between the $4f$ orbital itself

[116]. The mismatch between the host and dopant lattice sizes determines the extent of temperature range at which the doped ceramic will be able to be sensitive to temperature. Large differences between their lattice dimensions result in larger spaces for phonon vibration, which is responsible for thermal quenching [117]. An enormous amount of phosphor elements have been utilized with the objective of developing temperature sensing capabilities [111, 118, 119]. The Phosphor Thermometry technique requires the excitation of phosphors by a laser source of a particular wavelength that is selected based on the absorption spectrum of the sensing dopant. Two main methods are well-known to obtain temperature from this technique: The intensity ratio method, and the lifetime decay method [120, 121, 122]. In the intensity ratio method, the ratio between the luminescence intensities of two emission peaks is used to determine the temperature of the material, whereas, in the lifetime decay method, the decay of luminescence intensity of one single emission peak is used to retrace temperature [110]. The temperature-dependent decay constant of the luminescence is indeed used to infer the temperature after a required calibration step. The lifetime decay method offers the advantage of higher sensitivity and precision in high temperature measurements [123].

2.1 Phosphor configurations

A large number of rare-earth doped material configurations have been considered as potential sensors for Phosphor Thermometry applied to TBCs. Europium and Dysprosium stand out for their intense luminescence that is conserved at high temperatures. The concentration of dopant is generally lower than 3 wt.% to enable high luminescence and avoid any phase change and conserve the thermomechanical or optical properties of the undoped material. The main material configurations (rare-earth dopant (RE) + host is noted Host:RE) that were tested in literature for TBC applications are presented below.

2.1.1 Rare-earth doped Yttrium Aluminum garnet ($Y_3Al_5O_{12}$:RE)

Yttrium Aluminum garnet, also referred as YAG: This matrix has the advantage of possessing a very low oxygen diffusivity (10^{-25} m^2/s for bulk YAG), a low thermal conductivity at high temperature (3.2 W/m·K at 1000°C) [124] and a good phase stability up to its melting point (1970°C) [125]. However, the limited thermodynamic compatibility with the other phases present in standard TBCs [126] and its low coefficient of thermal expansion (6 - 8·10^{-6} /°C) [59, 127], combined with a low fracture toughness ($\approx$ 1.8 MPa·$\sqrt{m}$) [125] reduces its application scope in TBCs. In terms of luminescence properties, when

used in combination with rare-earth dopants, it exhibits excellent high temperature measurement capabilities, up to at least 1400°C [128, 129]. YAG:Dy has been extensively used, including in turbine environments [80, 86, 130, 131, 132, 133, 134], YAG:Eu has similarly shown high temperature capabilities [135, 136, 137]. YAG:Tm has been studied as it provides ultraviolet luminescence that is advantageous in presence of thermal radiation [134] and its quenching temperature is as high as 1100°C which makes it suitable for TBC surface applications [130, 138].

2.1.2 Rare-earth doped Yttrium oxide (Y_2O_3:RE)

Yttrium oxide has been mainly combined with Europium (Y_2O_3:Eu). Although it is known to display intense luminescence that is appropriate for Phosphor Thermometry on sensing TBCs [86, 106, 108, 130, 131, 135, 139], in particular for buried layers, this configuration is not ideal for real engine conditions as its luminescence signal is too low at temperatures exceeding 900°C, due to oxygen quenching [90]. Additionally, high pressure environments annihilates luminescence of Y_2O_3:Eu [140].

2.1.3 Rare-earth doped Yttria stabilized zirconia (YSZ:RE)

The utilization of YSZ as the host material for rare-earth luminescence dopants is an attractive option for embedded sensing layers because of the layer compatibility with the rest of the TBC system which allows for reduced intrusiveness of the sensor. Rare-earth doped YSZ configurations for sensing TBCs have been thoroughly investigated [2, 141] due to its easy integration and suitability to high temperature luminescence applications. YSZ:Eu has been largely studied because of its intense luminescence that can be used for integration of a sensing layer in the depth of the TBC, and because it exhibits high sensitivity to temperature from 500 to 850°C [1, 80, 86, 137, 142, 143, 144]. YSZ:Dy has been also considered as it displays the highest temperature capability among rare-earth doped YSZ (about 1000°C), using the lifetime decay method [1, 80, 93, 128, 137, 145, 146]. Other rare-earth dopants have been tested in a YSZ host for TBC applications using Phosphor Thermometry, namely, YSZ:Sm [147, 148], YSZ:Gd [80] and YSZ:Er [2, 148]. It can be noted that YSZ:Tb was found to be unusable due to the rapid oxidation of Tb [149]. Another attractive feature concerning YSZ:Eu and YSZ:Dy is that both phosphors possess a sensitivity that remains unchanged after thermal aging or at different dopant concentrations [150].

2.2 Effects of dopant concentration

The luminescence intensity that can be produced by a luminescent material is largely dependent on the concentration of luminescent ions, called activator ions. As the concentration increases, if the activator ions are well dispersed into the ceramic host, for a determined area, a higher number of photons can be emitted. However, at higher concentrations or if the doping ions agglomerate, their interaction will cause vibrational deexcitation resulting in the lower probability of photons emission. This phenomenon is called concentration quenching. Some of the synthesis methods used for the production of luminescent materials for Phosphor Thermometry such as Solid State Reaction are likely to form dopant clusters. Agglomeration can result in both a reduced maximum concentration level to achieve optimal luminescence intensity as well as a fast decay component when measuring the time response of the luminescent material under a pulsed excitation. It is important to note that impurities (hydroxy group, organic compounds) that can be present in the luminescent coatings contribute highly to luminescence quenching. To overcome this issue, luminescent samples can be annealed at temperatures exceeding 800°C for at least 2 h to enhance luminescence [77, 90, 151].

The Johnson-Williams equation, presented in Equation 2.1, gives a good approximation of the effect of dopant concentration on the intensity of luminescence, assuming ho-

mogeneous distribution of activator ions in the host matrix [152, 153]. The maximum concentration of doping ions, for a particular combination of dopant and ceramic host, depends on the actual energy levels of the activator ion in the specific host [126]. The Johnson-Williams equation is defined as following:

$$I_c = \frac{c(1-c)^z}{c + \frac{\sigma}{\sigma'}(1-c)} \tag{2.1}$$

where c is the dopant concentration, z is the number of nearest dopant cation neighbors and $\frac{\sigma}{\sigma'}$ is the capture cross section of non-activators, accounting for the actual absorption cross-section of luminescent receptors in the material.

Figure 2.2 shows the results obtained by digitizing experimental results that demonstrate the effects of concentration on luminescence intensity, found in literature, to obtain the fitting parameters for the Johnson-Williams equation [126, 150, 154, 155]. It can be noted that the optimal concentration for maximum luminescence intensity is strongly dependent on the dopant used into a YSZ matrix.

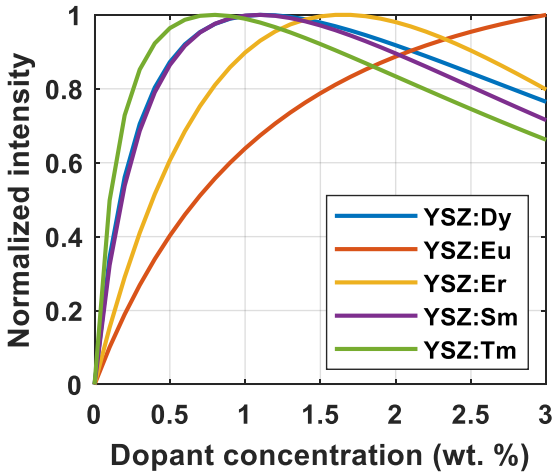

Figure 2.2: Predicted dependency of luminescence intensity in function of dopant concentration, and limited due to concentration quenching.

2.3 Rare-earth doped layer stability in ceramic coatings

The adaptation of Phosphor Thermometry to TBCs requires the manufacturing of embedded sensing layer configurations. One difficulty to consider in real conditions is the existing thermal gradient which can lead to significant measurement errors. A proposed solution is the application of a thin sensing layer, which minimizes the thermal gradient through the doped layer. However, the signal intensity is reduced proportionately. As a consequence, the thickness of the sensing layer needs to be adjusted to get a trade-off between temperature gradient and signal intensity. In this work, an intent to overcome

this particular issue is discussed, later in the following chapters, where the exact location at which temperature measurement is performed could be estimated, through simulations, for any doped layer thickness, and in presence of a thermal gradient. Such claim promotes thick doped layer configurations as they obviously provide higher luminescence intensities.

Designing multilayer TBC configurations for precision temperature measurements using Phosphor Thermometry is only possible if the location of the sensing layer is known. Therefore, it is essential to determine up front if discrete rare-earth doped layers remain in place when embedded into a TBC configuration, to enable luminescence sensing. The possible diffusion of luminescent ions has been modeled in YSZ to evaluate the stability of the position of dopants when embedded in a TBC as a thin layer in a multilayered configuration. The simulation uses the 2^{nd} Fick's law for diffusion, presented in Equation 2.2.

$$\frac{\partial c_{RE}}{\partial t} = D_{RE}\frac{\partial^2 c_{RE}}{\partial x^2} \tag{2.2}$$

where c_{RE} is the normalized dopant concentration, $D_{RE} = 5.2 \cdot 10^{-8} \mu m^2/s$ is the grain boundary diffusivity of rare-earth ions in YSZ, x is the position into the coating, originating

at the top surface and t is the time of operation of the TBC at 1200°C. The initial condition is defined in Equation 2.3 and the boundary condition assuming no external dopant source is defined in Equation 2.4.

$$c_{RE}(50 \leq x \leq 100) = 1 \tag{2.3}$$

$$\frac{\partial c_{RE}}{\partial t}(0,t) = 0 \tag{2.4}$$

The grain boundary diffusion was calculated using the diffusivity of Gadolinium (Gd) in cubic 8 mol.% YSZ at 1200°C in a Physical Vapor Deposition coating [156]. The grain boundary diffusion corresponds to a faster diffusion mode than bulk diffusivity and has been considered solely for this study to determine if the rare-earth diffusion in YSZ is negligible, and thus if multilayer configurations including discrete luminescent layers are viable. It is assumed that the diffusivity of other rare-earth elements remains identical to that of Gd and that the higher concentration of stabilizer, existing in the reference that was chosen in literature (Yttrium or rare-earth ions in zirconia), and leading to the prominence of the cubic phase, does not affect diffusion in YSZ. The bulk diffusivity of YSZ can be compared and supported by the value of cation diffusivity in standard 7-8 wt.% tetragonal YSZ found in literature [157].

The model configuration used for this simulation includes a 50 μm-thick layer of rare-earth doped YSZ, buried at 50 μm from the top surface into an undoped YSZ top coat. Figure 2.3 shows the results for the diffusion over the standard lifetime of a turbine blade TBC, indicating that the grain boundary diffusion penetration of dopant rare-earth ions throughout the surrounding ceramic top coat is negligible. As a consequence, it is possible to fabricate multilayer configurations including thin luminescent layers that remain in place over time.

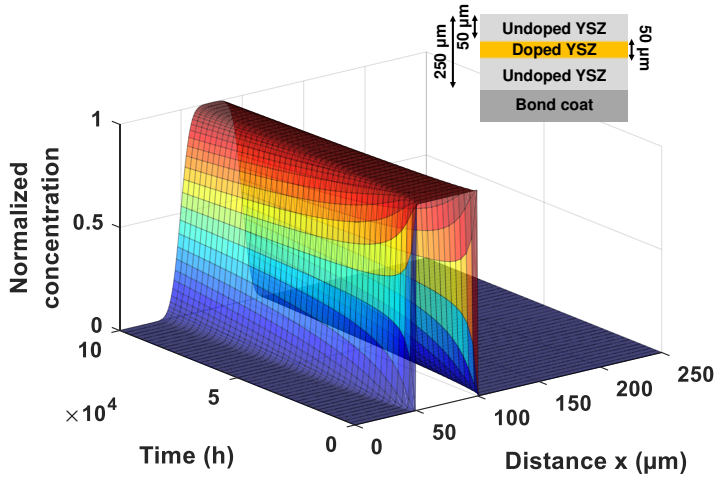

Figure 2.3: Predicted diffusion of rare-earth dopant through YSZ at 1200°C.

2.4 Data acquisition methods

2.4.1 Lifetime decay method

The acquisition of the radiative lifetime decay using a fast response detector (photomultiplier tubes or high-speed cameras are standard methods), allows for indirect temperature measurement from the data, after fitting the decay with single or multiple exponential models. The decay is related to the rate of energy transitions coming from the excited electron population that decreases its energy from a metastable energy level pumped by a laser source and that returns to ground level, as presented in Figure 2.1. In most cases, the simplified single-exponential decay model is preferred for robust temperature measurements, as given in Equation 2.5.

$$I(t) = I_0 \cdot e^{(-t/\tau(x))} \tag{2.5}$$

where I is the measured intensity, I_0 is the initial intensity at time $t = 0$, and τ is the decay constant, that is later correlated with the temperature measurement.

In practice, at $t = 0$, the excitation source turns off and the electrons return to the ground state after a delayed process of deexcitation. The time at which the remaining intensity of luminescence reaches $1/e$ of its initial value is τ, which is temperature de-

pendent. At higher temperatures, the higher thermal energy that is available facilitates vibrational deexcitation, and consequently, τ decreases. This phenomenon is represented in Figure 5.9, where the acquisition window shows the luminescence decay at two distinct temperatures (with $T_1 > T_2$). A calibration step is usually achieved to determine the lifetime decay response of a sensing coating. This step allows to highlight the sensitive temperature range used to retrace temperature. Thermal quenching generally enhances the sensitivity of the lifetime decay to temperature. For this reason, the lifetime decay method usually has a higher sensitivity to temperature than intensity-based methods [123].

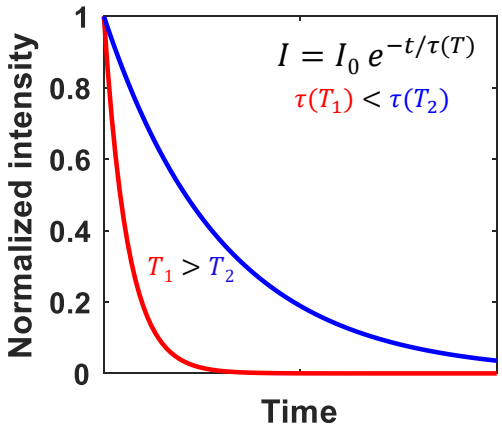

Figure 2.4: Typical luminescence intensity with respect to time

In a real engine environment, in which a luminescent coating is applied to a turbine blade, it is important to compare the rotation speed of the blade and the decay constant to determine if the lifetime decay method is applicable. In the high pressure turbine stage of a typical turbine system, blades can reach a linear velocity of 0.7 mm/μs, when operating

at 20,000 rotations per minute [130]. This value can be used for arbitrary down-selection of material configurations by eliminating the configuration for which the decay constant too long to be properly detected in presence of a linearly moving emission source initially excited by the laser pulse. In the case of rare-earth doped YSZ configurations, the decay constant is approximately 1 μs for all sensors, when exposed at about 900°C [2], which allows for collection of the decay by a fixed detector, neglecting the acquisition angle created by the movement of the probed blade.

2.4.2 Intensity ratio method

Luminescence intensity ratio between temperature sensitive emission peaks can be used for temperature determination, using a spectrometer. Dysprosium-based luminescence is well-known for Phosphor Thermometry using this method due to the thermal filling of the $^4I_{15/2}$ energy level, strengthening the emission peak at 458 nm in a process called thermalization [132]. In this case, the intensity ratio between the emission peaks at 458 and 485 nm allows to retrace temperature [128]. This technique allows for high temperature measurements, that are eventually limited by the growing thermal radiation combined with thermal quenching.

2.5 Motivations for preliminary predictive models

There are numerous combinations of dopant and host materials that can achieve TBC sensing through Phosphor Thermometry. To aid the selection of materials, it is crucial to understand the physical phenomena that drive the luminescence properties while ensuring that TBC performance is maintained. The prediction of luminescence properties through modeling can greatly simplify material selection, thus focusing the experimental effort on most relevant designs. The theoretical approach facilitates the development of new data acquisition methodologies, extending the capabilities of the technique. It additionally helps for the better understanding of the luminescence behavior in scattering media, which can later be used to evaluate and predict coating damage and temperature measurement locations, helping for better TBC lifetime predictions.

CHAPTER 3
LUMINESCENCE MODELING AND RESULTS

3.1 Luminescence intensity in doped coatings

The challenge with modeling light propagation in TBCs, in order to understand its implications in Phosphor Thermometry, is to account for the significant amount of scattering that occurs in porous ceramic coatings. In addition, it is necessary to consider light absorption, as it travels through the coating. A model to account for this type of attenuation is the Kubelka-Munk model [158, 159]. This model is a 1D model that assumes isotropic scattering of light and can model the distribution of light intensity in complex media. This model has been further extended for specific applications [160, 161, 162], and it has been applied in various fields including paint and papers [163], colorants and interference pigment mixtures [164], light trapping in plants and biological tissues [165, 166], and blood stain detection [167]. The model has been later implemented to describe excitation and emission intensity distributions within TBCs [114, 168].

In this work, the behavior of the phosphor luminescence in TBC configurations has been studied. To that goal, the four-flux Kubelka-Munk model has been used to predict the intensity of the luminescence. The two TBC configurations considered in this study are the configuration **(C1)**, that contains a fully doped top coating, and the configuration **(C2)**, that contains an embedded doped layer in the top coat, as shown in Figure 3.1. The TBC configuration with an embedded doped layer has two geometrical parameters to uniquely describe the configuration for the purpose of interest, namely, the position of the doped layer and the thickness of the doped layer. In the modeling work achieved here, the total thickness of the top coat is maintained constant at 250 μm and the position is defined as the distance from the top surface of the TBC to the top surface of the doped layer. Three rare-earth doped materials, YSZ:Dy, YSZ:Er and YSZ:Sm have been considered for this study. A detailed parametric study is performed by systematically varying the position and thickness of the doped layer.

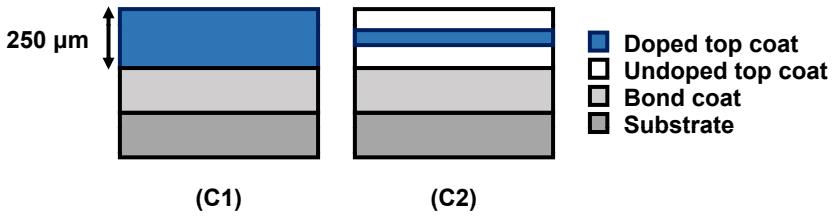

Figure 3.1: Configurations of TBC including a doped layer for Phosphor Thermometry, (left) fully doped configuration **(C1)** and (right) embedded doped layer in the top coat **(C2)**.

For a given excitation intensity input to the top surface of the TBC, the intensity of the emerging luminescence arising from the phosphorescent TBC depends on the absorption and scattering of the light into the coating. Therefore, the design of the TBC configuration strongly affects the intensity of the collectable signal. Figure 3.2 shows a schematic of the traveling incident laser light, and emitted luminescence in an example configuration that contains a doped layer inside the YSZ top coat. The position (x_1) of the top surface of the embedded doped layer of thickness $t = x_2 - x_1$ is measured from the TBC surface.

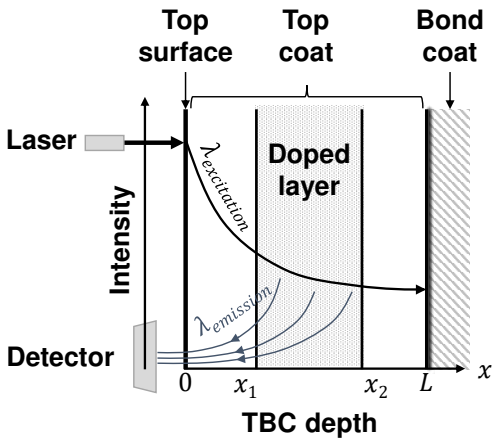

Figure 3.2: Mechanism of absorption of excitation (incident laser) and emission (luminescence) lights through the TBC.

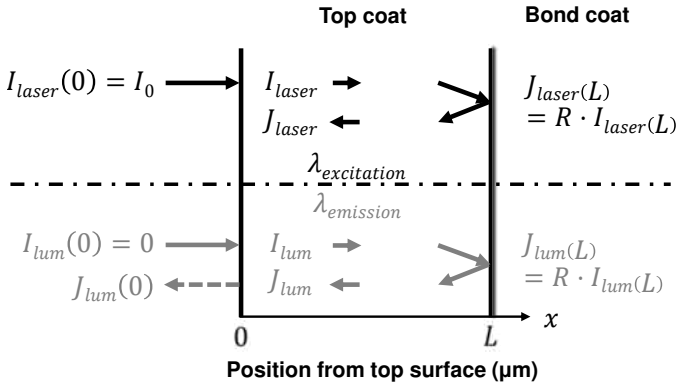

Figure 3.3: 1D Four-flux Kubelka-Munk boundary conditions to model phosphor luminescence in TBCs.

The classical four-flux Kubelka-Munk model accounts for the simultaneous absorption and scattering of laser and luminescence lights traveling in the depth of the material, along the x-axis, in two opposite directions. The notations are illustrated in Figure 3.3. At any point x, the incident laser light intensity traveling toward the bond coat is denoted by I_{laser} and that traveling back toward the TBC top surface is denoted by J_{laser}. Similarly, the intensities of the luminescence light traveling toward the bond coat and back to the top surface of the TBC are denoted by I_{lum} and J_{lum}, respectively.

The governing differential equation describing the intensities of the incident light traveling in and out (refer to Figure 3.3) can be formulated in a matrix form, as given by Equation 3.1.

$$\begin{Bmatrix} I'_{laser} \\ J'_{laser} \end{Bmatrix} = \begin{bmatrix} -(K_{laser}+S_{laser}) & S_{laser} \\ -S_{laser} & K_{laser}+S_{laser} \end{bmatrix} \begin{Bmatrix} I_{laser} \\ J_{laser} \end{Bmatrix} \tag{3.1}$$

where I'_{laser} and J'_{laser} denote differentiation of I_{laser} and J_{laser} with respect to x, respectively.

The luminescence is assumed to occur due to the incident lights I_{laser} and J_{laser} for a certain quantum efficiency (q) of the material. Therefore, the governing equation for the luminescence light can be defined as given in Equation 3.2.

$$\begin{Bmatrix} I'_{lum} \\ J'_{lum} \end{Bmatrix} = \begin{bmatrix} -(K_{lum}+S_{lum}) & S_{lum} \\ -S_{lum} & K_{lum}+S_{lum} \end{bmatrix} \begin{Bmatrix} I_{lum} \\ J_{lum} \end{Bmatrix} + \begin{bmatrix} \frac{qK_{laser}}{2} & \frac{qK_{laser}}{2} \\ -\frac{qK_{laser}}{2} & -\frac{qK_{laser}}{2} \end{bmatrix} \begin{Bmatrix} I_{laser} \\ J_{laser} \end{Bmatrix} \tag{3.2}$$

In the above equations, $K_* = 2k_*$, and $S_* = 2s_*$, where k_* and s_* are the respective absorption and scattering coefficients of the media, and q is the quantum efficiency. Equations 3.1 and 3.2 present the Kubelka-Munk model to describe the excitation (laser) and emission (luminescence) intensities at any position x into the TBC with I_* and J_* representing light traveling in the positive and negative x, respectively. The second term in Equation 3.2 accounts for the luminescence arising from the phosphors by the incident intensity. The intensity of the luminescence is governed by the quantum efficiency (q) which

is taken as 0.5 in this study for all three materials [168]. To use the governing equation for discrete layers, the second term was modified in this work using the Heaviside step function such that the luminescence occurs only in the doped layer given by Equation 3.3.

$$\mathscr{H}(x-x_1)\mathscr{H}(x_2-x)\begin{bmatrix} \frac{qK_{laser}}{2} & \frac{qK_{laser}}{2} \\ -\frac{qK_{laser}}{2} & -\frac{qK_{laser}}{2} \end{bmatrix}\begin{Bmatrix} I_{laser} \\ J_{laser} \end{Bmatrix}, \tag{3.3}$$

where x_1 and x_2 are the positions of the doped layer (refer to Figure 3.2) and $\mathscr{H}(x)$ is the Heaviside step function.

The boundary conditions are implemented accounting for the intensity of the incident light ($I_{laser}(x=0)=100\,a.u.$ and $I_{lum}(x=0)=0$) and the reflection coefficient R at the bond coat (set at 0.15 as defined in [114]). The boundary conditions used to solve the governing differential equations are also depicted in Figure 3.3.

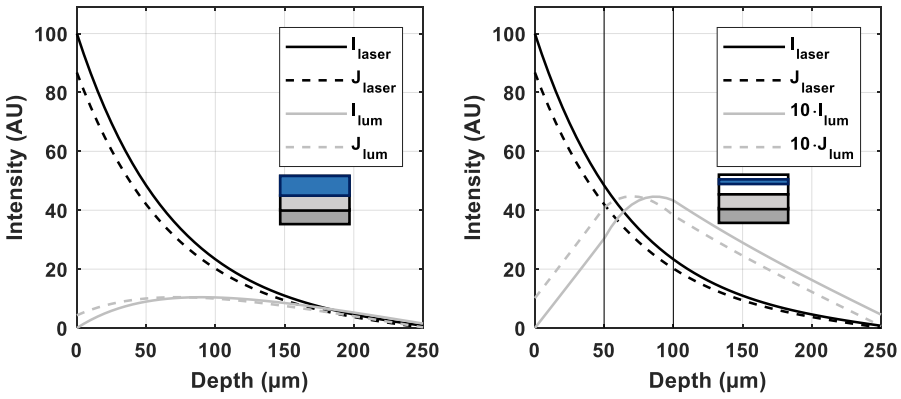

(a) (b)

Figure 3.4: Distribution of excitation laser and luminescence intensities through the coating based on Kubelka-Munk model for YSZ:Dy for (a) fully doped top coat **(C1)** and (b) configuration **(C2)** with 50 μm doped layer positioned at 50 μm from the surface.

The solutions of the Kubelka-Munk model described above to predict intensities at different positions of the top coat are shown in Figures 3.4(a) and 3.4(b), for the configurations **(C1)** and **(C2)**, respectively. These solutions correspond to the case where the TBC is doped with YSZ:Dy, wherein the configuration **(C1)**, the top coat is fully doped while in configuration **(C2)**, the doped layer of YSZ:Dy is embedded in an undoped YSZ top coat (refer to Figure 3.1). The wavelengths of the incident (excitation) and luminescence light depend on the dopant that is used. The excitation and luminescence wavelengths associated with the dopants are listed in Table 3.1. The optical properties of YSZ:Dy have been reported in experimental data [114], when the dopant is added in a small amount (typically $\approx$ 1 - 3 wt.%), can be approximated by that of undoped YSZ. In the different

literature references taken for experimental comparison, optical properties of YSZ given in literature [3] provide the best approximation. Therefore, the absorption and scattering coefficients for the specific wavelengths of interest in this study have been taken based on this reference and are listed in Table 3.1. Further, in the case of the configuration **(C2)**, all the results reported correspond to a TBC configuration where the doped layer has a thickness of 50 μm and is buried at 50 μm from the top surface. The collectable luminescence is the value of J_{lum} at $x = 0$. It can be observed that, for the selected quantum efficiency, the theoretical intensity of the collectable luminescence is 4.3 % of the incident intensity in the case of configuration **(C1)** and 1.0 % of the incident intensity in the case of configuration **(C2)**.

Table 3.1: Optical properties of YSZ from experimental data published in literature [3].

Material	λ **(nm)**	**scattering coefficient** s **(m^{-1})**	**absorption coefficient** k **(m^{-1})**
Excitation properties			
YSZ:Dy	355	50866	511
YSZ:Er / YSZ:Sm	532	33026	111
Emission properties			
YSZ:Dy	590	29585	95
YSZ:Er	545	32113	107
YSZ:Sm	619	28490	88

Table 3.2: Collectable intensity (% of incident light) for different TBC configurations with various doped layers.

Collectable intensity (% of incident light)	**YSZ:Dy**	**YSZ:Er**	**YSZ:Sm**
Fully doped TBC: $x_1 = 0$ μm, $x_2 = 250$ μm	4.3	1.4	1.5
Embedded doped layer: $x_1 = 50$ μm, $x_2 = 100$ μm	1.0	0.4	0.4

The effects of the position and the thickness of the doped layer in the configuration **(C2)** are shown in Figure 3.5(a). The figure shows the effect of varying the position of a YSZ:Dy doped layer that has a fixed thickness of 50 μm in the top coat of the TBC. The collectable intensity decreases from 2.9 % to 0.3 % when the 50 μm thick doped layer is moved from the top surface to a depth of 100 μm. The effect of varying the thickness of the doped layer when it is deposited at the top of the coating is depicted in Figure 3.5(b). For a doped layer that has no thickness, there will obviously be no luminescence intensity. It can be observed that the collectable intensity reaches a threshold (approximately 4.2 %) for thicknesses bigger than 150 μm. This implies that further increasing the thickness of the doped layer will not contribute to the collectable intensity as the luminescence does not reach the surface when emitted from further in-depth locations. The collectable intensities at the surface of the TBC configurations using different dopant layers are predicted by the model as listed in Table 3.2. Three materials, YSZ:Dy, YSZ:Er and YSZ:Sm have been chosen due to their promising properties for applications in phosphor thermometry [1, 2, 141]. The optical properties for the materials are listed in Table 3.1. The scattering and absorption coefficients of the incident light are found to strongly affect the collectable luminescence. It can be seen that YSZ:Dy exhibits higher luminescence intensity in both **(C1)** and **(C2)** configurations due to the significantly higher scattering and absorption coefficients at the incident wavelength of 355 nm (Table 3.2).

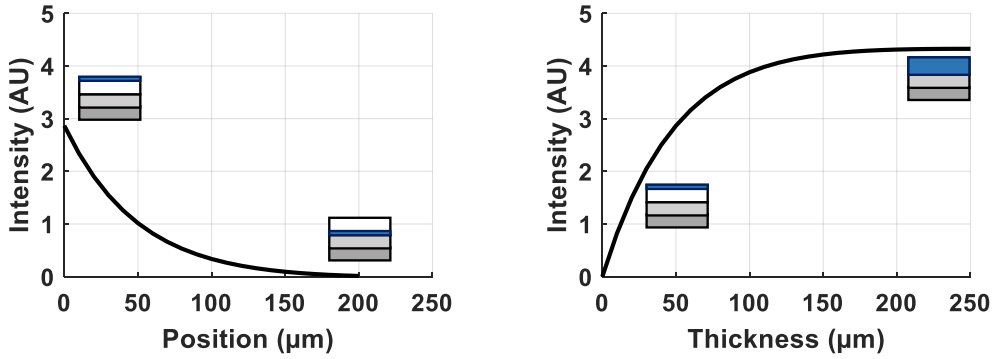

(a) (b)

Figure 3.5: Effects of (a) position of the doped layer of a constant thickness and (b) thickness of the doped layer when placed at the top on the collectable luminescence intensity predicted by the classical Kubelka-Munk model for YSZ:Dy.

Phosphor Thermometry often applies to complex sensing configurations that possess multiple layers that can exhibit distinct optical properties. The Kubelka-Munk model has been adapted in this work for double-layer configurations. In standard TBCs, this configuration exists after some thermal aging, considering that the well-known luminescence of the TGO can be used for luminescence sensing to evaluate temperature, up to 600°C [141], or to characterize stress in the TBC [169].

The modification applied to the Kubelka-Munk model for two distinct layers, labeled **1** (top coat) and **2** (TGO), of dissimilar absorption and scattering coefficients, as presented in Figure 3.6(a), is given in Equation 3.4. It can be noted that layer **3** (bond coat) is not considered for light travel but plays a role for interface reflectivity.

$$\begin{Bmatrix} I'_{1,lum} \\ J'_{1,lum} \\ I'_{2,lum} \\ J'_{2,lum} \end{Bmatrix} = \begin{bmatrix} -(K_1+S_1) & S_1 & 0 & 0 \\ -S_1 & K_1+S_1 & 0 & 0 \\ 0 & 0 & -(K_2+S_2) & S_2 \\ 0 & 0 & -S_2 & K_2+S_2 \end{bmatrix} \cdot \begin{Bmatrix} I_{1,lum} \\ J_{1,lum} \\ I_{2,lum} \\ J_{2,lum} \end{Bmatrix} + \begin{bmatrix} 0 & 0 & 0 & 0 \\ 0 & 0 & 0 & 0 \\ 0 & 0 & \frac{q \cdot K_2}{2} & \frac{q \cdot K_2}{2} \\ 0 & 0 & -\frac{q \cdot K_2}{2} & -\frac{q \cdot K_2}{2} \end{bmatrix} \cdot \begin{Bmatrix} I_{1,laser} \\ J_{1,laser} \\ I_{2,laser} \\ J_{2,laser} \end{Bmatrix} \tag{3.4}$$

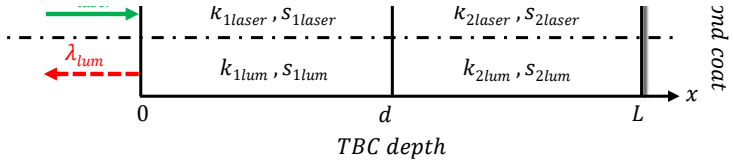

(a) Definition of the layer configuration and optical properties

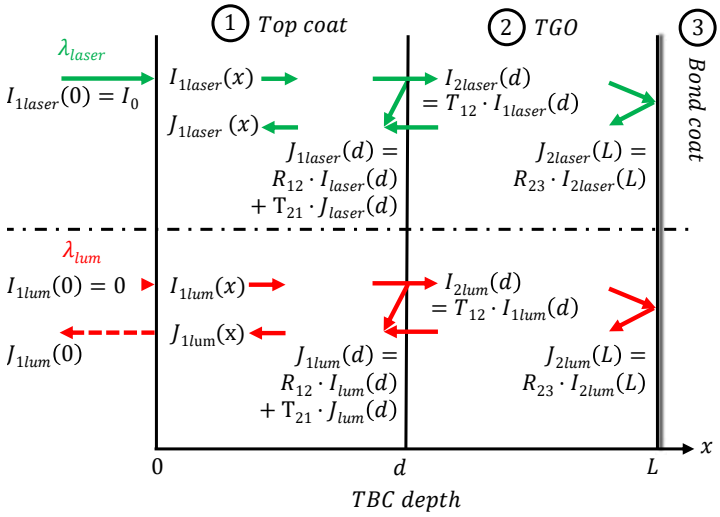

(b) Boundary conditions

Figure 3.6: Modification of the Kubelka-Munk model for double-layer configuration applications in TBC, in which the TGO is luminescent and the top coat is not.

Concerning the boundary conditions, the percent reflectivity and transmissivity are given by R_{ij} and T_{ij}, where $_{ij}$ represents the layer interaction $i \rightarrow j$. For the numerical study, the optical properties of alumina were taken from literature [170, 171]. The reflectivity at the bond coat was chosen arbitrarily to be 50 %. The quantum efficiency was assumed to be 0.5. The resulting distribution of luminescence intensity, traveling into the TBC, which is for this study comprised of a 200 μm top coat and a 10 μm oxide layer is presented in Figure 3.7. This model enables luminescence prediction for the determination of the feasibility of multilayer sensor coatings for Phosphor Thermometry.

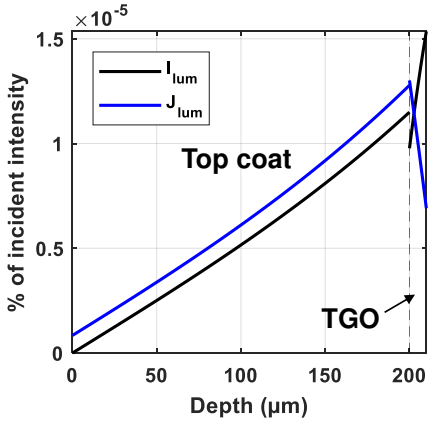

Figure 3.7: Luminescence intensity produced in TGO is attenuated as it travels back to the top surface. Laser intensity is not shown on this graph.

3.2 Location of temperature-dependent luminescence

The model has been extended to account for the time decay behavior of the emerging phosphor luminescence to understand the effectiveness of the TBC configurations applied to Phosphor Thermometry. The model developed has been applied to multilayered doped TBC configurations to understand the effects of the geometry of the embedded doped layer on the temperature measurement using the lifetime decay method. Three rare-earth doped materials, YSZ:Dy, YSZ:Er and YSZ:Sm have been considered for this study and the in-depth position and the thickness of the added doped layer have been incrementally varied to evaluate their influence in the resulting temperature measurement.

While the prediction of the value of luminescence intensity remains critical to ensure the feasibility of data collection at high-temperatures, as the lifetime decay method offers the advantage of higher sensitivity and precision in temperature measurement [123], modeling the decay behavior of the emerging luminescence is of key importance for Phosphor Thermometry by the decay method. Following an excitation pulse of laser, the decrease of luminescence intensity with time is typically described, for the dopants used in this study, using an exponential function: $I(t) = I_0 e^{-t/\tau(T)}$ in which $\tau(T)$ represents the decay constant that is temperature dependent. Starting from a temperature threshold called quenching temperature, the energy of the phonons is high enough to allow for deexcita-

tion through vibrations between energy levels. The rate of non-radiative emissions is then highly sensitive to temperature which is directly reflected on the rate of emitted photons. To predict the luminescence decay behavior along with the intensity in this work, the classical Kubelka-Munk model has been extended by considering the decay behavior of the luminescence from the dopants.

To model a realistic TBC environment, a linear temperature distribution with a gradient of 1 K/μm was assumed through the coating thickness. This was used to determine the spatial distribution of $\tau(x)$ [172]. The decay constant and temperature across the depth of the TBC are shown in Figure 3.8. It has been reported in literature that thermal conductivity of the doped layer is very close to that of the host material (within 5 %), therefore, the temperature distribution in both the configurations **(C1)** and **(C2)** was assumed to possess identical thermal properties as those of the undoped material. However, a model considering the temperature dependence and effects of addition of dopants on the thermal conductivity may be included to obtain more accurate temperature distribution across the TBC.

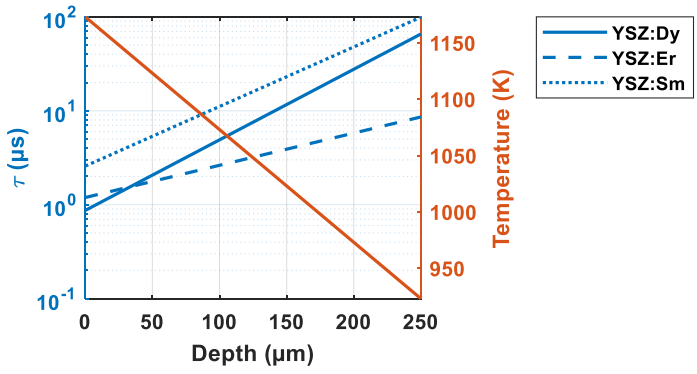

Figure 3.8: Variation of $\tau(x)$ with TBC in-depth location due to the temperature gradient. Data has been fitted from experimental data published in literature: YSZ:Dy [1], YSZ:Er and YSZ:Sm [2].

The measurement obtained by Phosphor Thermometry, when there is such a gradient of temperature acting on the TBC is consequently representative of a temperature that can be found at a subsurface location. Indeed, the luminescence arising from a point at higher temperature will have smaller decay constant than that of the luminescence arising from a point at lower temperature, as represented in Figure 3.9 ($\tau_1 < \tau_2 < \tau_3$). Thus, the collectable luminescence at the TBC surface is the result of distinct signals coming from in-depth locations into the doped coating with different decay constants. The exponential decay of the luminescence arising from different positions of the TBC is integrated with the Kubelka-Munk model to predict the decay of the collectable luminescence.

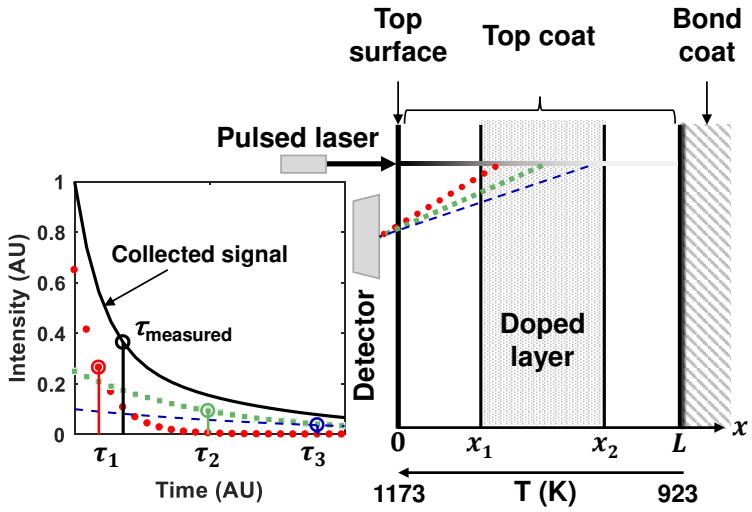

Figure 3.9: Decay of phosphor luminescence intensity arising from different positions of the TBC with temperature gradation across the coating.

To account for the variation of the decay time of the luminescence at each location in the TBC, the governing equation were modified (refer to Equation 3.2), so that it includes the luminescence decay contribution, as given in Equation 3.5.

$$\begin{Bmatrix} I'_{lum} \\ J'_{lum} \end{Bmatrix} = \begin{bmatrix} -(K_{lum}+S_{lum}) & S_{lum} \\ -S_{lum} & K_{lum}+S_{lum} \end{bmatrix} \begin{Bmatrix} I_{lum} \\ J_{lum} \end{Bmatrix} + \phi(x,t) \begin{bmatrix} \frac{qK_{laser}}{2} & \frac{qK_{laser}}{2} \\ -\frac{qK_{laser}}{2} & -\frac{qK_{laser}}{2} \end{bmatrix} \begin{Bmatrix} I_{laser} \\ J_{laser} \end{Bmatrix} \tag{3.5}$$

where, $\phi(x,t) = e^{-t/\tau(x)}$. In this exponential decay relation, t is the real time and $\tau(x)$ is the decay constant of the luminescence arising from different positions x. The decay

constant $\tau(x)$ depends on the position due to the existing temperature gradient across the TBC. This decay form has been motivated by the monoexponential decay behavior of the luminescence of the dopants considered in this study [173, 174, 175].

The time-dependent luminescence coming from different positions of the TBC with the fully doped layer configuration **(C1)** and the TBC with an embedded thin doped layer configuration **(C2)** is shown in Figure 3.10, and up to 4 μs. As it can be observed from the figure, the part of the luminescence coming from the area close to the top surface emerges with a higher intensity but decays rapidly. On the other hand, the luminescence coming from a more buried position into the TBC has a smaller intensity, but decays slower. The decay of the collectable luminescence $(J_{lum}(x=0))$ can be then fitted using a single-exponential model: $J_0(t) = J_0(t=0)e^{-t/\tau_{eq}}$.

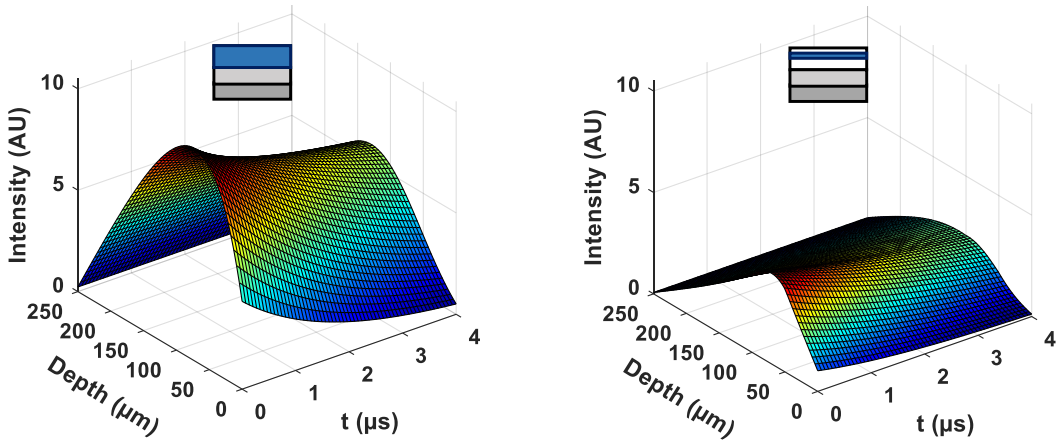

(a) **(C1)** (b) **(C2)**

Figure 3.10: Time dependent luminescence at different positions in the TBC obtained from the modified Kubelka-Munk model for (a) fully doped TBC **(C1)** and (b) TBC with a 50 μm doped layer at a depth of 50 μm **(C2)** of YSZ:Dy.

The decay of the collectable luminescence from the two TBC configurations **(C1)** and **(C2)** are shown in Figures 3.11(a) and 3.11(b), respectively. The results that are presented are based on the simulations using YSZ:Dy as the doped material. The luminescence decay that is expected to be generated at both edges of the doped layer are also shown in the figure. In the case of the fully doped TBC configuration **(C1)**, the edges correspond to the surface of the TBC and the bond coat.

It can be noted that the equivalent decay constant of the collectable luminescence has a value in between those of the luminescence from the edges of the doped layer which

means that the collectable signal indicates a temperature in a specific location into the doped layer.

The decay constant of the collectable luminescence for the configuration **(C1)** is computed to be 1.67 μs, while those of the luminescence arising from the TBC surface and from the top coat - bond coat interface are computed to be 0.87 μs and 65.69 μs, respectively. In the configuration **(C2)**, the decay constant of the collectable luminescence is 2.89 μs and that of the luminescence arising from both edges of the doped layer are 2.06 μs and 4.90 μs, respectively. The equivalent decay constant can be experimentally measured and can be used for the validation of this model. The decay constant (τ_{eq}) of the collectable luminescence is further correlated to a particular position, named here equivalent position. This position represents the sub-surface location from which the luminescence decay is similar to that of the collectable luminescence. In other words, it represents the location that is measured using Phosphor Thermometry.

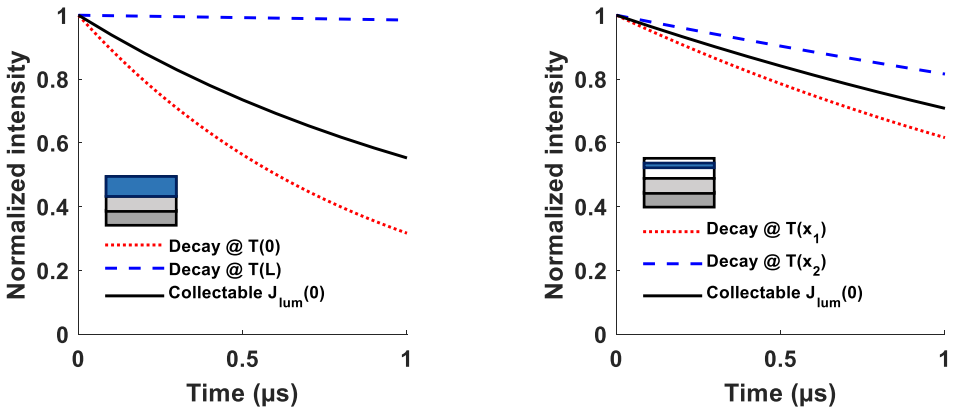

(a) **(C1)** (b) **(C2)**

Figure 3.11: Decay of the luminescence from different positions in (a) fully doped TBC and (b) TBC with a 50 μm doped layer at a depth of 50 μm of YSZ:Dy.

In order to compare the application of different materials, the modified model has been applied to the TBC configurations with three doped materials, YSZ:Dy, YSZ:Er and YSZ:Sm. These rare-earth dopants are chosen for this study since these have been demonstrated potential material for Phosphor Thermometry applications and are applicable to a fairly high temperature of around 900°C. The collectable intensity and equivalent position are presented together in Figure 3.12 for all the possible positions and thicknesses of the doped layer in the top coat of the TBC. Each map was prepared from the simulation results using the modified Kubelka-Munk model for 325 different geometries by systematically varying the position from $x = 0$ μm to $x = 250$ μm and the thickness from $h = 250 - x$ μm with a step size of $x = 10$ μm. For the YSZ:Dy system, the equivalent position is

found to be 38 μm for the configuration containing a fully doped top layer **(C1)**. This means that when sending an excitation pulse to a Dy-doped top coat of thickness 250 μm, the Phosphor Thermometry instrument gets a sginal indicating the temperature at approximately 38 μm from the top surface. For YSZ:Er and YSZ:Sm, the equivalent positions are 53 μm and 47 μm, respectively. Consequently, it is shown that the equivalent position can be controled by tailoring the TBC configuration. For example, using a YSZ:Dy doped layer in the configuration **(C2)**, the equivalent position results to be 70 μm while it can be moved to 119 μm by positioning the same 50 μm thick doped layer at a depth of 100 μm. However, while displacing the doped layer from an initial depth of 50 μm to 100 μm, the collectable luminescence at the TBC surface is reduced from 1.00 % to 0.34 % of the incident laser intensity, for the given quantum efficiency. The presented maps help to understand the simultaneous effects of modifying the geometry on the final collectable intensity and equivalent position (or estimated sub-surface location), using Phosphor Thermometry.

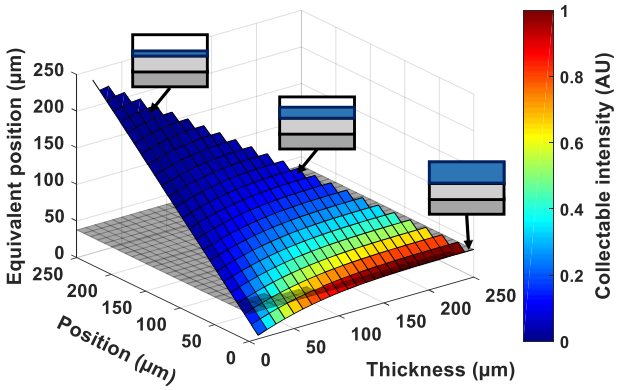

(a) **YSZ:Dy**

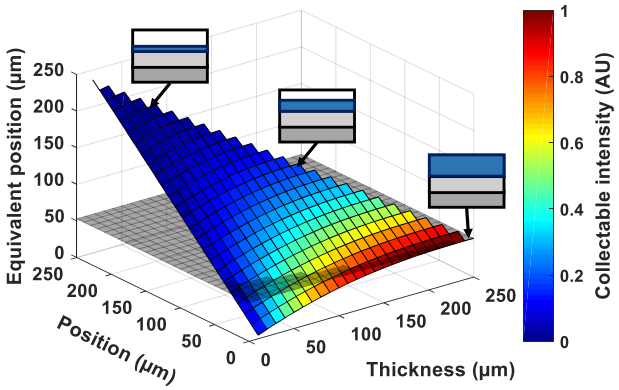

(b) **YSZ:Er**

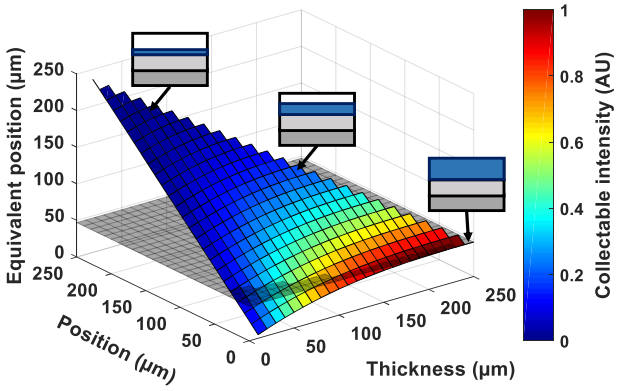

(c) **YSZ:Sm**

Figure 3.12: Equivalent position (sub-surface location) of temperature measurement and collectable intensity results for varying geometries of the TBC configuration.

The results of equivalent decay constants, obtained after fitting the convoluted signal, for two layered configurations of the TBCs, and made with different doped materials, are presented in Figure 3.13. Figure 3.13(a) shows the comparison of equivalent positions and decay constants of the collectable luminescence of the TBC configuration that contains a fully doped top layer **(C1)** and those for the configuration with a 50 μm thick doped layer at a depth of 50 μm **(C2)** are shown in Figure 3.13(b). It can be noted that, for the fully doped configuration **(C1)**, YSZ:Er provides the temperature representative of the most in-depth position into the coating - 53 μm among the three dopants. However, in the configuration with a 50 μm doped layer at a depth of 50 μm, the temperature is obtained from nearly similar depth in the coating. The equivalent depth being 70 μm, 72 μm, and 71 μm for the Dy, Er, and Sm dopants, respectively. The equivalent decay constant of the luminescence using Sm is the highest being 5.1 μs and that using Dy and Er are determined to be 1.7 μs and 1.8 μs, respectively, in fully doped configuration. This is due to the inherent longer decay time of the dopant Sm than the other two dopants in this temperature range (refer Figure 3.8). This feature is conserved in the multilayered configuration also, in which the YSZ:Sm exhibits the higest decay constant. Within the multi-layered TBC configuration, YSZ:Er can provide better temporal resolution due to its smaller decay constant while probing similar in-depth position like the other two materials.

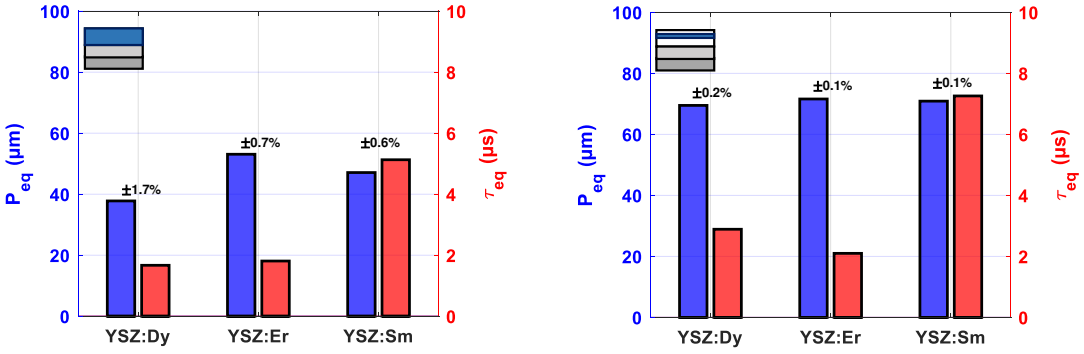

(a) **(C1)** (b) **(C2)**

Figure 3.13: Intensity and equivalent decay constants of collectable luminescence from the TBC configurations with different materials (a) fully doped top coat **(C1)** and (b) a 50 μm thick doped layer at a depth of 50 μm. The error bar represent the error in fitting the collectable luminescence to determine the equivalent position and decay constant.

3.3 Model sensitivity to thermal parameters

The modeling work up to this point demonstrates the feasibility of predicting, for a known TBC layer configuration, the luminescence intensity that can be collected as well as the sub-surface location that is measured by Phosphor Thermometry, using the lifetime decay method. However, the results obtained in the previous parts are necessarily associated with the boundary conditions that were selected for the numerical study. In particular, the TBC surface temperature and the gradient were fixed, so the temperature at any point in depth into the coating was known, which is generally not the case in experimental conditions. To determine of the previous models can be used as a supportive tool for real

temperature measurements, it is crucial to evaluate the sensitivity of the model to thermal parameters, namely the temperature at the surface of the TBC and the thermal gradient acting through the TBC. This sensitivity study is important to justify of the potential applicability of models to predict accurately sub-surface locations that are corresponding to temperature measurement depths using Phosphor Thermometry. This would open the way to thick sensing layers as they produce higher luminescence intensities.

For this study, the intensity and decay behavior have been modeled in 250 μm-thick luminescent coatings. YSZ:Dy, YSZ:Er and YSZ:Sm fully doped TBCs were used, as in the previous results, for comparison. The extended Kubelka-Munk model was used with the same optical properties as in the previous simulations, given in Table 3.1. Multiple simulations were run with varying the boundary conditions so that the top surface temperature (T_0) ranges from 973 to 1473 K and the thermal gradient ranges from 0.2 to 1 K/μm. The resulting convoluted luminescence decay, emerging from multiple sub-surface locations exposed at different temperature conditions, are fitted over the time range 0 - 1 μs, using a single-exponential decay model. The obtained decay constant was converted to the corresponding temperature using the known time-response of the phosphor (refer to Figure 3.8). This ultimately allows to determine the sub-surface location that is being measured by Phosphor Thermometry. Results are presented in Figure 3.14 and show the high sensitivity of the measured sub-surface location P_{eq} in YSZ:Dy to the surface temperature

and the thermal gradient, at temperatures exceeding 1300 K, which is anyways unpractical using the decay method as the luminescence of the phosphor is quenched. For YSZ:Dy, with a surface temperature that is inferior to 1300 K and for YSZ:Er and YSZ:Sm, for any surface temperature or any gradient, the sub-surface location that is expected to be measured with Phosphor Thermometry remains almost constant. This is an essential piece of information that can be used to extend the capabilities of the existing methods for temperature characterization in TBCs. The insensitivity of the equivalent position to thermal parameters potentially allows for direct measurements using thick luminescent sensors, revealing sub-surface temperature and internal thermal gradients.

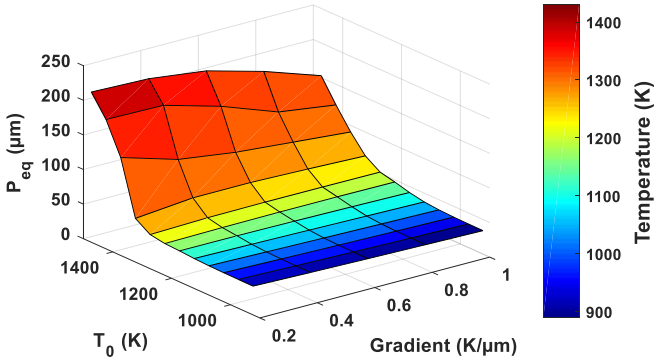

(a) **YSZ:Dy**

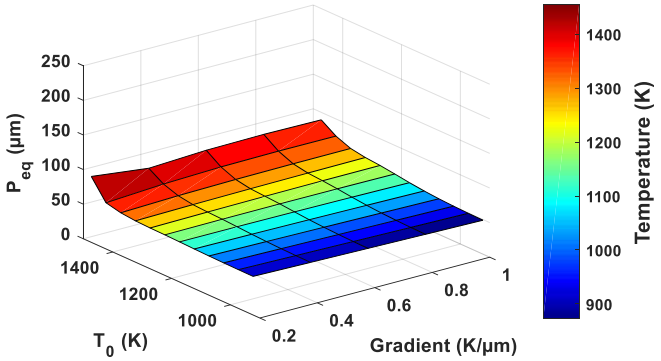

(b) **YSZ:Er**

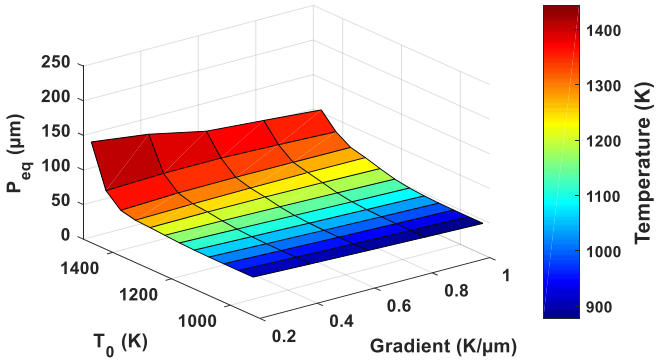

(c) **YSZ:Sm**

Figure 3.14: Sensitivity of the equivalent position (sub-surface location) of temperature measurement to the gradient of temperature applied through the coating and the surface temperature.

3.4 Delamination progression modeling

Controlling the integrity of Thermal Barrier Coatings is essential to ensure the smooth running of the turbine systems in the most efficient way with optimized maintenance. Ensuring the integrity of the coatings is crucial for the proper functioning of the turbine systems and recent progress has been made on the improvement of optical-based methods for delamination detection. The drastic change in reflectivity occurring when a delamination forms can be used for high-contrast luminescence mapping. To this objective, optical imaging have been extensively used to reveal delamination progression on coatings, in particular using the thermal radiation emitted in the mid-infrared [176] as well as luminescence-based mapping [177, 178, 179]. The latter is made possible by the integration of rare-earth elements into the top coat which allows to perform high-contrast and high-resolution imaging for the monitoring of the components after being used in extreme environments [180]. In this work, the four-flux Kubelka-Munk model described in the previous parts has been used and further extended in this section to predict luminescence intensity variation caused by delamination and spallation, by estimating numerically the luminescence intensity for both an intact coating and a delaminated coating. The validation of this model was completed using two TBC configurations that contain an Erbium doped layer for delamination sensing. An artificial delamination was created by Rockwell indentation on both samples and each of them has been monitored by measuring the

change of intensity of the luminescence emerging at the top surface induced by the higher internal reflectivity in presence of coating debonding areas. For the first sample (sample A), the doped layer was deposited at the top of the TBC to significantly increase the intensity of the luminescence that can be collected by the detector [113] and, therefore, to reduce the acquisition time for mapping the surface of the samples. This configuration is also advantageous for erosion indication as the sensing layer on the surface is directly exposed to the extreme environments [181, 182]. In addition, when doping YSZ for luminescence sensing, the concentration increase of trivalent dopant of similar ionic radii [183] (summation of rare-earth luminescent activators and Yttrium stabilizer) into zirconia may affect the prominence of the metastable tetragonal phase of zirconia often leading to a reduced lifetime [184]. The positioning of the doped layer on the top of the TBC ensures the integrity of the underneath standard coating. On the other hand, the doped layer in the second sample (sample B) was placed at the bottom of the ceramic top coat, at the interface with the bond coat for maximum contrast and resolution of the delamination tracking. The current literature presents results on configurations similar to the second sample exclusively.

The samples considered in this study are represented in Figure 3.15(a) and are embedding a thin sensing layer as an indicator for underneath delamination. They are both consisting of a Rene N5 superalloy substrate, a NiPtAl bond coat, a standard 125 μm

8 wt.% Yttria-Stabilized Zirconia (YSZ) Electron-Beam Physical Vapor Deposition (EB-PVD) TBC and an additional 12.5 μm EB-PVD layer composed of Erbium doped YSZ (YSZ:Er^{3+}). This doped layer is placed at the top and at the bottom of the undoped top coat, for sample A and B, respectively. For sample A, the sensing layer was placed on the surface of the TBC to obtain a higher luminescence intensity, as the produced radiation is not blocked by any intermediate non-luminescent coating, for the ease of data collection as well as to avoid any interaction between the bond coat and the sensing layer. Moreover, this material configuration has not been reported in literature for delamination, erosion, or spallation detection and is therefore intended to demonstrate its applicability for delamination monitoring. For sample B, the sensing layer was placed at the interface with the bond coat to maximize the effect of internal reflectivity variations that occur with delamination growth. The delamination areas on the samples were created artificially by Rockwell indentation. For sample A, a 2.45 kN load was applied normal to the surface and resulted in the spallation of the coating at the indentation spot and the delamination of the surrounding area on about 12 mm^2. For sample B, a 1.96 kN load was applied and resulted in the delamination of the surrounding area on about 7 mm^2. As the as-deposited EB-PVD coatings are oxygen deficient and to restore the crystallinity of ZrO_2, samples were annealed at 1000°C for 3 h in air to enhance luminescence.

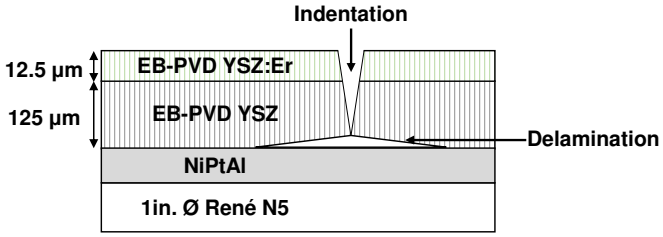

(a) Sample A, with doped layer at the top surface.

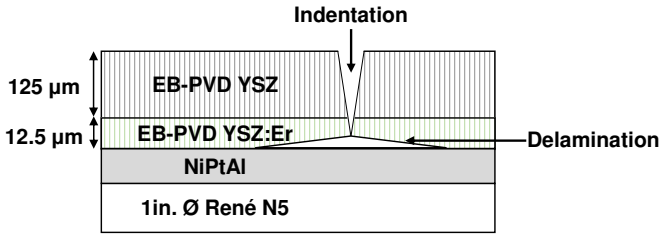

(b) Sample B, with doped layer at the bottom of the top coat.

Figure 3.15: Layer configurations of the TBC with a luminescent layer that can detect the presence of underneath delamination.

The four-flux Kubelka-Munk model is a radiative transport model that was applied to the material configurations described above to get a numerical estimation of the laser excitation and luminescence emission intensities at any point into the coating. This model considers the radiative properties of EB-PVD YSZ obtained from experimental results found in literature [4, 5]. Specifically, for a given incident laser excitation intensity on the top surface of the TBC, the luminescence intensity emerging out at the top surface and originally emitted from the sensing layer is calculated based on the internal reflection in

the coating as well as the absorption and the scattering coefficients taken at the specific excitation and emission wavelengths. The doped layer is assumed to have the same optical properties than the standard undoped EB-PVD YSZ. Consequently, the whole ceramic top coat is assumed to be homogeneous with no interface between doped and undoped layers.

The model diagram including boundary conditions and definitions are presented in Figure 3.3. In this model, light is traveling along the x-axis, corresponding to the normal to the surface of the TBC, in two opposite directions: the light vector component oriented towards the bond coat is denoted by I and the light vector component oriented back to the top surface of the TBC is denoted by J. The four-flux model differentiates both excitation and emission wavelengths to solve for the laser (labeled *laser*) and luminescence (labeled *lum*) intensities separately. The generalized coefficients K and S that account for the bidirectional path of light are calculated from the absorption and scattering coefficients, respectively k and s, given in Table 3.3 and such as $K = 2 \cdot k$ and $S = 2 \cdot s$. These parameters are assumed to be isotropic and the coefficients uniform.

Table 3.3: Scattering [4] and absorption coefficients [5] of as-deposited EB-PVD YSZ from experimental data published in literature, digitized and considered at the wavelengths of interest for this study.

λ **(nm)**	**Scattering coefficient** s **(m^{-1})**	**Absorption coefficient** k **(m^{-1})**
532	12965	407
562	12107	319

Equation 3.1 is used to solve for the distribution of the laser intensities into the coating.

The luminescence is assumed to occur exclusively due to the excitation of the sensing layer by the laser, so it can be originated by I_{laser} or J_{laser}. Therefore, Equations 3.6a and 3.6b are used to solve for the distribution of the luminescence intensities into the coatings, for sample A and B, respectively.

$$\begin{Bmatrix} I'_{lum} \\ J'_{lum} \end{Bmatrix} = \begin{bmatrix} -(K_{lum}+S_{lum}) & S_{lum} \\ -S_{lum} & K_{lum}+S_{lum} \end{bmatrix} \begin{Bmatrix} I_{lum} \\ J_{lum} \end{Bmatrix} + \mathscr{H}(x)\cdot\mathscr{H}(t-x) \begin{bmatrix} \frac{qK_{laser}}{2} & \frac{qK_{laser}}{2} \\ -\frac{qK_{laser}}{2} & -\frac{qK_{laser}}{2} \end{bmatrix} \begin{Bmatrix} I_{laser} \\ J_{laser} \end{Bmatrix} \tag{3.6a}$$

$$\begin{Bmatrix} I'_{lum} \\ J'_{lum} \end{Bmatrix} = \begin{bmatrix} -(K_{lum}+S_{lum}) & S_{lum} \\ -S_{lum} & K_{lum}+S_{lum} \end{bmatrix} \begin{Bmatrix} I_{lum} \\ J_{lum} \end{Bmatrix} + \mathscr{H}(x+t-L)\cdot\mathscr{H}(L-x) \begin{bmatrix} \frac{qK_{laser}}{2} & \frac{qK_{laser}}{2} \\ -\frac{qK_{laser}}{2} & -\frac{qK_{laser}}{2} \end{bmatrix} \begin{Bmatrix} I_{laser} \\ J_{laser} \end{Bmatrix} \tag{3.6b}$$

where I'_{lum} and J'_{lum} denote differentiation of I_{lum} and J_{lum} with respect to x, respectively, q is the quantum efficiency of the luminescent dopant, which is assumed to be 0.5 [168], $\mathscr{H}$ is the Heaviside function, t is the thickness of the luminescent coating embed-

ded into the TBC and L is the overall thickness of the top coat (combining undoped and doped layer thicknesses).

The boundary conditions are defined at the top surface, where the percent intensity of the incident laser light is set to $I_{laser}(x = 0) = 100\%$ and there is no external luminescence input at the surface so that $I_{lum}(x = 0) = 0\%$. The boundary conditions for the interface located at the bottom of the top coat accounts for the internal reflection with either the bond coat, for an intact coating, or air, in the case of delamination. For the case of an intact coating, the reflectivity R is fixed to 4% [180], and is assumed to remain constant between 562 and 532 nm. For the case corresponding to a complete delamination, Equation 3.7 defines the reflectivity for diffuse external radiation at the air/coating interface which can be calculated by applying the integrated average of the Fresnel equation [185, 186] and is used in Equation 3.8 to obtain the reflectivity R at the interface YSZ/air. The refractive index of EB-PVD YSZ is given in Table 3.4 and, by definition, n_{air} = 1. The value of reflectivity obtained at 532 nm is 82% and at 562 nm is 83%, for the case of a delamination (for which the gap thickness is assumed to be larger than the wavelength).

Table 3.4: Refractive index of EB-PVD YSZ [6], digitized and considered at the wavelengths of interest for this study.

λ (nm)	n_{YSZ}
532	2.17
562	2.16

$$\begin{aligned}\rho_0(n) =& \frac{1}{2} + \frac{(3n+1)\cdot(n-1)}{6\cdot(n+1)^2} + \frac{n^2\cdot(n^2-1)^2}{(n^2+1)^3}\cdot ln(\frac{n-1}{n+1}) \\ &- \frac{2n^3\cdot(n^2+2n-1)}{(n^2+1)\cdot(n^4-1)} + \frac{8n^4\cdot(n^4+1)}{(n^2+1)\cdot(n^4-1)^2}\cdot ln(n)\end{aligned} \tag{3.7}$$

$$R = 1 - \frac{1}{n^2}\cdot(1-\rho_0(n)) \tag{3.8}$$

where ρ_0 is the diffuse external radiation at the air / top coat interface, n is the refractive index of YSZ and R is the internal diffuse reflectivity.

The solutions provided by the four-flux Kubelka-Munk model are used to display the distribution of light intensities at the two distinct wavelengths considered in this study. At any point into the coating, the radiation intensity is calculated based on absorption, scattering and internal reflection. The results for the laser intensity are presented in Figure 3.16. It can be highlighted that, in presence of a delamination (case presented in red), there is a significant difference in the intensity of light traveling back to the top surface (J_{laser}). The additional excitation intensity in the doped layers contributes to the higher intensity of luminescence produced in the sensing layers. For sample A, in the doped layer, the increase of the intensity of the backscattered laser radiation J_{laser} contributes almost exclusively to the gain in excitation intensity that is available for the production of luminescence. For sample B, in the doped layer, the summation of the integrated intensities of the incoming

laser radiation I_{laser} and the backscattered laser radiation J_{laser} is drastically increased in presence of a delamination, largely contributing to the higher intensity of luminescence. The results of the model for the luminescence intensities for sample A and B are presented in Figure 3.17 and 3.18, respectively. It can be seen that there is an overall increase of luminescence intensity when a delamination is present. This is due to both the higher amount of laser excitation energy available, as described above, but also to the greater reflection of the luminescence radiation itself, at the bottom of the top coat. The particular value of interest on the graphs is $J_{lum}(x = 0)$ and is reported in Table 3.5. It corresponds to the measurable luminescence intensity that is emerging from the top surface and that can be collected by a detector.

Table 3.5: Results of the four-flux Kubelka-Munk model for the luminescence intensity emerging out at the surface for both samples.

% of incident laser intensity	**Sample A**	**Sample B**
$J_{lum}(x = 0)$ delamination	0.775	0.187
$J_{lum}(x = 0)$ no delamination	0.695	0.017

The deviation between the values found for the luminescence intensity in the case of a delamination and for an intact coating corresponds to the maximum increment that can be obtained due to the change of internal reflectivity taken at the two extreme limits: in the case of a large air gap that has a thickness bigger than the wavelength so that the light is not interfering with the underneath bond coat material.

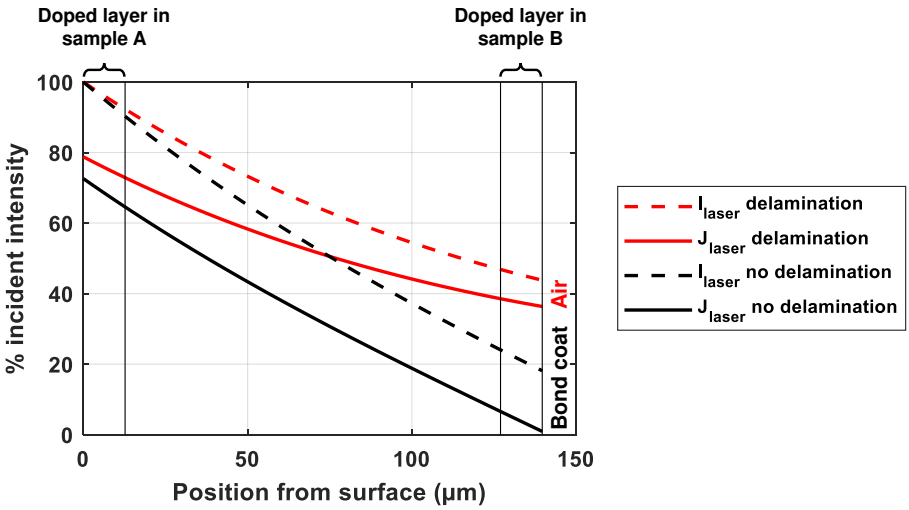

Figure 3.16: Modeled distribution of the laser light intensity into the TBC. In the case where there is delamination, higher intensities are scattered back due to increased reflectivity. The location of the doped layer for samples A and B is represented on the same figure.

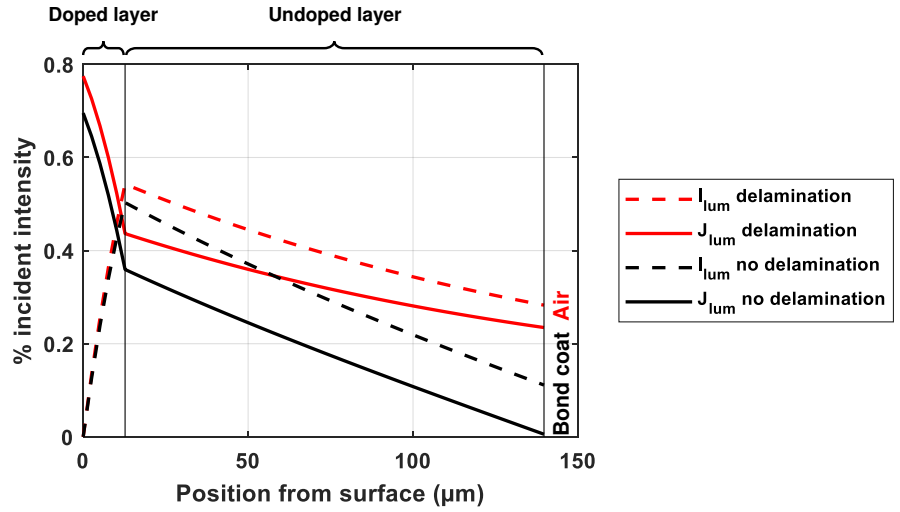

Figure 3.17: Modeled distribution of the luminescence intensity into the TBC. In the case where there is delamination, a higher luminescence intensity is expected.

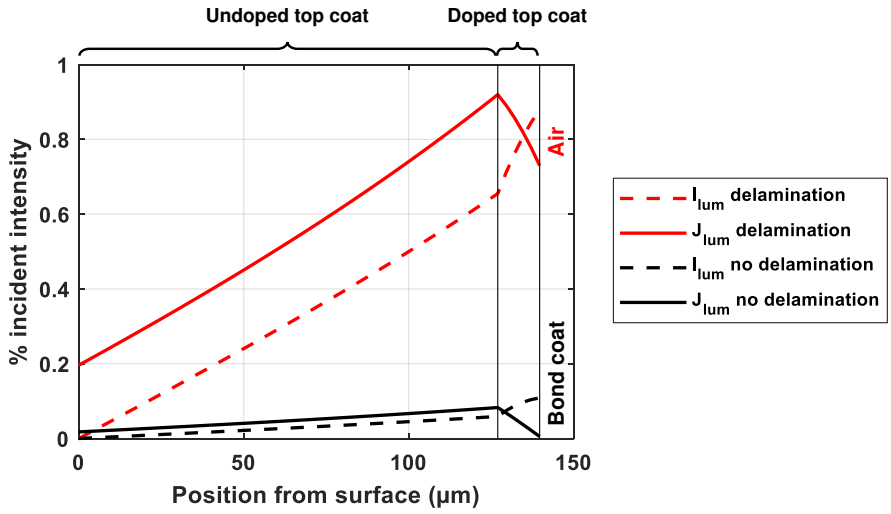

Figure 3.18: Modeled distribution of the luminescence intensity into the TBC. In the case where there is delamination, a higher luminescence intensity is expected.

The data acquisition was done using a photoluminescence piezospectrocopy instrument [187] that uses a 15 mW 532 nm laser and a Pixis 100 (Princeton Instruments) for the collection of the spectrum. It is capable of fast scanning over the surface of the sample by the means of an XYZ stage. This instrument has been successfully used for damage identification through piezospectroscopic stress evaluation using the R-line emission of alumina [188, 189, 190, 191, 192, 193, 194, 195, 196, 197]. For this study, the wavelength range was adjusted to 540 - 580 nm to collect the Er-lines and the instrument was calibrated using a Hg lamp. The TBC samples, that both contain a delamination area induced by Rockwell indentation, as shown in Figure 3.19, were mounted on a vertical support and aligned normally to the laser beam. The spectral intensity was recorded over the sur-

face of the samples with step increments of 200 μm to cover the area represented in the insert boxed in red. The emission peak at 562 nm, corresponding to the transition $^4S_{3/2}$ $\rightarrow$ $^4I_{15/2}$ of Erbium, was fitted using a linear baseline removal. The intensity maps of the samples were obtained and are presented in Figure 3.20. In both cases, delamination areas can be detected easily due to sharp increases in intensity. This high-contrast delamination zones demonstrates the applicability of this technique on curved surfaces. In contrast, foreign objects like dust that are deposited on the surface or partial erosion can contribute to a progressive decrease of the luminescence intensity in localized areas. The current luminescence mapping of the TBC shows that some defects can be detected as they are associated with a very reduced luminescence intensity. Furthermore, the spallation area results in zero luminescence and is presented in gray on the intensity map. Total erosion of the sensing layer would eventually produce the same result so visual inspection in this case would determine the situation of the coating. Table 3.6 allows for the comparison of both the model and the experimental results. For the obtained map corresponding to the experiment, the average of 10 measurements into the delamination area was compared to the average of 10 measurements outside this area and the error presented in Table 3.6 corresponds to the standard deviation over these points.

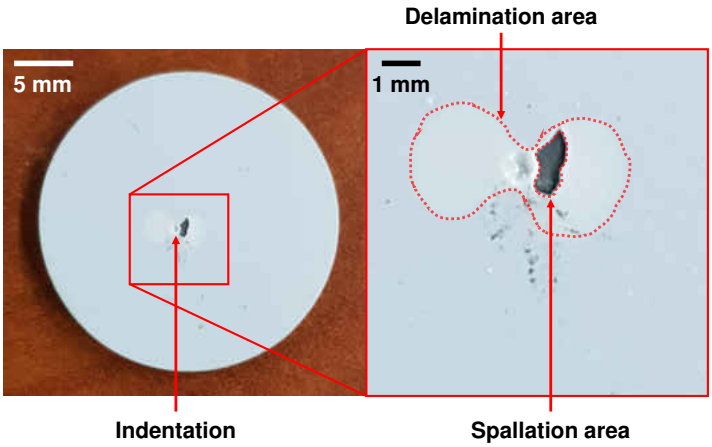

(a) Sample A, with doped layer at the top surface.

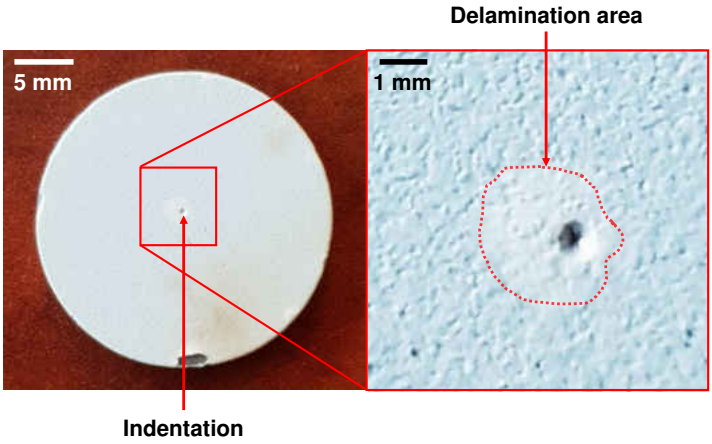

(b) Sample B, with doped layer at the bottom of the top coat.

Figure 3.19: Rockwell indentation with visible induced delamination areas.

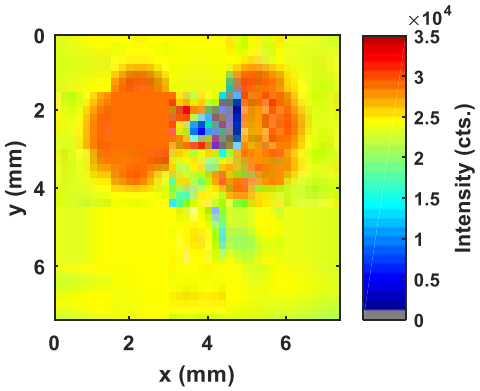

(a) Sample A, with doped layer at the top surface. 5 ms exposure time.

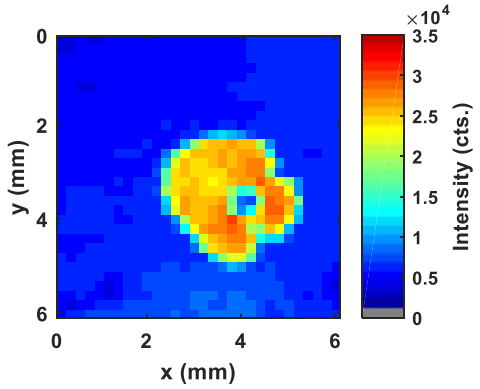

(b) Sample B, with doped layer at the bottom of the top coat. 100 ms exposure time.

Figure 3.20: Luminescence intensity of the Er-line at 562 nm, highlighting the delaminated zones with higher intensity.

Table 3.6: Comparison of model and experiment for the luminescence intensity increase due to delamination.

%	**Sample A**	**Sample B**
Kubelka-Munk model	11.4	988.9
Experimental measurement	17.4 ± 2.1	381.5 ± 47.4

Although the sensing layer is not in direct contact with the delamination, the increase of internal reflectivity at the bottom of the ceramic top coat that is associated with the debonding of the ceramic top coat produces a noticeable increase of luminescence intensity. The indentation location shows a reduced luminescence intensity due to the partial compaction and angling of the sensing layer that contributes to the emission of signal in an increased area.

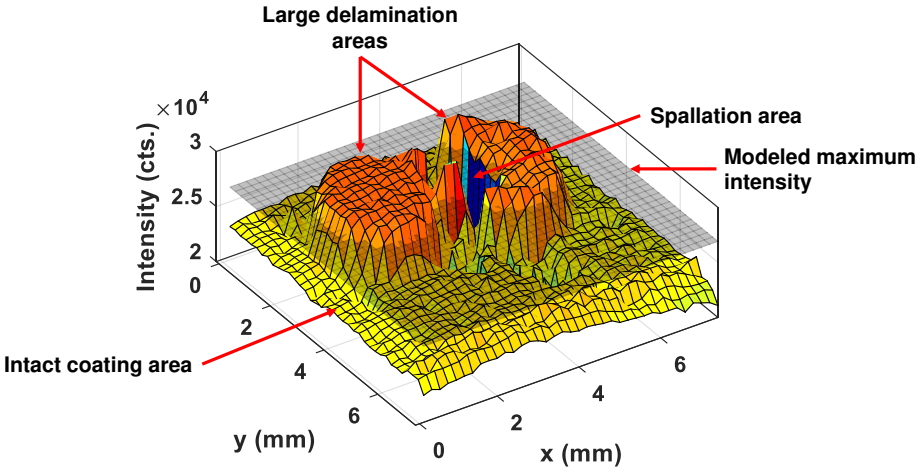

(a) Sample A, with doped layer at the top surface.

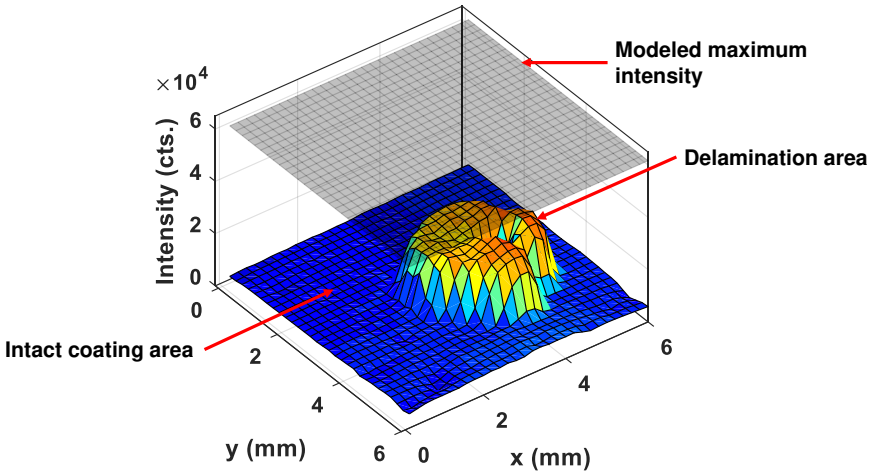

(b) Sample B, with doped layer at the bottom of the top coat.

Figure 3.21: Delamination monitoring by luminescence intensity mapping. The maximum intensity limit calculated with the Kubelka-Munk model for a large delamination is indicated in gray.

The Kubelka-Munk model presented in this work can be used as a support for the tracking of coating delamination progression. For example, applying a safety margin to the maximum intensity predicted by the model could allow for a better characterization of the gravity of delamination on the affected coatings. Figure 3.21 shows the delamination progression of samples A and B. For sample A, the high indentation load led to a large coating debonding, creating an important air gap in between the top coat and the bond coat. This results in a strong luminescence increase for which the model underestimated its absolute maximum limit. This could be due to the assumptions and simplifications on the model as well as the inaccuracy of the coefficients selected for the material. The samples of this study might have in reality a smaller scattering or absorption coefficient than the value found in literature and used for the calculation of this model. Selecting a reduced value for these coefficients would result in an overall increase of luminescence intensity and a higher maximum contrast when comparing the luminescence emerging off of a delamination area and an intact coating area.

3.5 Conclusions of the chapter

Phosphor thermometry is a promising non-destructive method for accurate temperature measurement using phosphor elements that emit temperature-dependent luminescence.

The method relies on the intensity and decay of luminescence arising from the phosphor elements upon excitation by an incident laser. In this work, the classical Kubelka-Munk model has been extended to model the luminescence emitted from phosphor elements that are added into Thermal Barrier Coatings (TBCs) to enable temperature sensing using phosphor thermometry. In addition, the collectable luminescence and its time decay behavior emerging from a tailorable multi-layer TBC configuration have been predicted for different rare-earth dopants: Dy, Er and Sm within an Yttria-Stabilized Zirconia (YSZ) host, and with an operational gradient of temperature acting through its depth. The configurations have been designed by varying the position and thickness of the doped layer into the coating. The decay constant of the collectable luminescence has been used to determine the position in the coating from where the luminescence decay is the same as the decay of the collectable signal. This subsurface position indicates the location at which the temperature measurement is performed using phosphor thermometry under realistic operating conditions. It has been determined that YSZ:Dy provides the highest intensity of the collectable luminescence among the three dopant materials. In the TBC configuration with a fully doped coating, using YSZ:Er as a sensor enables temperature measurement from a more in-depth position into the coating. It has been shown that this position can be tailored by adjusting the geometrical configuration of the TBCs, varying the position and thickness of the doped layer. Due to the sensitivity of the dopants to the temperature, the decay be-

havior of the emerging luminescence varies for different TBC configurations. The model can be used in screening the dopants to design multilayered TBCs for their suitability in temperature sensing by Phosphor Thermometry.

The luminescence behavior of different temperature sensitive TBCs containing rare-earth dopants was studied using the four-flux Kubelka-Munk model. Different configurations that are suitable for non-invasive temperature sensing by phosphor thermometry were considered: YSZ:Dy, YSZ:Er and YSZ:Sm. The existing gradient of temperature that acts through the thickness of the coating contributes to the convolution of the collectable luminescence decay reaching the surface of the TBC. The derived decay constant has been used to infer an equivalent position into the TBC, providing an accurate indicator of the location that is representative of the temperature measurement.

It was also shown how tailoring the geometric configuration of the TBC allows for tuning the intensity, the equivalent position and the decay constant of the emerging luminescence:

- It was found that the increase of thickness for a doped layer placed on the top of the TBC results in an increase of the collectable luminescence intensity until a certain threshold that indicates a limit of detection in the depth of the coating, located between 150 and 200 μm for YSZ:Dy.

- Among the three doped materials considered, YSZ:Dy was found to exhibit the highest luminescence intensity (around 3 times more than the other two materials) at the TBC surface, for an equal quantum efficiency.

- For the fully doped TBC configuration, the equivalent position is found to be the most in-depth for YSZ:Er, while larger decay constant was exhibited by YSZ:Sm by its inherent decay characteristics.

The model developed here can be applied to study the feasibility of using phosphor materials in a multilayered TBC configuration. The model enables the prediction of the position and temperature of which dominates the luminescence emerging from the TBC. Thereby, this model may be further used to predict the spatial distribution of temperature across the coating using an inverse approach. The model provides insight into designing multilayer TBC configurations that are viable for non-invasive temperature measurement with required luminescence intensity and decay behavior prior to testing. In the future, experiments will be conducted to compare measurements to the results presented.

The modified Kubelka-Munk model has been used to study the luminescence behavior of a doped TBC for which the entire top coat contains doping elements. Using the predicted time dependent luminescence, it was possible to infer the position at which the temperature measurement is performed by Phosphor Thermometry. The sensitivity of this equivalent position to the surface temperature and gradient through the top coat was

found to be negligible over the range of temperature considered in this study. The results will help understand the viability of using doped TBCs for temperature sensing.

A four-flux Kubelka-Munk model has been formulated to predict the maximum theoretical luminescence intensity increase between an intact coating and a delaminated coating for which the debonding gap is bigger than the luminescence wavelength. The model outcomes were compared to experimental values that were collected on two EB-PVD TBCs that contain an embedded Erbium doped YSZ layer for delamination sensing. An artificial delamination zone created by Rockwell indentation was successfully tracked by measuring the intensity of the Erbium emission at 562 nm. The magnitudes of intensity deviation output by the model were found to be comparable to those collected experimentally. In the future, the adjustment of the parametric inputs might help obtaining more accurate results. The ratio of luminescence increase obtained experimentally and maximum luminescence increase obtained by modeling can help monitoring coating delamination progression and the model can be therefore a supporting tool to set the absolute limits for the safe utilization of TBCs. Even though the configuration including the sensing layer at the bottom of the top coat was found to have the highest contrast and resolution for delamination sensing, this work proved the applicability of the configuration integrating the

sensing layer at the top surface. Indeed, it has the advantage of having a stronger emerging luminescence, which favorizes data collection.

For the experimental validation of the previously described model, a sample plan was elaborated to support the main modeling results.

CHAPTER 4
MANUFACTURING OF RARE-EARTH DOPED THERMAL BARRIER COATING CONFIGURATIONS

The models discussed in the previous chapter were used to understand the TBC parameters that influence luminescence parameters for Phosphor Thermometry. Sample configurations were designed based on results found in literature and to validate modeling results.

4.1 Fabrication of rare-earth doped YSZ samples

The samples were fabricated using an SGT-100 (Praxair) spray gun at the Air Plasma Spray facility of the Florida Institute of Technology. Directionally solidified CM247 nickel-based superalloy substrate disks were provided by Siemens Energy. This material was chosen as it is commonly used in combination with APS TBCs in the hot sections of land-based turbine systems [198]. The standard coupon dimensioning was selected for high temperature testing, with a diameter and thickness of 25.4 mm and 3 mm, respectively. The substrates were grit blasted prior to the deposition of the bond coat layer to

obtain appropriate surface roughness and to ensure proper adhesion. A stud was spot-welded on the back of the substrate to mount the coupon normally to the spray gun on the deposition stage. NiCrAlY bond coat powder (NI-164/NI-211, Praxair), 7-8 wt.% YSZ undoped top coat powder (ZRO-271, Praxair) and rare-earth doped YSZ top coat powders (produced by solid state reaction, Phosphor Technology Ltd.) were used for the deposition of the layers, in the configurations presented in Figure 4.1.

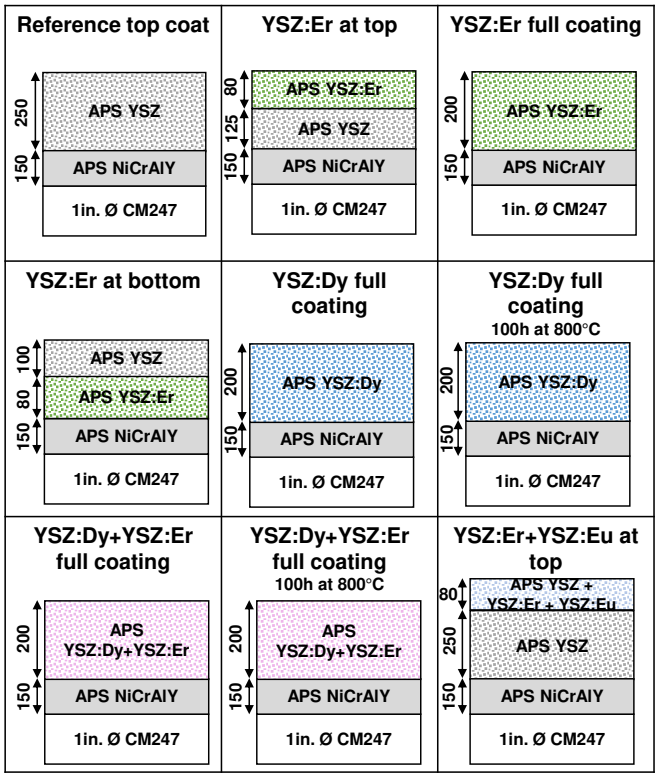

Figure 4.1: Samples manufactured at the Florida Institute of Technology using Air Plasma Spray. Thicknesses are indicated in μm.

The deposition of the doped YSZ powders turned out to be challenging due to the small particle size ($D_{50} < 1$ μm). Nanoparticles are usually preferred for the production of homogeneous doped powders, in a reasonable time scale, through cation diffusion during the solid state reaction. However, this particle size is problematic for Air Plasma Spray deposition, as indicated in Figure 1.3, because standard deposition parameters are optimized for $D_{50} \approx 30$ - 50 μm. In addition, the doped powders were found to possess irregular particle shapes, which is an additional constraint for APS deposition. To ensure the flowability of the mixture and a good deposition rate for the doped layers, doped nanoparticle powder and undoped microparticle powder were mixed so the high flowability industrial powder can act as a carrier for the doped material. The micrographs of both starting powders and the resulting mixture that was used for the deposition of luminescent layers are presented in Figure 4.2. The particle size obtained for mixture was estimated to be approximately: $D_{50} \approx 30$ μm, using the microscope scaling tool. The powders were observed with a voltage acceleration of 15 kV.

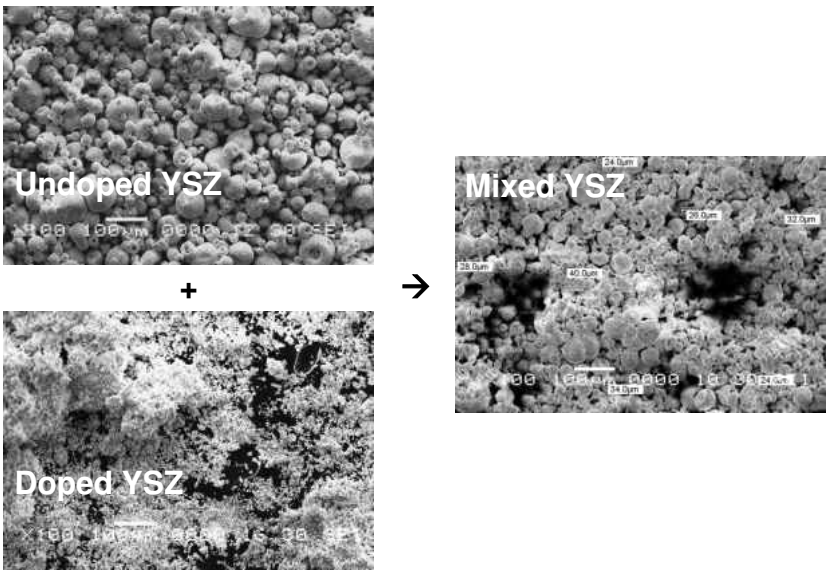

Figure 4.2: Micrographs of preprocessing powders mixed to enable the deposition of luminescent powders through Air Plasma Spray.

During the deposition process, the feeding wheel speed was decreased to get a low but consistent deposition rate which drastically reduced the clogging probability of the APS system. The parameters used for the deposition of the layered configuration are given in Table 4.1. The rare-earth dopant concentrations in YSZ were chosen for optimal luminescence intensity, based on literature [126, 150, 199] and using the Johnson-Williams equation which results are presented in Figure 2.2.

Table 4.1: Parameters used for sample fabrication through Air Plasma Spray.

	Bond coats	**Undoped top coats**	**Doped top coats**
Spray distance (cm)	10	7.5	7.5
Current (A)	802	902	902
Voltage (V)	43.3	43.7	43.7
Argon (SLM)	49.1	25.5	25.5
Helium (SLM)	20.3	20.8	20.8
Feeding wheel speed (rpm)	1.17	3.29	0.48

After the deposition of each layer, thickness measurements were performed using an eddy current thickness gauge. The thicknesses are indicated in the sample matrix, given previously in Figure 4.1. Following the deposition of the TBCs on the superalloy disks, the studs were removed and the specimens were cut into three pieces to provide:

- A circular segment for Phosphor Thermometry experiments
- A circular segment for Scanning Electron Microscopy (SEM) characterization
- A 2.5 mm width rectangular cuboid piece for transmission X-ray diffraction experiments: this width has been chosen as it is suitable for depth-resolved high-energy transmission X-ray diffraction measurements [200, 201].

4.2 An innovative configuration: Doped bond coat for TGO sensing

An innovative approach was explored in this work introducing doped bond coat configurations fabricated with the possibility of creating a sensing TGO layer. This presents a different method from the typical doped top coat ceramic coatings which is the current approach for Phosphor Thermometry applied to TBCs. Such an innovation would provide the following benefits:

- Direct measurement at the TGO layer for higher control on the thermally driven failure mechanisms associated with TGO growth;
- No additional layer to the standard TBC system that could create a mechanical interface;
- No modification of the industrial YSZ thermal barrier;
- No modification of the industrial deposition procedure with standard two-step deposition process and no increase in manufacturing costs.

Prototype doped bond coats were fabricated via APS by spraying a mixture of metallic rare-earth (Sigma-Aldrich) and standard bond coat (Praxair) powders. The concentration of rare-earth powder into NiCrAlY powder was approximately 3 - 5 wt.%. As the TGO forms through thermal aging, it is anticipated that some impurities initially present in the

bond coat migrate to the TGO, as it commonly occurs for smaller elements from the bond coat to the TGO [202]. An example of this is the migration of Chromium that contributes to the composition of the TGO, as an impurity, which enables luminescence using the α-Al_2O_3:Cr R-lines. The desired doping of alumina with rare-earth doped to provide α-Al_2O_3:Cr,RE would be used as temperature sensor at the interface between the top coat and the bond coat, which corresponds to the particular location of interest for temperature measurements in TBCs. Indeed, this temperature information would be invaluable as most of the failure mechanisms in TBCs are driven by TGO growth rate. Sol-gel rare-earth doped alumina films deposited on silicon substrates have shown positive results for the applicability of such configurations at high temperature [203]. The first set of sample configurations that were fabricated are shown in Figure 4.3. All the samples were thermally aged with 4×100 h at 800°C in order to form some TGO. In this sample matrix, standard bond coat (BC) and Dysprosium or Erbium doped bond coat configurations were compared using different top coat (TC) thicknesses: The standard 250 μm top coat was compared with 50 μm top coat or no top coat configurations that were fabricated to facilitate luminescence measurements. A second set of samples was manufactured to produce Samarium and Erbium doped bond coat samples, as presented in Figure 4.4.

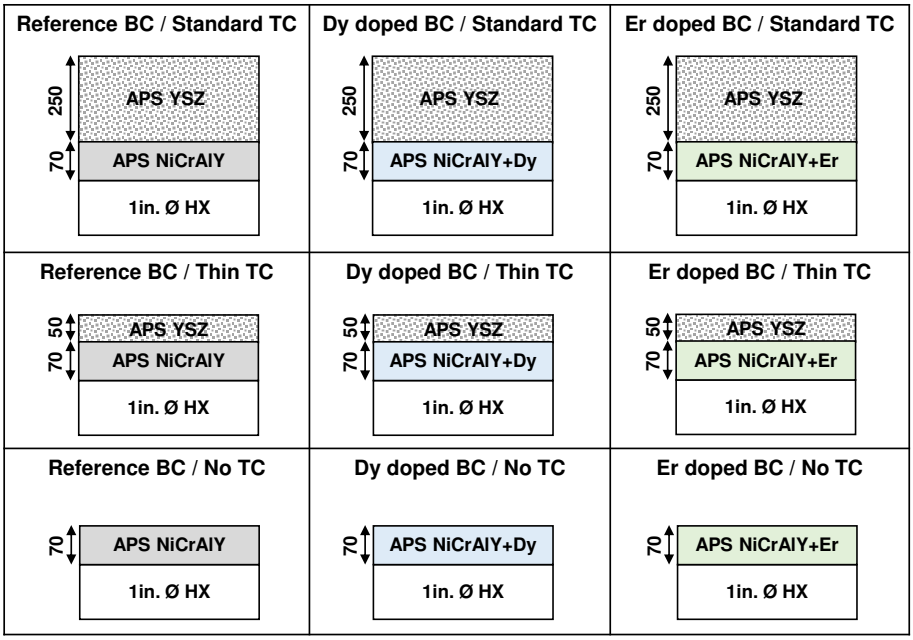

Figure 4.3: Dysprosium and Erbium doped bond coat samples manufactured at the Florida Institute of Technology using Air Plasma Spray. Thicknesses are indicated in μm.

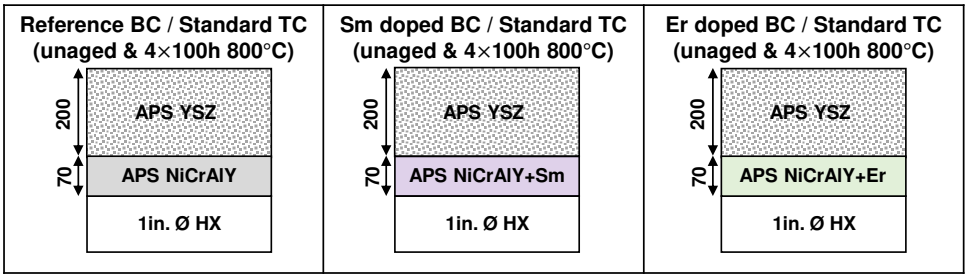

Figure 4.4: Samarium and Erbium doped bond coat samples manufactured at the Florida Institute of Technology using Air Plasma Spray. Thicknesses are indicated in μm.

4.3 Luminescence characterization an Erbium doped bond coat configuration

After manufacturing, the luminescence of the samples was measured using a fiber spectrometer, at room temperature, under a 20 mW 532 nm excitation laser. Two wavelength ranges were selected to characterize the samples. The spectrometer was first centered on the 690 to 700 nm range to verify that the TGO layer formed after aging. It was then centered on 535 to 635 nm range to determine if there is any luminescence emission peak that would be produced by the doping of the TGO for Phosphor Thermometry measurements. The results are presented for one of the samples: the Erbium doped bond coat sample that contains a standard top coat. Figure 4.5 and Figure 4.6 present the luminescence spectra of this sample after aging. It can be noted that, although TGO has clearly formed with a thickness that is sufficient to be detected below a 250 μm top coat, using the typical R-lines, no other usable emission peak could be detected for Phosphor Thermometry up to this point.

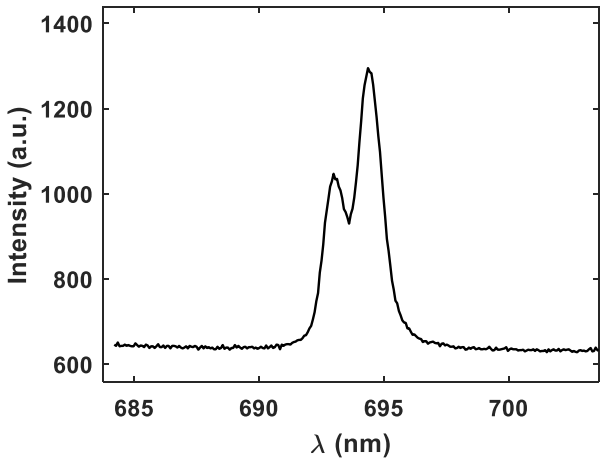

Figure 4.5: R-line emission spectrum from the TGO in the Erbium doped bond coat sample with a standard top coat, after 4×100 h cycles at 800°C, under a 532 nm laser excitation.

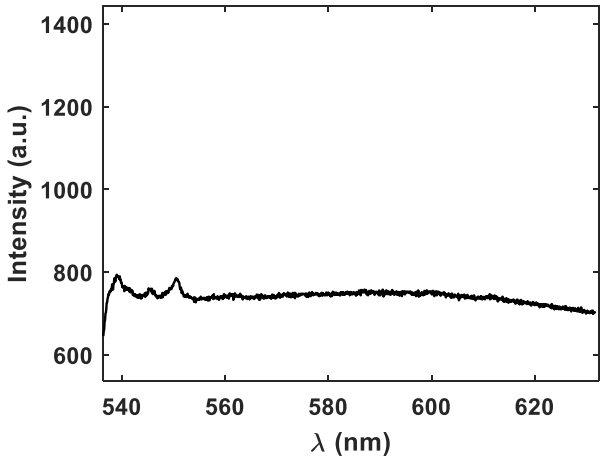

Figure 4.6: Emission spectrum from the Erbium doped bond coat sample with a standard top coat, in the green-orange range, after 4×100 h cycles at 800°C, under a 532 nm laser excitation.

4.4 Elemental mapping of Dysprosium and Erbium doped bond coat configurations

Elemental mapping was conducted on two of the samples that were presented in the sample matrix above (refer to Figure 4.3), namely, the Dysprosium doped bond coat configuration that contains a standard top coat and the Erbium doped bond coat configuration that contains a standard top coat. The investigation was achieved to find the areas where Dy/Er, Zr, Ni and Al are present, after 4×100 h at 800°C. It is important to determine in particular if Al has diffused to the interface between the top coat (highlighted with Zr) and the bond coat (highlighted with Ni). Additionally, it is essential to determine if the rare-earth has migrated or agglomerated in the same area where traces of this element could suffice to form the desired sensing TGO. Elemental maps were taken with an acceleration voltage of 25 kV, which is just high enough to distinguish elements of the substrate (such as Ni) and Dy or Er in the Energy-Dispersive X-Ray spectra. Figure 4.8 shows the SEM and elemental mapping of the Dysprosium doped bond coat configuration. It can be noted that the TGO has formed, as indicated by the agglomeration of Al at the top coat - bond coat interfacial areas. It is very interesting to highlight that Dysprosium contained in the bond coat was found well concentrated areas including or surrounding the TGO. Figure 4.8 shows the SEM and elemental mapping of the Erbium doped bond coat configuration. For this material configuration however, the deposition rate of the doped bond coat pow-

der was found to be insufficient, where almost no bond coat was deposited. This can be due to the unadapted rare-earth powder particle size that resulted in the impossibility to efficiently carry the rare-earth through the APS feeding system.

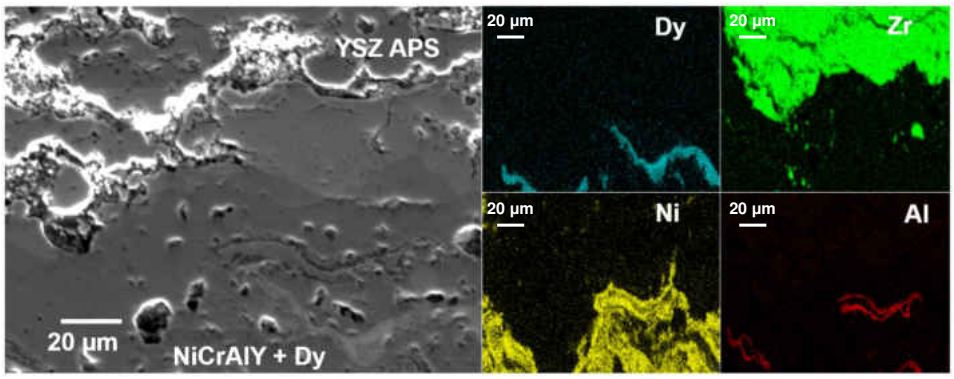

Figure 4.7: SEM and elemental mapping of the Dysprosium doped bond coat configuration with standard top coat.

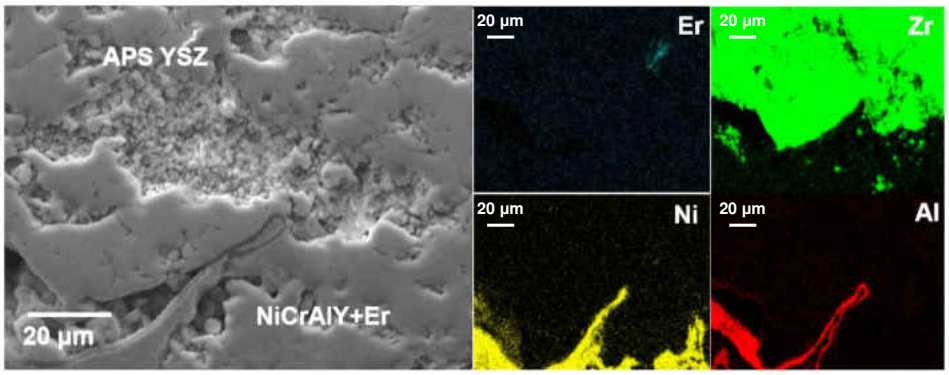

Figure 4.8: SEM and elemental mapping of the Erbium doped bond coat configuration with standard top coat.

CHAPTER 5
PHOSPHOR THERMOMETRY INSTRUMENTATION AND EXPERIMENTATION

5.1 Context of instrumentation development

Thermal Barrier Coatings are widely used in turbine systems to protect the components operating at high temperatures. They are generally used in combination with active cooling systems that allow for temperature drops through the ceramic top coat, in the order of $1^{\circ}C/\mu m$ [204]. Accurate measurement of coating temperatures in such extreme environments is crucial to ensure and maintain good performance, functionality of the system, and predictions on the lifetime of the turbine blades. The temperature measurement uncertainty has to be reduced to a few degrees at service temperatures as failure mechanisms are thermally driven. This is particularly important due to the extreme sensitivity of the growth rate of the Thermally Grown Oxide to the temperature at the interface between top coat and bond coat [67]. Currently, the viable techniques for non-contact *in-situ* temperature measurements are infrared thermometry, for which precision is limited by the presence of

emissions from the operation of the turbine engines as well as emissivity variation, and Phosphor Thermometry, that shows potential as a reliable method for precision temperature measurements [86, 105]. Phosphor Thermometry has proven to be effective at high temperatures using rare-earth or transition metal doped ceramics that can be embedded into TBC configurations to enable real-time temperature monitoring in service conditions [205, 206, 107, 207, 93, 146]. Among the possible sensors for high temperature measurements integrated into TBCs, rare-earth doped Yttria-Stabilized Zirconia (YSZ:RE) have been largely studied as they offer sensing capabilities with ease of integration in existing standard TBCs and no layer compatibility mismatches. Particularly, Europium doped YSZ (YSZ:Eu^{3+}) has been extensively selected as it has excellent temperature sensitivity past its quenching temperature of about 500°C [208] and an intense visible luminescence with a long room temperature decay time [184, 209]. Similarly, Erbium doped YSZ (YSZ:Er^{3+}) has a strong visible luminescence intensity [180]. It has a shorter room temperature decay time and a temperature sensitivity on the entire range between room temperature and turbine operating temperatures [2]. Having a usable absorption band at 532 nm [210] and distinct emission wavelengths, both dopants can be used together in a co-doped configuration that possesses their combined properties. The two dopants have been used together in literature in a YSZ host for multi-layer rainbow sensors [126], thermal history sensors [210, 211], and in Y_2O_3 for intensity ratio measurements [212]. In this work, instru-

mentation was developed so that the luminescence produced by YSZ:Er^{3+} and YSZ:Eu^{3+} could be isolated and simultaneously collected with the objective of doubling the data for higher precision, combining sensitivities of the dopants and extending the temperature range at which the instrument can measure *in-situ* temperature on rare-earth doped YSZ TBCs [213]. The decay and intensity ratio methods were used jointly, as reported in literature [120, 111], to take advantage of the synchronized collection of two dopants. The sample contains the sensing layer at its top surface so the Phosphor Thermometry measurement can be compared with infrared thermometry. Additionally, this configuration allows for the strongest luminescence intensity to emerge out of the sample [113].

5.2 Development of the instrumentation

In this work, a Phosphor Thermometry instrument has been developed to collect simultaneously two emission peaks of a Erbium and Europium co-doped Yttria-Stabilized Zirconia TBC, enabling higher precision of the *in-situ* temperature assessment. The luminescence lifetime decays and the intensity variations of both dopants were captured by the instrument, testing its higher sensitivity and extended temperature range capabilities for accurate measurements, up to operating temperatures for turbine engines. The results open the way for the applicability of portable Phosphor Thermometry instrumentation to

perform effective temperature monitoring on turbine engine materials and support the advancement of innovative sensing coatings.

5.3 Phosphor Thermometry system characteristics

5.3.1 General specifications of the instrument

The Phosphor Thermometry system that is presented in Figure 5.1, has been constructed so it is adaptable to any temperature sensor that has at least two emission peaks that can be isolated by means of dichroic filters. The instrument was also made portable by setting up the system on a stable cart for which the height can be adjusted by either lifting the top surface of the cart or lifting individually the photomultiplier tubes (PMTs) as they are mounted on precision lab lift jacks, fixed on the main optical breadboard. The Phosphor Thermometry instrumentation is equipped with a YAG:Nd pulsed laser (CNI) that provides 10 ns of laser output at a frequency of 10 Hz. The radiation emitted by the laser head is the fundamental mode at 1064 nm with an pulse energy of approximately 2 mJ. Firstly, it travels through a frequency doubling potassium titanyl phosphate (KTP) crystal to generate 532 nm pulses on the order of 0.5 - 1 mJ. Secondly, the 1064 nm and 532 nm beams are collinearly traveling through a lithium triborate (LBO) crystal to gen-

erate pulses at the sum frequency of 355 nm, with pulse energies up to 0.5 mJ. The PMTs are two Hamamatsu R3896 powered by a single precision direct current power supply providing 15 V and a maximum current of 90 mA for each detector. The maximum internal resistance of the gain control module of each PMT was measured to be around 80 kΩ.

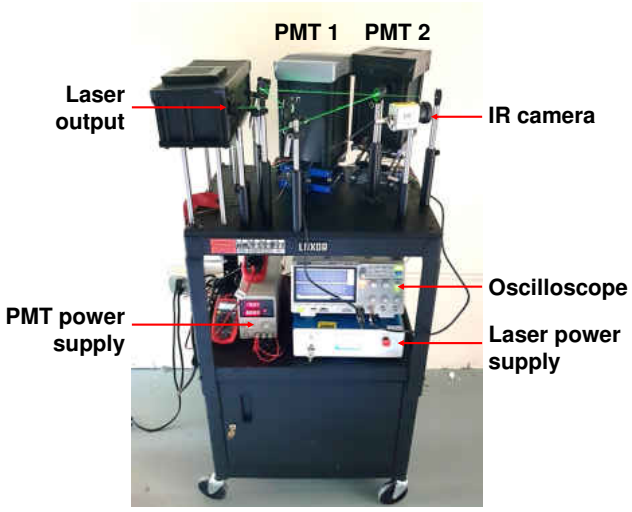

Figure 5.1: Overall view of the Phosphor Thermometry instrumentation.

5.3.2 Testing of the detectors

The instrument was tested using the well-known R-line (ruby) emitted from an alumina block under a 532 nm excitation pulse. This experiment was first achieved at room temperature and using a 694.3 nm bandpass (10 nm FWHM - Thorlabs) for the specific collection of the R1-line decay. A cyan dichroic filter (FD1C - Thorlabs) was used to

transmit the laser beam to the sample and to reflect the luminescence signal to the detector. The resulting decay was fitted using a single-exponential model and is presented in Figure 5.2. The obtained decay is comparable to values found in literature [141, 214].

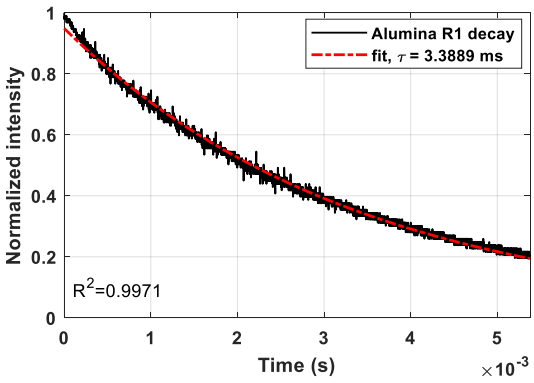

Figure 5.2: Room temperature decay of the R1-line of alumina.

Afterwards, the alumina sample was placed in an infrared heater to capture the sensitivity of its luminescence with temperature. The optical setup used for this data acquisition is presented in Figure 5.3.

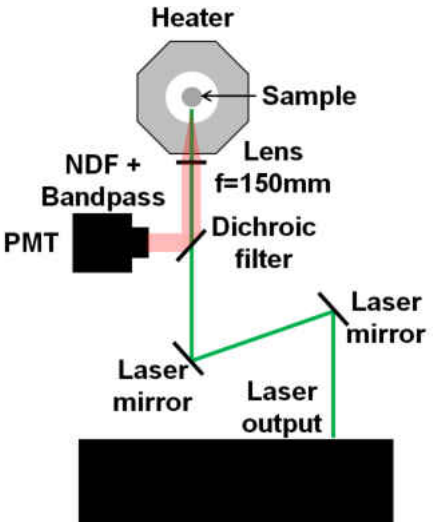

Figure 5.3: Phosphor Thermometry optical setup for initial testing using alumina into a heater.

Lifetime decays were reported in Figure 5.4(a) up to 300°C. At higher temperatures, the luminescence was impossible to collect due to the light that is emitted in the visible range, as a byproduct of the infrared heating. Other options for heating the luminescent samples had be to explored, in order to reduce the background thermal radiation as well as the noise which can impede luminescence measurements, as shown in Figure 5.4(b).

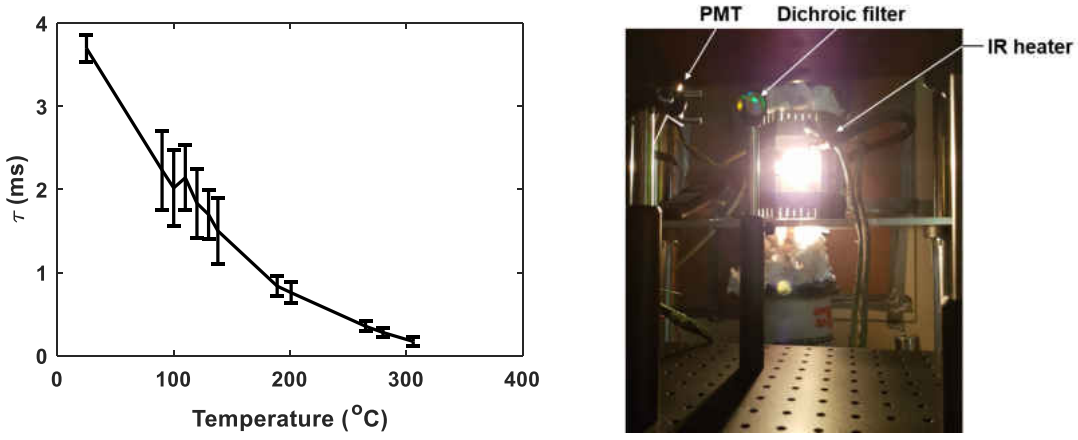

(a) (b)

Figure 5.4: (a) Luminescence lifetime decay of alumina with temperature, and (b) Initial testing using infrared heater for Phosphor Thermometry measuring the luminescence decay of alumina.

5.3.3 Optical setup for YSZ:Er,Eu temperature sensing

For this experiment, the 532 nm excitation was chosen and the 355 nm was stopped with a beam blocker. A couple of laser mirrors were used to adjust the direction of the beam to the sample. After the laser beam was correctly aligned in the axis of the sample, a cyan dichroic filter (FD1C - Thorlabs) was placed in the path of the beam so the angle of incidence (AOI) is 30°. This value was chosen as it lowers the reflection of the laser light on the dichroic filter and allows for a higher excitation intensity onto the sample. A magenta dichroic filter (FD1M - Thorlabs) was then placed with an angle of incidence of

45° from the axis of reflection of the cyan dichroic filter. This allowed the convoluted luminescence of the co-doped sample that was reflected on the cyan dichroic filter to be further split into two spectral bands. The shorter wavelengths containing the Erbium emissions were reflected on the magenta dichroic filter and directed to PMT 1, located in the axis of reflection of the magenta dichroic filter. On the other hand, the longer wavelengths containing the Europium emissions were transmitted through the magenta dichroic filter to PMT 2, located in the axis of reflection of the cyan dichroic filter. The distance from the cyan dichroic filter to the sample was approximately 30 cm and the distance between the two dichroic filters was approximately 8 cm. For the collection of the decays, the two PMTs were used simultaneously. On PMT 1, connected to the channel 1 of the oscilloscope, a 543.5 nm (10 nm FWHM - Thorlabs) bandpass was placed in the viewing port of the detector. Because the wavelengths of the Erbium emission at 545 nm and the excitation at 532 nm are close to each other, some laser leakage occurred due to laser reflections passing though the bandpass which has a transmission and optical density at 532 nm of 0.19% and 2.73, respectively. As the laser intensity is very high in comparison with the luminescence intensity, to better protect the PMT and avoid the undesired collection of laser light, a longpass filter with an optical density of 5 on the 190-532 nm range was added. On PMT 2, connected to the channel 2 of the oscilloscope, a 590 nm (10 nm FWHM - Thorlabs) was mounted in the viewing port. To avoid direct exposition to intense laser

reflections, prevent from the collection of external light, and capture exclusively light traveling through the optical components of the instrument, a laser barrier panel was placed in front of the instrument. A viewing hole was extruded to insert an iris, opened to its maximum aperture (25 mm) and a 125 mm convex lens, that converges the slightly divergent laser beam onto the sample. This arrangement results in a spot size of about 4 mm on the surface of the sample, placed at the focal distance of the convex lens, and allows for the collimation of the luminescence light traveling to the detectors. The optical setup that was assembled for this study is presented in Figure 5.5.

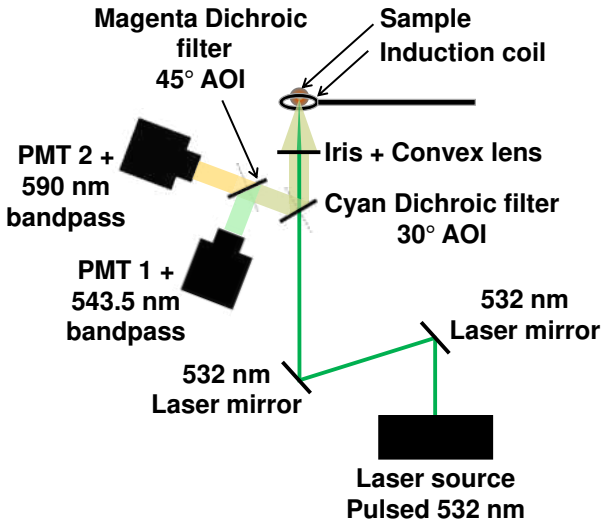

Figure 5.5: Phosphor Thermometry instrumentation for synchronized monitoring of luminescence from YSZ:Er,Eu.

5.3.4 High temperature setup with an induction heating system

For this study, high temperature was achieved via induction heating (RDO HU2000), that produces the high frequency pulsating of magnetic fields to induce internal eddy currents in the material. These eddy currents begin to circulate, causing resistive heating within the material [215]. A frequency of 272 kHz and lift off distance of 5 mm was used between the induction coil and the surface of the sample, as shown in Figure 5.6(a). The resistive heating Q, generated by the internal eddy currents can be described by Equation 5.1:

$$Q = \frac{1}{\sigma} \cdot \mid J_s \mid^2 \tag{5.1}$$

where σ is equal to electrical conductivity and J_s is the eddy current density generated by the magnetic field. In order to keep the sample surface parallel to the induction coil and normal to the horizontal path of the laser beam, a circular segment of the disk was cut off so the sample can stand on refractory blocks, as shown in Figure 5.6(b). Temperature increments of 50°C were achieved up to 1100°C through increasing the power of the inducting system and Phosphor Thermometry data was collected at each temperature step. Induction heating was chosen for this study as it does not produce background thermal radiation which facilitates luminescence measurements.

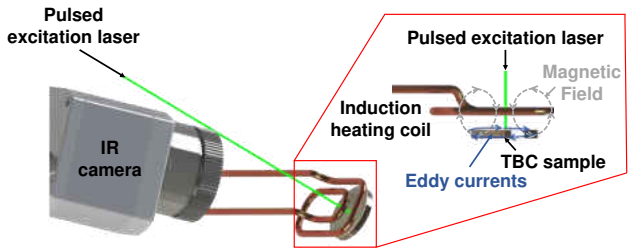

(a)

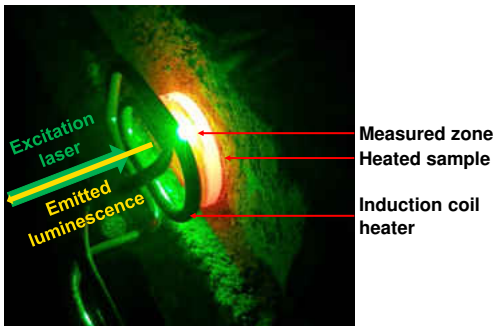

(b)

Figure 5.6: High temperature setup with a) the induction system principle and temperature control using a longwave infrared camera, b) a view of the heated sample with the Phosphor Thermometry measurement.

5.3.5 Control of the temperature using infrared thermometry

The temperature was measured using a TIM450 (Micro-Epsilon) longwave infrared camera (7-13 μm) operating at 30 Hz and placed at 20 cm from the sample, which corresponds to the focal distance of the camera. The collection area was reduced to match the Phosphor Thermometry laser spot size. The camera uses the program TIM Connect to

track the thermal radiation emitted from the sample. The emissivity was set to $\varepsilon = 0.95$ for all readings as this value corresponds to the emissivity of YSZ in the longwave infrared range and does not vary noticeably with temperature [216, 217, 218].

5.3.6 Data collection

5.3.6.1 Spectral characterization of the sample

The emission spectrum of the YSZ:Er,Eu sample has been measured with a collection time of 1 ms using a fiber collection spectrometer (Pixis 100, Princeton Instruments) under a 15 mW 532 nm laser excitation. The probe has a focal length of 7.5 mm, a depth of field of 2.2 mm, a numerical aperture of 0.27, and a spot size of 200 μm. The Er-lines at 545 nm and 562 nm and the Eu-lines at 590 nm and 606 nm were observed. The co-doping might introduce some level of re-absorption of the Erbium-lines due to the presence of Europium that possesses an absorption band that excites the $^5D_1$ level and that extends from 520 to 550 nm [184, 141]. This could ultimately result in a smaller intensity ratio between Erbium and Europium. For this study, the peak of Erbium at 545 nm ($^4S_{3/2} \rightarrow {}^4I_{15/2}$) and the peak of Europium at 590 nm ($^5D_0 \rightarrow {}^7F_1$) were chosen for luminescence intensity and

decay measurements. Figure 5.7 shows the emission spectrum of the YSZ:Er,Eu sample, highlighting the two regions that were collected by the Phosphor Thermometry detectors.

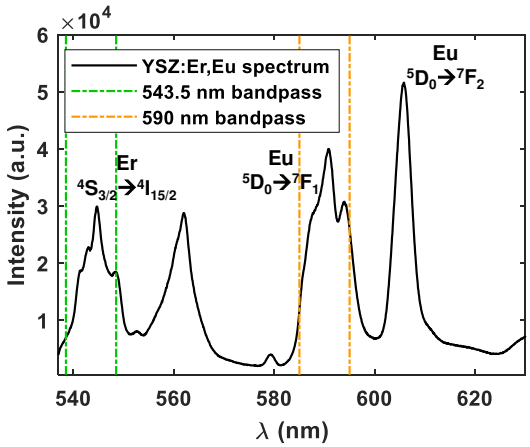

Figure 5.7: Emission spectrum of YSZ:Er,Eu under 532 nm laser excitation. The full width at half maximum of the bandpasses is represented to indicate the range of wavelength collected for the luminescence measurements.

5.3.6.2 Acquisition of luminescence decays

The luminescence decays of the Erbium emission at 545 nm and the Europium emission at 590 nm were captured simultaneously, using PMT 1 and PMT 2, respectively. A Siglent SDS 1204X-E oscilloscope was used to convert the electric signal to data matrices. In front of the viewing port of PMT 1, the incoming light is composed of a spectral band which ranges in wavelength between 532 nm and 560 nm. It contains the lumi-

nescence emitted by Erbium as well as some laser reflections. This light followed the optical path originating at the sample surface, reflected on the cyan dichroic filter with $R_{cyan,545nm} \approx 95\%$ and reflected on the magenta dichroic filter with $R_{magenta,545nm} \approx 92\%$. The spectral band was narrowed down to select the peak of Erbium at 545 nm, using both a 543.5 nm bandpass and a laser cutoff longpass, as described in the optical setup section. Similarly, in front of PMT 2, the incoming signal contains a spectral band with a wavelength range between 560 nm and 720 nm. It contains the Europium luminescence that emerges out of the sample surface and is reflected on the cyan dichroic filter with $R_{cyan,590nm} \approx 100\%$ and transmitted through the magenta dichroic filter with $T_{magenta,590nm} \approx 91\%$. The specific luminescence emission peak of Europium at 590 nm was selected by placing the 590 nm bandpass described in the optical setup section in the viewing port of PMT 2. To obtain a greater amplitude of the signal that facilitates the detection of the luminescence decay and increases the signal-to-noise ratio (SNR), fixed resistance loads were connected to the RG58 coaxial cables that link the PMT detectors to the oscilloscope. Resistances of 50 kΩ and 5 kΩ were applied to the acquisition channels associated with PMT 1 for Erbium and PMT 2 for Europium, respectively. Figure 5.8 shows an example of the simultaneous decay acquisition, captured at 500°C and showing the long decay of Europium ($\approx 632\ \mu$s) compared to the one of Erbium ($\approx 13\ \mu$s) as well as the higher noise of the Europium decay due to the lower resistance value chosen for

the acquisition. For this experiment, the amplitude of the signal was favored over time response to enable the use of luminescence intensities up to high temperature. By selecting these high feedthrough resistances, the minimum lifetime decay that could be accurately measured was found to be ≈ 6 μs for channel 1 and ≈ 1.5 μs for channel 2. After the completion of the experiment, the collected data was processed using a MATLAB code that synchronizes all decays so that $t = 0$ corresponds to the start of the decay at all temperatures, as presented in Figure 5.9. The code uses a single exponential model to fit the data of both decays. Even though the Europium decay has been shown to have a triple-exponential decay behavior [123], the single exponential model has been widely used as it offers a more robust fit for the temperature measurement using this phosphor [141, 1, 142].

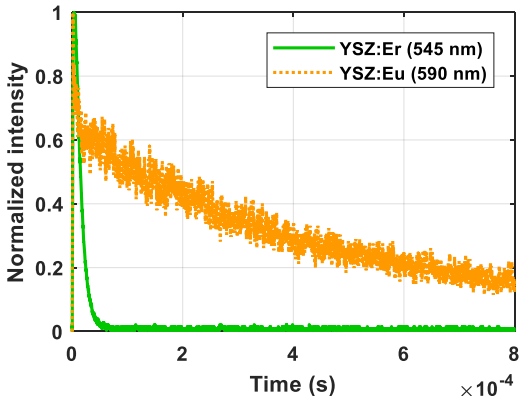

Figure 5.8: Synchronized collection of Erbium and Europium decays at 500°C.

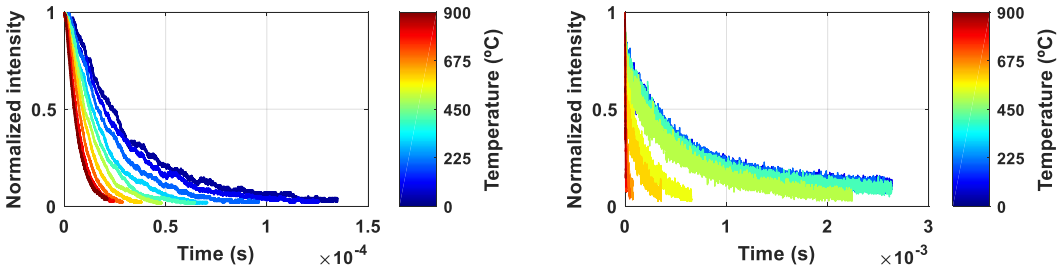

(a) Er emission at 545 nm (b) Eu emission at 590 nm

Figure 5.9: Behavior of the luminescence decays of (a) Erbium and (b) Europium with respect to temperature.

5.3.6.3 Measurement of luminescence intensities

The use of two independent PMTs and high signal-to-noise ratio allows for the comparison of the intensities at $t = 0$, when the laser excitation pulse ends and where the luminescence intensity reaching the detectors is maximal. The PMTs receive a reduced region of the spectrum that is let through by the bandpasses and convert all the reaching photons to an electrical amplitude, measured in volts. The quantum efficiency of the PMTs is expected to be slightly higher at 545 nm ($\approx 20\%$) than at 590 nm ($\approx 18\%$). For this experiment, the feedthrough resistance of channel 1, that collects the luminescence of Erbium, was set to a higher value than the one of channel 2, as it allowed to get amplitudes exceeding 1 V for both dopants. At room temperature, the integrated intensity of the luminescence of Europium between 585 nm and 595 nm was found to be about 55%

higher than the one of Erbium between 538.5 nm and 548.5 nm (in the spectral ranges of the bandpasses). This is mainly due to the particular quantum yield of Erbium and Europium in YSZ, with the specific concentration and distribution parameters that were obtained for this sample. All the collected intensities were processed by the MATLAB routine to subtract the growing thermal radiation background from the measurements by averaging the intensity received by the PMTs when laser excitation is off and no luminescence remains. This takes place typically just before a new excitation pulse, which corresponds on the oscilloscope window to the trace preceding the rise-time and decay. The ratio between the normalized intensities of the two dopants can be used for high temperature measurements, assuming that the spectral shift due to temperature is negligible in comparison with the spectral bandpass of the filters used for the collection of light [219]. The integrated intensity measured by each of the two PMTs is, in consequence, assumed to remain proportional to the peak intensity of each radiative transition.

5.4 Results and discussions

5.4.1 Temporal analysis

The independent luminescence decays were fitted at each 50°C step and the results were reported in Figure 5.10. The error bars represent the standard deviation of three independent measurements that were performed with an identical setup, on three different locations onto the sample. It can be seen that the decay of Erbium at 545 nm is sensitive to temperature over the entire range of temperature from room temperature to 850°C with a lifetime decay time at room temperature of approximately 31 μs. The decay of Europium has a very high sensitivity in the range of temperature comprised in between the quenching temperature of the phosphor in YSZ ($\approx$ 500°C) and 850°C, with a lifetime decay time of approximately 1.2 ms at room temperature. The advantage of the co-doped configuration and simultaneous data acquisition of the decays is the extension of the temperature range on which the decay method is applicable as the individual dopant have different maximum sensitivity temperature ranges. Past 850°C, the fits of the Europium decay indicate a lifetime that stagnates around 1.5 μs which corresponds to the detection limit of the instrument on this channel, which is related to the resistance used for collection of the signal, as described in the data acquisition section. This temperature also matches with the limit found in literature for YSZ:Eu^{3+} [142, 144]. This inaccurate lifetime decay is gen-

erated by the limited response of the instrument at high temperature [220]. Reducing the resistance feedthrough on the channel can reduce the response time to some extent, but it implies a significant degradation of the SNR. A compromise between signal-to-noise ratio and time-resolution has to be selected for high temperature Phosphor Thermometry. The sensitivity of the decay of Europium appears to be very high between 500°C and 850°C which corresponds to the luminescence quenching of the dopant into YSZ, due to the higher probability of vibrational deexcitation past the quenching temperature. However, the sensitivity of the decay of Europium outside this highly sensitive temperature range is close to zero. The combination of Europium with Erbium, facilitated by the instrument, allows for the extension of the range of temperature that can be measured using the decay method. This is because the lifetime decay of Erbium can be conveniently differentiated for any temperature between room temperature and turbine system operating temperatures.

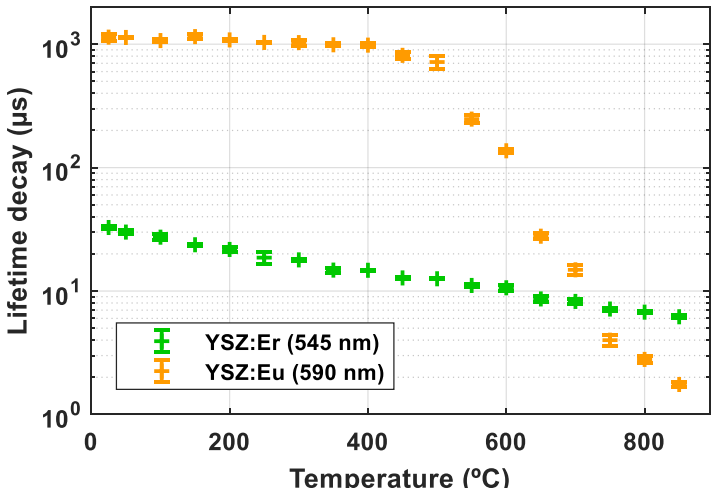

Figure 5.10: Lifetime decay response of APS co-doped YSZ:Er,Eu.

5.4.2 Intensity considerations

The luminescence intensity variation was measured and the ratio between the intensities of the Erbium emission at 545 nm and the Europium emission at 590 nm, normalized with respect to their distinct room temperature intensity. This data was obtained to provide additional information for the temperature measurement using the Phosphor Thermometry instrumentation. The luminescence intensity was obtained by measuring the maximum of the amplitude of the luminescence decay, that is proportional to the amount of photons reaching each PMT at the moment where the laser excitation pulse produces the strongest luminescence. As the temperature increases, it was found that the luminescence in-

tensity of both dopants initially increased, due to the thermal filling of the energy levels, then decreased due to thermal quenching. The growing thermal radiation, which spectral radiance can be predicted using Planck's law, provides a contribution to the overall intensity of which one part is the luminescence. The percent variation of the luminescence intensity for each dopant, with respect to the room temperature intensity is reported in Figure 5.11. The error bars indicate the standard deviation of three independent measurements that were performed with an identical setup, on three different locations onto the sample. It was also found that the ratio of the normalized intensity variation of Erbium to Europium, $R_{Er/Eu}$, has a sensitive range of temperature, usable from 850°C up to at least 1100°C, as presented in the lower plot. The error bars report the propagation of error from the ratio of the intensity variation between Erbium and Europium. This is a result of the fast quenching of Europium luminescence on this range compared to the luminescence of Erbium, that remains strong, as shown in the 3D plots. Although the lifetime decay of Europium cannot be accurately determined past 850°C due to the limitation on the temporal resolution of the instrument, the high SNR allows for valid intensity measurements at higher temperatures.

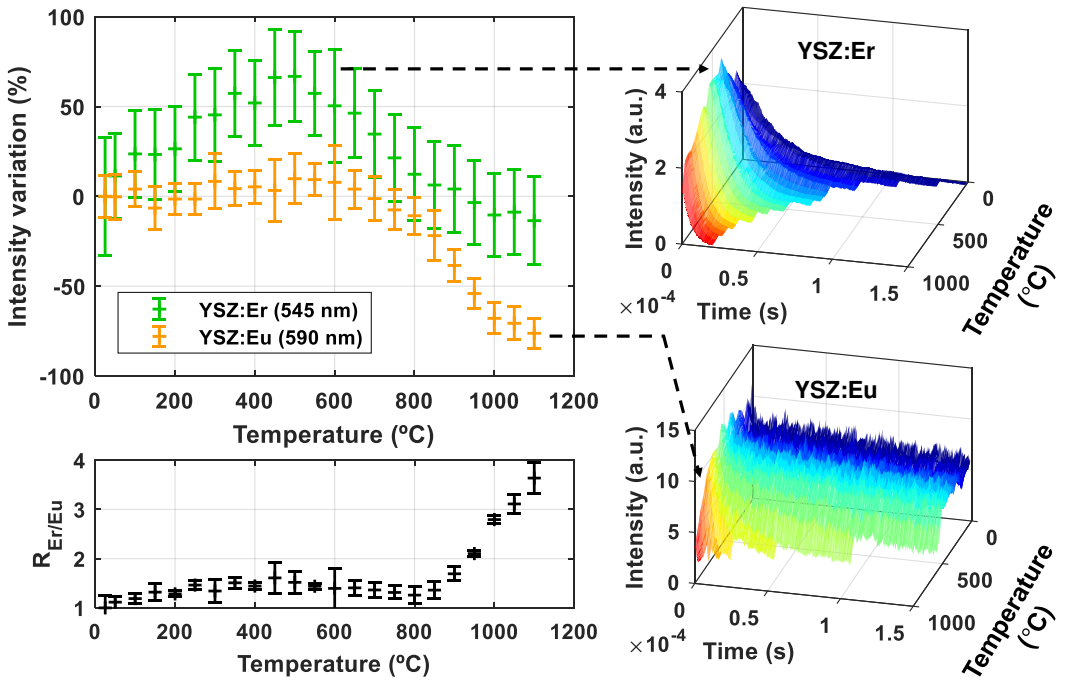

Figure 5.11: Percent luminescence intensity variation with respect to room temperature intensity for each dopant and corresponding ratio, sensitive between 850°C and 1100°C and usable for high temperature measurements.

5.4.3 Measurement error considerations

To evaluate the precision and obtain a representative response of the instrument with the YSZ:Er,Eu sample, three independent measurements were performed. The Phosphor Thermometry instrumentation setup remained unchanged while the sample and the induction coil were translated normally to the laser to collect the luminescence signal from three different locations. It is important to consider the intrinsic temperature measurement un-

certainty implied by the utilization of infrared thermometry, which accuracy is $\pm$ 2% at high temperature. Indeed, the material was brought to the desired temperature values for data collection using infrared thermometry as the reference to determine the power input of induction heating. Another limiting factor when targeting a temperature for measurement is due to the gradient of temperature in the doped layer, created by the heat flux from the top surface to the bond coat in TBCs, but which direction is inverted in this study due to the utilization of the induction coil that heats preferentially the metallic substrate and dissipates heat by convection at the free surfaces of the material. Furthermore, material characteristics can vary importantly with position probed on the sample. For example, the random distribution of porosity affecting both thermal and optical properties of the material and the irregularity of the doped layer thickness contribute in possible variations in the luminescence of the sample. A possible uneven distribution of dopant into the material, possibly intensifying ion-ion interaction, or the consecutive thermal cycling can also result in intensity and lifetime decay variation when probing different locations onto the doped layer. Uncertainty on the exponential fit can also be significant, in particular with Europium, that exhibits a triple-exponential decay behavior typically. The precision of the measurements at 800°C was found to be $\pm$ 8°C and $\pm$ 3°C, using Erbium and Europium decays, respectively. In addition, it can be noted that the current instrumentation is a lab-scale prototype that would necessitate automated acquisition for calibration to reduce

experimental errors and that would require further development to allow for measurements on an operating engine, using an optical port, similarly to other existing instrumentation [137].

5.4.4 Outcomes of the developed instrumentation for YSZ:Er,Eu TBC sensing

A Phosphor Thermometry instrument has been developed for the synchronized data collection of the luminescence decay and intensity ratio measured from two independent emission peaks coming from an Erbium-Europium co-doped Yttria-Stabilized Zirconia Air Plasma Spray Thermal Barrier Coating. The luminescence emerging out of the doped layer was collected up to 1100°C with 50°C steps, while the surface temperature was concurrently measured using a longwave infrared camera. The high resistances at the input of the oscilloscope, chosen to amplify the signal-to-noise ratio, allowed to collect lifetime decays with a sufficient bandwidth up to 850°C. The results were found to be in good accordance with literature. At higher temperatures, the limited response time was compensated by the acquisition of the ratio of intensity between Erbium and Europium emission peaks, that varies significantly due to the faster quenching of Europium. As a consequence, the range of temperature that can be accurately measured using rare-earth doped YSZ configurations was extended up to turbine engine operating temperatures. The simultaneous ac-

quisition of Phosphor Thermometry data achieved in this work paves the way for increased precision measurements on extended temperature ranges using the high-sensitivity decay method combined with the high-detectability intensity ratio method. Exploiting further the synchronized acquisition capabilities of this novel Phosphor Thermometry instrumentation will provide efficient *in-situ* temperature measurement options for turbine components.

5.4.5 Initial effort for model-validation through high heat-flux experimentation

In the attempt of validating the claims and results previously presented, in the chapter on luminescence modeling, an additional heating setup was tested. This was done in order to replicate thermal gradients that are existing in turbine environments. The advanced Phosphor Thermometry instrumentation that has been developed in this work has been used with the same optical configuration, using only PMT 1, and substituting the 543.5 nm bandpass by a 560 nm bandpass (10 nm FWHM - Thorlabs) to collect the emission peak at 562 nm from a YSZ:Er sensing TBC, which luminescence spectrum and microstructure are shown in Figure 5.12(a) and Figure 5.12(b), respectively.

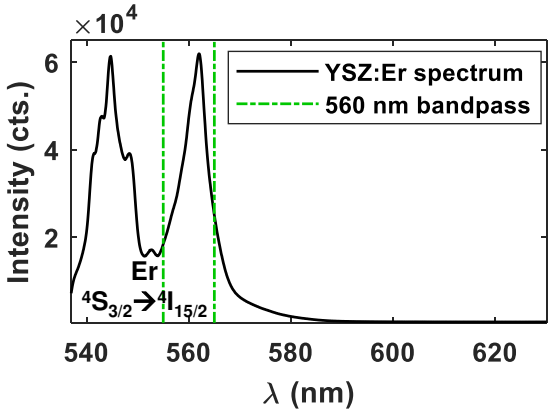

(a)

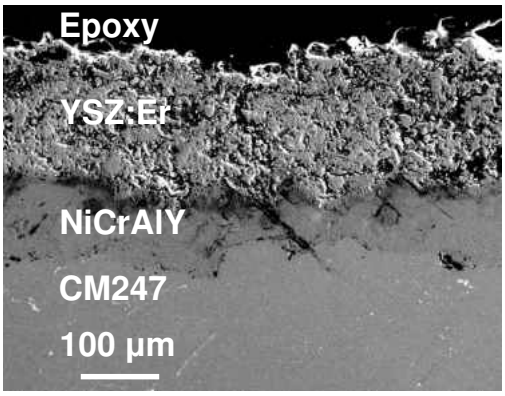

(b)

Figure 5.12: (a) Luminescence spectrum of YSZ:Er, highlighting the range of wavelengths captured for decay measurements, and (b) Micrograph of the YSZ:Er TBC.

To achieve a realistic thermal gradient, a high-heat flux burner rig was constructed for *in-situ* sub-surface temperature measurement on a 200 μm YSZ:Er TBC sample. The burner rig experimental setup includes an infrared camera and a K-type thermocouple, for the measurement of the surface and the back of the coupon, respectively. The burner rig

supplies a 560 kW heat flux that is usable to apply thermal gradient while performing Phosphor Thermometry measurements, taken at intervals of 100°C, on the TBC surface, up to 900°C. Figure 5.13 displays the *in-situ* Phosphor Thermometry experiment during the high-heat flux testing.

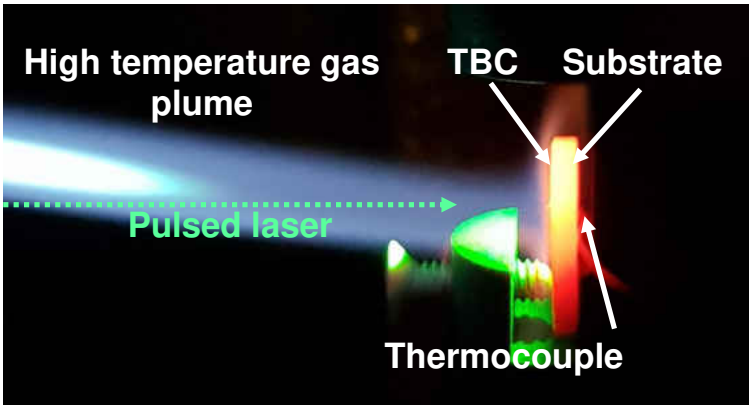

Figure 5.13: High-heat flux experimental setup to induce a thermal gradient through the thickness of the TBC.

As described in the modeling sections, the presence of the temperature gradient is expected to generate a convoluted luminescence signal emitted from different depths within the TBC. As the result, the Phosphor Thermometry detector captures a temperature measurement at a sub-surface location. Applying the YSZ:Er sample configuration to the previously described models predicts the location of the temperature measurement to be at 38 μm from the top surface. It can be noted that the precision of this modeled location is limited due to the difficulty for the estimation of the actual quantum efficiency

of the phosphor, due to the very strong scattering of the ceramic TBC, and caused by the inhomogeneities in the top coat material. Furthermore, the accuracy of the Phosphor Thermometry measurements is determined by the quality of the reference measurement, which needs to be achieved to get the appropriate calibration of the instrument with the specific sample. In this experiment, the reference measurement, where ideally no thermal gradient is applied to the TBC top coat was performed by heating the coupon up to a surface temperature exceeding 900°C, and stopping the heat flux to release the sample which creates a balancing of the temperature in the top coat. It was assumed that the temperature into the top coat was homogeneous as the sample cools down, which allowed to perform Phosphor Thermometry measurements from 900°C to room temperature, using infrared thermometry as the TBC temperature reference. The luminescence decays that were collected are presented in Figure 5.14. The luminescence of YSZ:Er presents the advantage of having a single-exponential behavior and a good temperature sensitivity over the entire temperature range for this study.

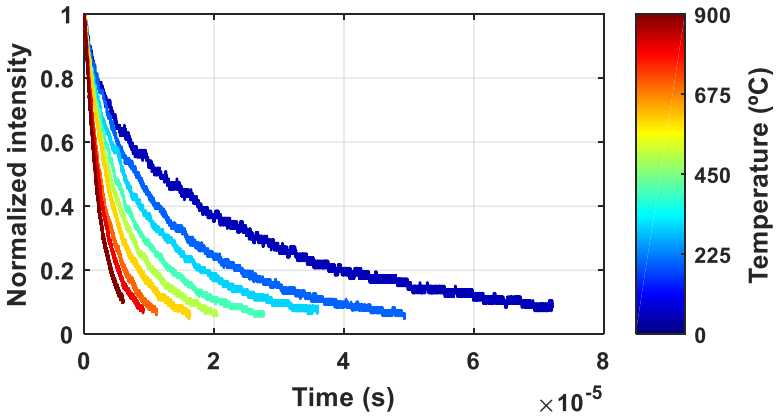

Figure 5.14: Luminescence decays of YSZ:Er measured from room temperature to 900°C.

The feasibility of sub-surface temperature measurements using Phosphor Thermometry was proven by observing the shifting of lifetime decays, when applying a thermal gradient to the TBC, as shown in Figure 5.15. During the high-heat flux experiment, for a surface temperature of 600°C, the thermal gradient in the top coat was estimated to be of the order of 160°C, using the temperature measurement provided by the thermocouple located at the back of the sample, and using a 1D conduction model. The Phosphor Thermometry instrument calibration indicates with the black dashed line (refer to Figure 5.15) that the decay constant corresponding to YSZ:Er exposed to 600°C with no thermal gradient equals approximately to 4.62 μs. Similarly, the lifetime decay constant corresponding to the case where the surface temperature is 600°C, and where a 160°C gradient is applied,

equals approximately to 5.33 μs, which gives a sub-surface temperature of 565°C, based on the decay constant that matches the response found during calibration.

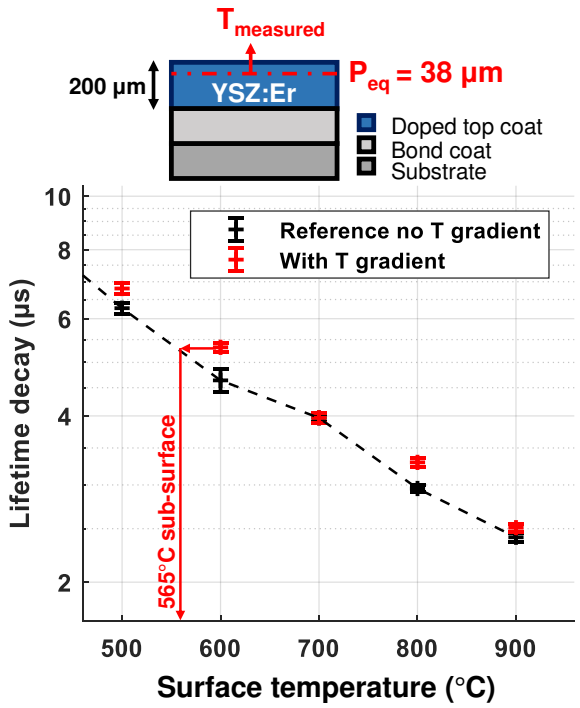

Figure 5.15: Sub-surface temperature measurements, in presence of a thermal gradient enabled by Phosphor Thermometry.

The position at which the temperature measurement is made can be theoretically estimated using models and associated with this experimental temperature value, which allows to reveal the gradient of temperature that is acting through the TBC. In this particular case, a surface temperature of 600°C was measured by the infrared camera and Phosphor Thermometry provided the temperature value into the depth of the coating, which was found to be 565°C at 38 μm from the top surface. The resulting gradient of temperature

is about $1^{\circ}C/\mu m$. As a conclusion, this study shows huge potential for improved measurement capabilities using Phosphor Thermometry, applied to turbine environments, and using thick luminescent coatings. Additionally, luminescence models can be associated to experimental results to help unveiling temperature gradients in TBCs.

CHAPTER 6
EVALUATION OF RARE-EARTH DOPED TBC CONFIGURATIONS USING SYNCHROTRON RADIATION

With a growing demand for more sustainable and efficient turbine systems, extending coatings' capabilities is imperative. Due to their extreme operating conditions, significant effort has been invested in understanding the thermomechanical behavior of TBCs under operational environments [188, 221, 222, 223, 224]. For the sensing coatings presented in the previous chapters, characterizing the mechanical properties of the doped material configurations is essential to determine the ability of these coatings to retain or further enhance TBC performance. In this work, the coatings were tested in room and high temperature environments, using in-situ synchrotron X-ray diffraction (XRD).

6.1 Synchrotron X-Ray Diffraction theory

Synchrotron sources produce high-energy X-rays that are ideal for high-resolution strain measurements using transmission XRD. The Sector 1 beamline at the Advanced

Photon Source of Argonne National Laboratory produces extremely bright X-rays, which energy can be as high as 150 keV. The general method of strain determination using synchrotron XRD is described in literature [225], and summarized in this chapter.

As the X-rays impinge the sample, the interplanar spacing (d-spacing) is determined using Bragg's law. The distortion of the diffraction pattern rings provides information on the averaged strain in the volume probed of the material, in directions normal to the X-ray beam. The diameter of the ring is related to the d-spacing, using simple trigonometry of the diffraction set up, as given in Equation 6.1, and Bragg's law can be therefore reformulated as given in Equation 6.2.

$$\theta = \frac{1}{2}\arctan\left(\frac{D}{2L}\right) \tag{6.1}$$

where θ is the angle between the incident ray and the scattering planes, D is the diameter of the diffraction ring, and L is the sample to detector distance.

$$d = \frac{\lambda}{2\sin\left(\frac{1}{2}\arctan\left(\frac{D}{2L}\right)\right)} \tag{6.2}$$

where λ is the wavelength of the X-ray.

Equation 6.2 can be simplified for small Bragg angles (high-energy X-rays), providing Equation 6.3.

$$d \approx \frac{\lambda L}{D} \tag{6.3}$$

Hence, the strain for a lattice plane (the reference or unstressed state denoted with subscript 0) is expressed in terms of the diffraction ring diameter as given in Equation 6.4. This corresponds to the widely used equation in strain determination using X-ray diffraction with a 2D area detector.

$$\varepsilon = \frac{d - d_0}{d_0} \approx \frac{D_0 - D}{D_0} \tag{6.4}$$

6.2 Transmission X-ray diffraction for TBCs

High-energy XRD measurements allow for the investigation of the thermomechanical behavior of coating materials at the micron level. Specifically, high-resolution measurements allow for the characterization of the spatial distribution of residual strains in TBCs [200]. Residual strains are strongly dependent on the microstructure formed during processing and operation [226, 227]. Controlling the residual strain of doped TBCs will enable the evaluation of the mechanical properties and to anticipate possible failure [188, 223, 228]. The thermomechanical and thermochemical stability of the coating must be maintained under extreme operating conditions. The purpose of this work is to ensure

that the doped materials that are made for Phosphor Thermometry still meet the standards for TBCs so they can be applied to operating turbine systems with reduced risk of lifetime reduction.

6.3 XRD experiment setup and parameters

6.3.1 Experiment parameters

Table 6.1 reports the parameters that were chosen for the synchrotron experiments, selected with the intention of using peak (101) of the metastable tetragonal phase of YSZ, as it is known to exhibit the highest diffraction intensity, for strain measurements. The XRD beam size was focused using lenses to allow for high spatial resolution and fast acquisition.

Table 6.1: Synchrotron XRD parameters used for TBC characterization.

Parameter	**Value**
Beam energy	71 keV
Sample to detector distance	1.78 m
Beam size	$15{\cdot}150\ \mu m^2$
Step size	$15\ \mu m$
Volume probed	$5.6{\cdot}10^{-3}\ mm^3$
Exposure time	0.3 s
Main diffraction angle t'-(101) peak	3.36°

6.3.2 Sample description

The measurements were done on three samples that were taken from the previously described list of manufactured APS YSZ materials. A reference TBC including a 260 μm YSZ top coat, a sensor TBC including a 180 μm YSZ:Er top coat and a sensor TBC including a top coat constituted of a 250 μm undoped YSZ bottom layer and an 80 μm YSZ:Er,Eu co-doped top layer. It is important to note that, before residual strain evaluation, the as-deposited APS materials received a heat treatment of 2 h at 800°C for luminescence enhancement. As reported in the chapter that describes the manufacturing process, samples used for XRD experiments are 2.5 mm width rectangular cuboid pieces, so the volume probed by the incident X-ray beam remains constant for all samples. This small width was chosen to avoid broadening of the diffraction rings. The thickness of the sample is about 3.5 mm, TBC included.

6.3.3 Sample setup

The high-energy synchrotron XRD measurements were performed at beamline 1-ID of the Advanced Photon Source at Argonne National Laboratory. High-energy X-rays and micron-scale beam size provided the ability to probe the three TBC configurations into

the depth of the coatings. The XRD data was collected with a spatial resolution of 15 μm along the thickness of the coating, and 3 line scans were taken by moving the stage with a 1 mm step along the surface (y-direction), as shown in Figure 6.1, to get statistical residual strain results with respect to the sub-surface location into the coating.

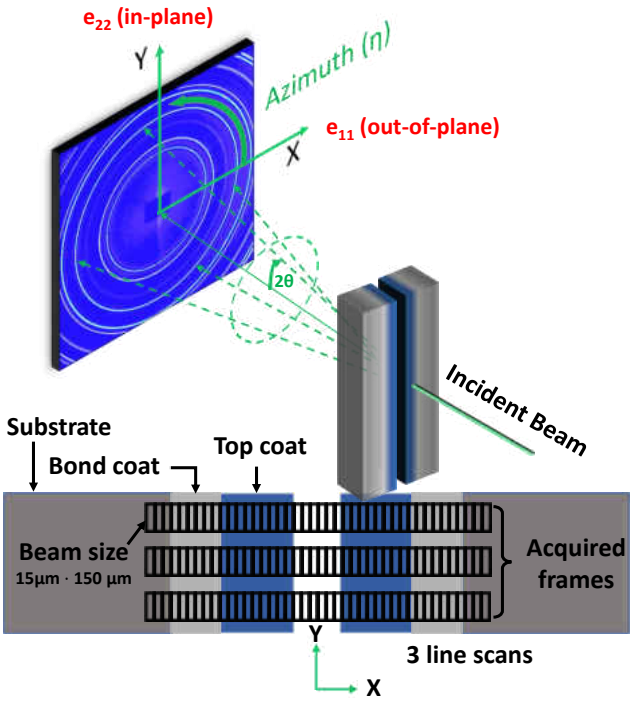

Figure 6.1: Schematic view of data collection using transmision XRD. Diffraction pattern was obtained experimentally for YSZ.

The sample tilt, that is amplified at the micron-scale, was corrected by finding, for each line scan, the frame corresponding to the top surface for each sample, using diffraction peak intensities. The frames from all three lines were then correlated to discrete

positions along the x-axis, and the comparison between lines was achieved by matching the positions.

6.3.4 Replication of high temperature engine environments

In order to replicate thermal loads that usually exist in engine environments, a high temperature setup was designed to operate at the beamline, in combination with the transmission XRD setup. For this purpose, a 30 A infrared heater that possesses lateral measurement holes, for the incoming and diffracted XRD beam, was mounted on a fixed arm so the ports are aligned with the XRD beam. High-energy transmission *in-situ* XRD data was collected on the samples from room temperature and ramping up with a rate of 100°C/min with 6 min holds at 400, 600, 800, 900, 1000 and 1100°C, as indicated in Figure 6.2. Data acquisition was initiated after 1 min holding at the desired temperature. This duration was assumed to be sufficient to avoid the presence of a thermal gradient into the top coat.

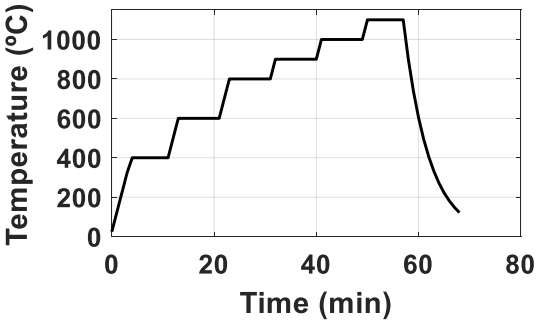

Figure 6.2: Thermal cycle used for transmission XRD measurements.

For each high temperature experiment, two samples were mounted face-to-face in an Alloy X sample holder, as presented in the inset of Figure 6.3, allowing for reduced experiment time.

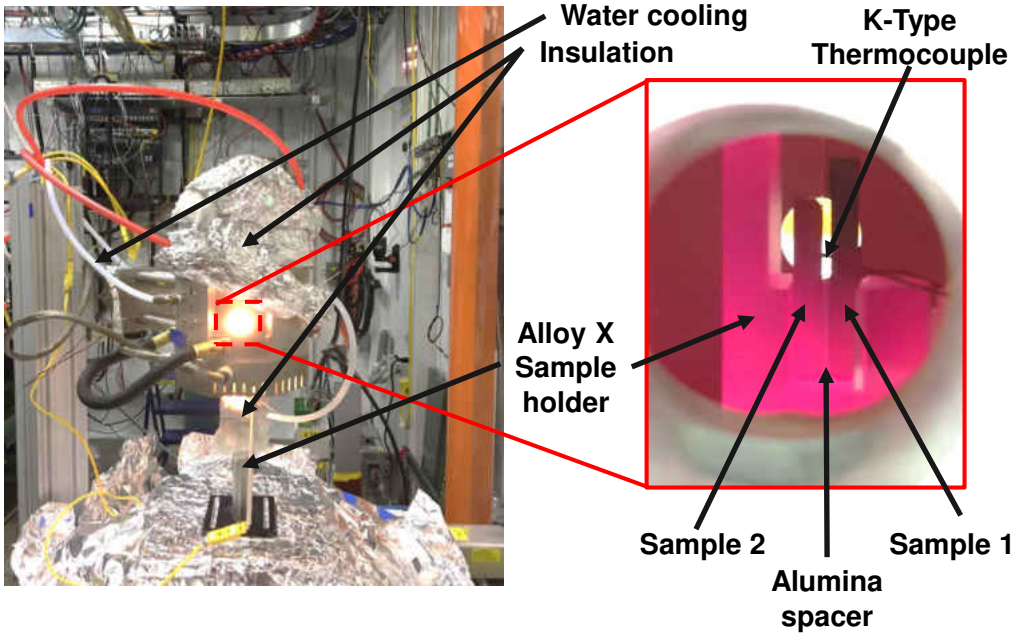

Figure 6.3: High temperature setup used for transmission XRD measurements.

In this experiment, the XRD beam is fixed, and the sample is translated via the movement of the stage on which the sample holder is attached. Alumina-silica fiber insulation was used to prevent from too large heat dissipation in the chamber, and the fiber was surrounded with aluminum foil. Room temperature water cooling with a pressure drop of 60 - 70 PSI was used to cool the heater components and was assisted with air cooling, directed to the infrared lamps. K-type thermocouples (Ni-Cr + Ni-Al leads) are known to be applicable for temperature measurements up to 1372°C. Therefore, one K-type thermocouple was placed in the chamber, in contact with the TBC surface, to monitor temperature as

close as possible to the zone that is measured by XRD. Additional thermocouples were installed outside the heater to check on the efficiency of the cooling and ensure safety of the components from potential overheating. During experimentation, thermal expansion of the sample holder and of the samples result in a significant displacement of the samples. To maintain the samples in place for measurements, a 1 mm thickness alumina spacer was used to provide a flat area to the sample which increased considerably sample stability and helped for the positioning, reducing the tilt.

6.4 *In-situ* residual strain analysis

6.4.1 Initial sample characterization

Diffraction lineouts were observed to be similar for the three samples of this study, indicating that there is no difference in terms of the phases in presence in the coatings. It can be recalled that the concentration of doping ions, also acting as stabilizing ions, is relatively small (1 - 3 wt.%), which does not destabilize the metastable tetragonal phase t', that is generally found in YSZ TBCs. Figure 6.4 shows the standard diffraction pattern, obtained with the reference YSZ sample, where the t'-YSZ lattice planes were identified,

using the relation between Miller indices (*hkl*) and lattice parameters, as given in Equation 6.5.

$$\frac{1}{d^2} = \frac{h^2 + k^2}{a^2} + \frac{l^2}{c^2} \tag{6.5}$$

where $a = 3.61\ \mathring{A}$ and $c = 5.16\ \mathring{A}$, were taken from literature [72, 229, 230].

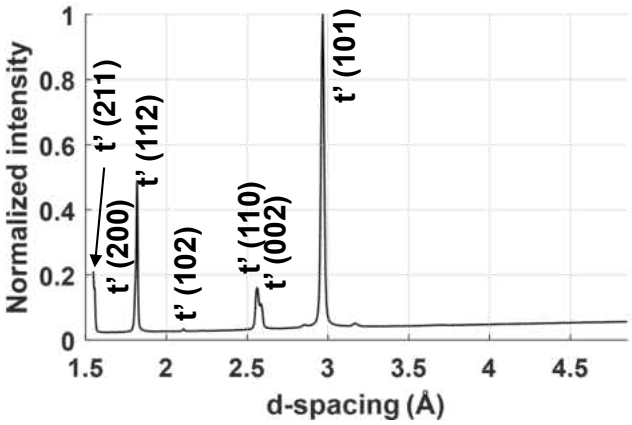

Figure 6.4: Air Plasma Spray YSZ TBC diffraction lineout.

6.4.2 Residual strain methodology

To correct tilt angles of the detector and find the precise sample to detector distance, a ceria powder was used for calibration and the correcting parameters were obtained using

Fit2D [231, 232]. The ceria powder was placed at the precise location where TBC samples are held for XRD measurements, then removed after calibration and prior to *in-situ* sample characterization. The elastic constants of YSZ were taken from literature [233]. The η^* method was used for the determination of residual strain as it allows to get a zero-deviatoric strain reference [234]. The η^* angle was calculated using Equation 6.6, and the Kröner model was chosen to obtain specific lattice plane dependent Poisson's ratios, using DECcalc [235].

$$sin^2(\eta^*) = \frac{2 \cdot \nu_{hkl}}{1 + \nu_{hkl}} \tag{6.6}$$

where ν_{hkl} is the modeled Poisson's ratio in the lattice plane (*hkl*). Numerical values taken for strain calculation using the η^* method are given in Table 6.2.

Table 6.2: Zero strain reference diffraction angles based on the η^* method.

Lattice planes of t'-YSZ selected for residual strain analysis	**(101)**	**(110)**	**(112)**	**(211)**
ν_{hkl} (Kröner model)	0.323	0.331	0.319	0.329
η^* (°) zero strain reference angle	44.3	44.8	44.1	44.7

The residual strains were measured in all three APS doped coatings by evaluating the radius of the pseudo-rings associated with the main lattice planes of t'-YSZ at each 5° increments around the azimuth and comparing it with the radius of the pseudo-ring measured at η^* for each plane. The radius at η^* can be related to the d_0, zero-strain

reference. The deviations of the radius of the pseudo-ring with respect to the reference radius were measured in the out-of-plane (e_{11}) and in-plane (e_{22}) directions.

6.4.3 Residual strain results

The strain results are presented in Figure 6.5 for the temperature range from room temperature to 800°C and in Figure 6.6 for the temperature range from 800°C to 1100°C. It can be noted that, although three measurements were achieved at a distinct location in each coating (1 mm between each line scan), the trend of strain with respect to depth is well defined and corroborated by the multiple measurements. The results of the three line scan measurements for residual strains found in the coatings are plotted together, with their specific error bars. Tensile in-plane (e_{22}) strains were found in all three samples, which can be explained by the almost as-deposited condition of the YSZ in the TBC. APS TBCs usually exhibit in-plane tensile strains due to the prominence of residual stress created during spray deposition and splat quenching [236]. The sample containing the double-layer configuration, that includes YSZ:Er,Eu at the top surface, was found to have a higher magnitude of strain within the doped layer, which can be explained by the deposition process that implied some cooling time in between the deposition of the distinct layers

and may be also due to a low surface temperature of the underlying substrate during the spraying process [226, 237].

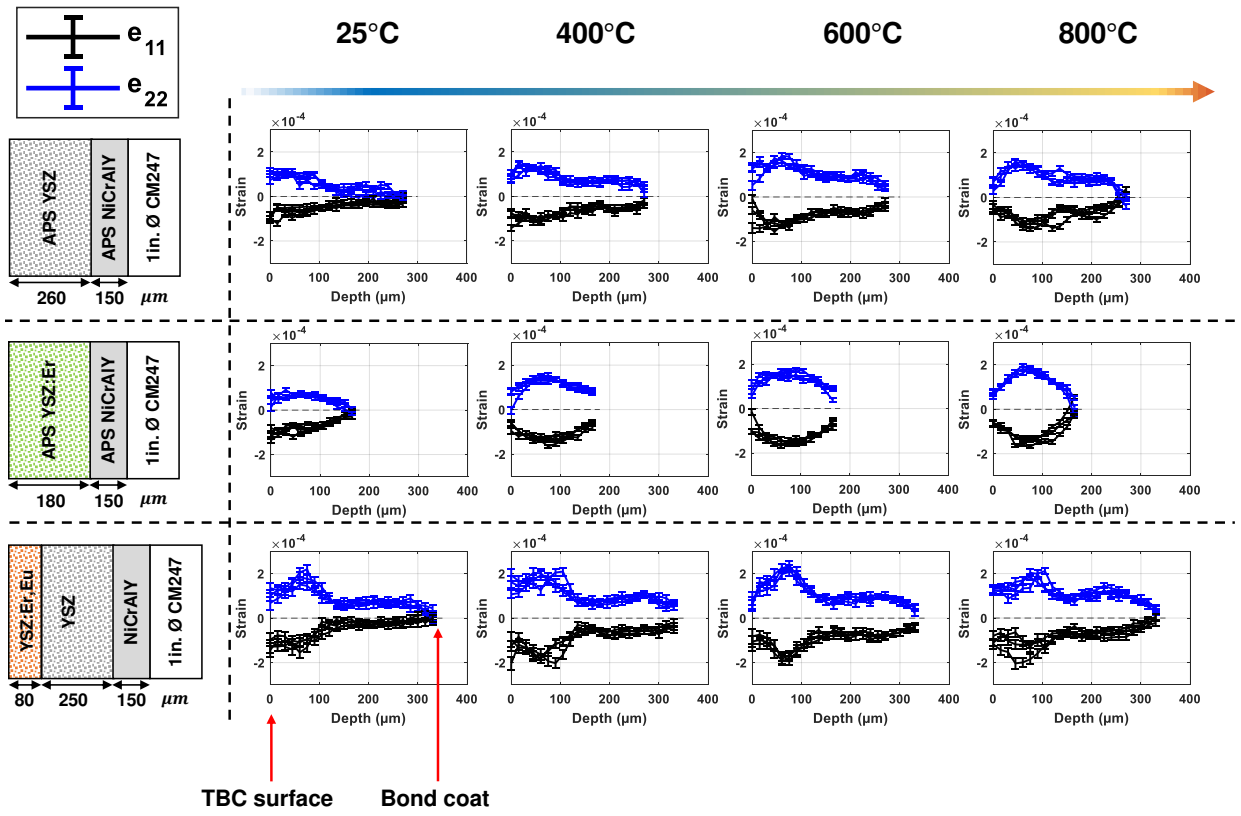

Figure 6.5: Residual strain measurements into the depth of the coatings, from room temperature to 800°C.

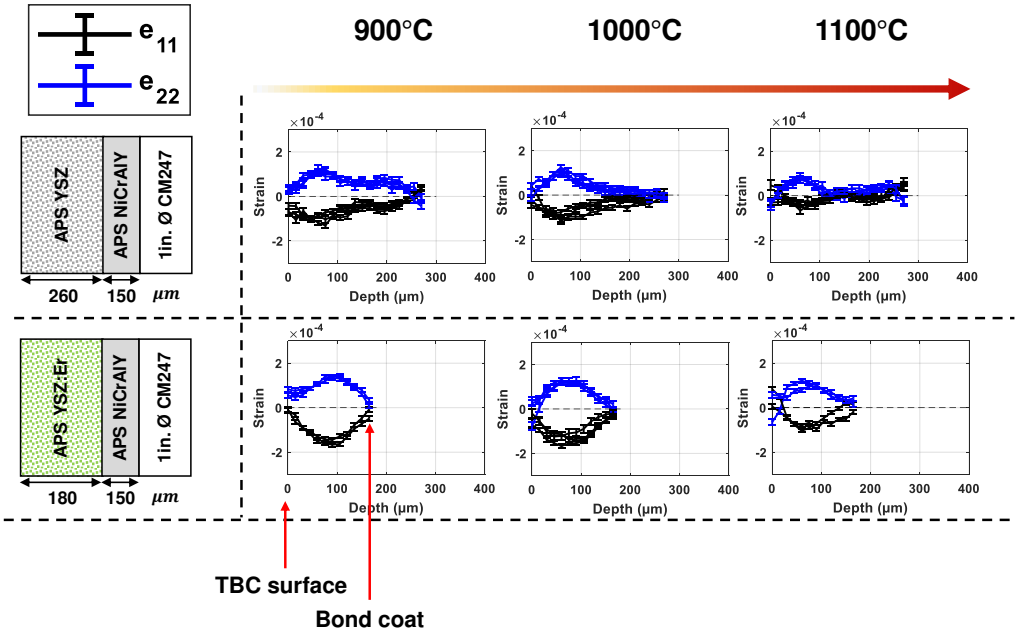

Figure 6.6: Residual strain measurements into the depth of the coatings, from 800°C to 1100°C.

The strain results obtained with the three line scans for each sample were averaged and plotted in Figure 6.7, Figure 6.8 and Figure 6.9 to better highlight the variation of strain magnitudes with TBC depth and temperature. It can be highlighted that the samples tested in this part contain low residual strains. In addition, the rare-earth doping was not found to affect significantly the strain magnitudes, which is a positive indication for the applicability of such luminescent coatings to industrial TBCs. Closer to turbine operating temperatures, residual strains were found to be reduced to almost a relaxed state, which is favorable for the utilization of these coatings in real engine environments.

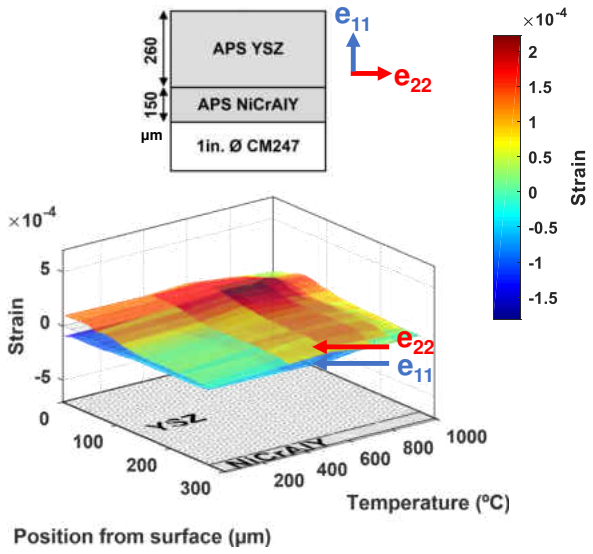

Figure 6.7: Strain results for the reference YSZ sample.

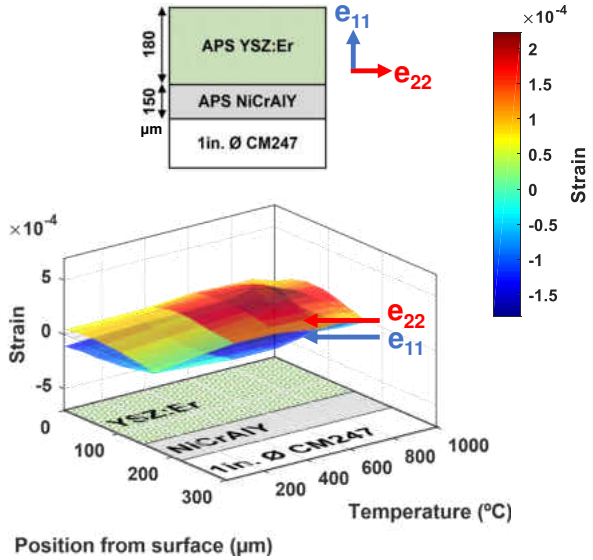

Figure 6.8: Strain results for the luminescent YSZ:Er sample.

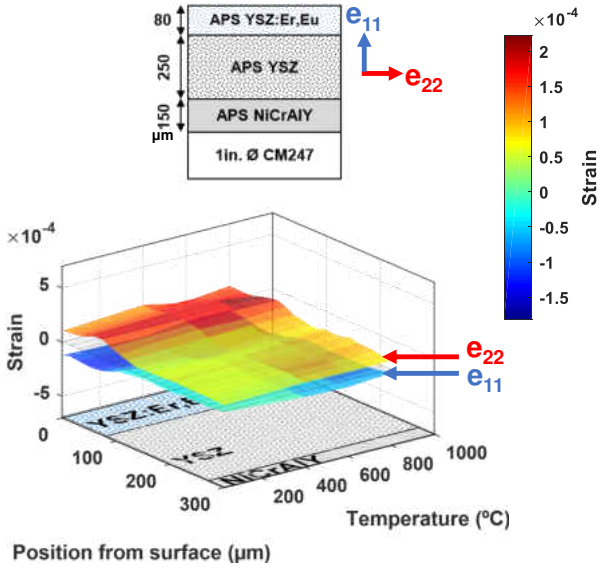

Figure 6.9: Strain results for the luminescent YSZ:Er,Eu sample.

Figure 6.10 represents the 2D diffraction pattern collected from the YSZ:Er,Eu co-doped sample at the interface between the YSZ:Er,Eu layer and the undoped YSZ layer while the sample was maintained at 800°C. To confirm the strain magnitude at the interface between YSZ and YSZ:Er,Eu, the strain analysis was performed into each of the main lattice planes, namely (101), (110), (112) and (211), and was measured by fitting the rings around the azimuth to get the 1D variations of d-spacing that can be related to residual strain. This thorough analysis confirms the presence of a strain concentration at the interface between undoped and doped layers. The 2D diffraction pattern further confirms

that the measured coatings possess random crystal orientation, which is typical for APS deposited coatings.

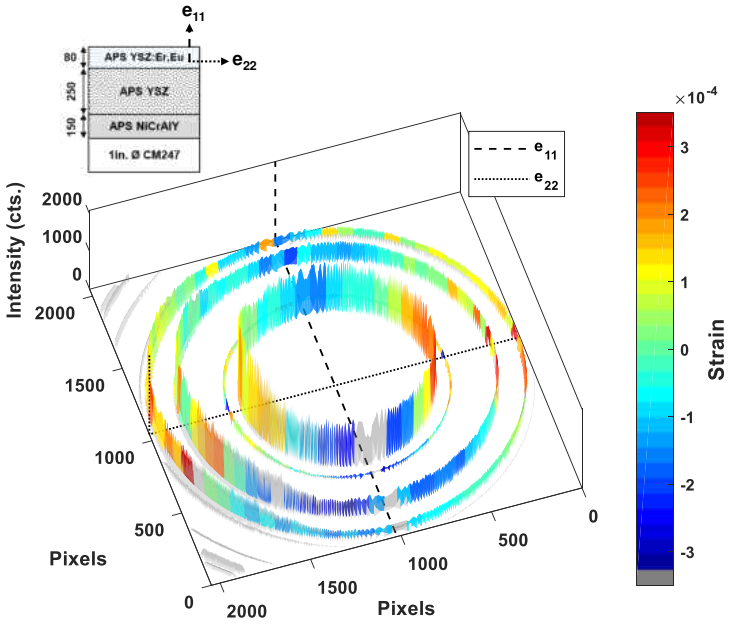

Figure 6.10: X-ray diffraction rings obtained for the co-doped APS YSZ:Er,Eu and associated residual strains calculated for the distinct t'-YSZ lattice planes.

6.5 Coefficients of thermal expansion

Coefficients of thermal expansion (CTE) were calculated at each temperature hold, probing samples at their top surface, and measuring the radius of the diffraction ring at η^* to find the value of d-spacing of peak (101) of t'-YSZ that is exclusively affected by

thermal expansion. The d-spacings that were obtained are reported in Figure 6.11. From the d-spacing, the volume expansion of the samples due to temperature was calculated and is presented in Figure 6.12. It was found that the typical expansion in YSZ TBCs is of the order of 1 % at about 900°C.

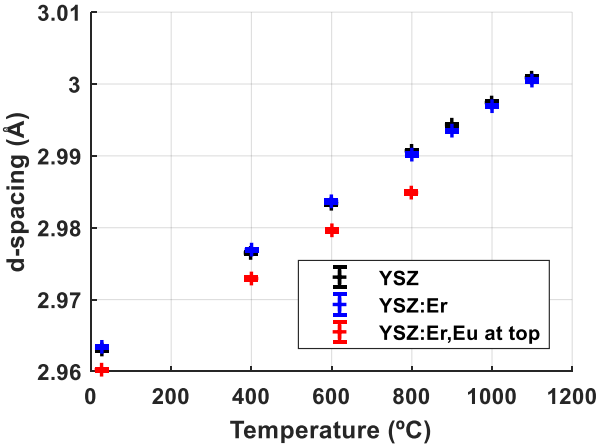

Figure 6.11: d-spacing of YSZ, YSZ:Er and YSZ:Er,Eu TBCs.

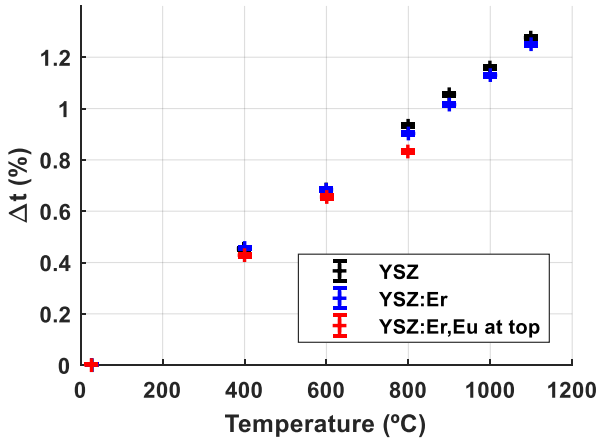

Figure 6.12: Lattice expansion of YSZ, YSZ:Er and YSZ:Er,Eu TBCs due to temperature.

Equation 6.7 was then used to obtain the coefficients of thermal expansion for all three samples, and the results are presented in Figure 6.13.

$$\alpha = \frac{\Delta l}{l_0 \cdot \Delta T} \tag{6.7}$$

where Δl is the change of d-spacing evaluated on the diffraction pattern at the angle η^* at a given temperature, l_0 is the d-spacing measured at η^* at room temperature, and ΔT is the change in temperature with respect to room temperature.

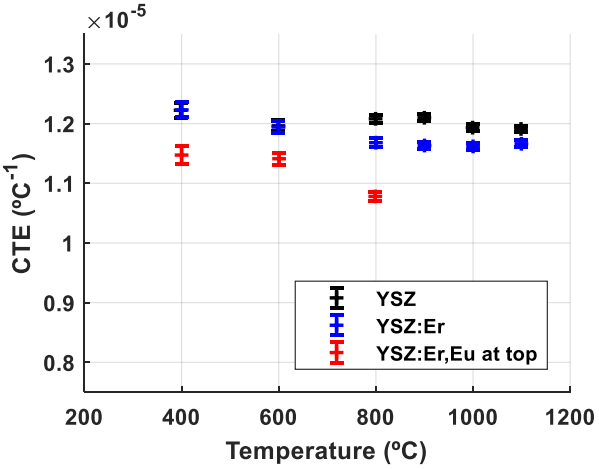

Figure 6.13: Coefficient of thermal expansion of YSZ, YSZ:Er and YSZ:Er,Eu TBCs.

The coefficients of thermal expansion were found to be relatively similar from the values available in literature [16, 66, 238, 239]. The substitution of YSZ by YSZ:Er was found to induce no change in the coefficient of thermal expansion up to 600°C, and a 2 % reduction at 1100°C. Therefore, the amount of doping chosen for this study is expected not to contribute significantly to a reduction of the thermal cycling performance of the TBCs. Concerning the coating containing the co-doped YSZ:Er,Eu layer at the top of the TBC, its lower coefficient of thermal expansion (about 10 %) might affect the mechanical response of the coating as it has an increased propensity to build stress through expansion mismatch with the surrounding materials constituting the TBC, or phase change.

As a conclusive remark for this study, the synchrotron experiments provide an insight into the effects of dopants on strain and thermal expansion within the coatings and the results show minimum changes compared to the reference, with the greatest variations localized at the interface between the sensing layer and the standard material, although it is a typical trait for multi-layer configurations to exhibit strain concentration due to mismatch in thermomechanical properties in between the different layers. The results point to the benefits of fully doped configurations, which are characterized by consistent strain throughout the depth of the coatings.

CHAPTER 7
CONCLUSIONS AND PERSPECTIVES

7.1 General conclusions

This work intends to provide novel methods and solutions to create sensing capabilities for improved characterization of Thermal Barrier Coatings, especially under extreme environments. To address this challenge, the design of configurations with rare-earth luminescent dopant ions integrated into TBCs was proposed to enable material sensing capabilities. Supporting models were constructed based on the radiative properties of the materials constituting TBCs. TBC configurations were fabricated and the best configurations for Phosphor Thermometry were tested using an advanced instrumentation that is able to collect both luminescence lifetime decays and intensities. The samples were further characterized by synchrotron XRD transmission to ensure the integrity of such materials for potential industrial implementation.

The contributions that this work attempts to yield for the scientific community include:

- A four-flux Kubelka-Munk model has been extended to be applicable for the life-time decay method using Phosphor Thermometry, in presence of a thermal gradient through the thickness of the coatings. The model is able to provide, for any TBC layer configuration, the sub-surface position at which the temperature measurement is achieved via Phosphor Thermometry, and initial experimental results validated the luminescence model using a YSZ:Er TBC.

- The measurable range of temperature using Phosphor Thermometry was extended, with increased sensitivity, by capturing the luminescence simultaneously out of a co-doped YSZ:Er,Eu top layer.

- An approach for modeling intensities based on internal reflectivity considerations to establish delamination progression in coatings was undertaken and its results were compared with experiments.

- A YSZ:Er coating that includes a sensing layer placed uniquely at the top surface was able to track an underlying delamination area with sufficient contrast, which was found to be encouraging for the development of faster damage detection methods.

- The effects of dopant layer thickness on the expected luminescence intensity have been evaluated through modeling: It was found that the increase of thickness for a doped layer placed on the top of the TBC results in an increase of the collectable lu-

minescence intensity until a threshold that indicates a limit of detection in the depth of the coating, which depends mainly on the excitation and emission wavelengths.

- Configurations, including one of the first successful sub-surface measurements from entirely doped top coat, were evaluated and tested. The results show potential for enhanced temperature measurement capabilities using Phosphor Thermometry, including the revealing of temperature gradients acting through the depth of the coatings.

- Rare-earth doped bond coat configurations were fabricated in the attempt of producing Thermally Grown Oxides that can be used as Phosphor Thermometry sensor layers with limited success up to this point, due to the low aging applied on the manufactured samples as well as the fairly inefficient deposition of the bond coats during production using Air Plasma Spray.

7.2 Future work

The model developed in this work has been successfully validated for extended temperature sensing, temperature gradient sensing and delamination sensing, demonstrating significant potential for enhanced sensing capabilities for various applications with further development. In the future, it will be necessary to compare experiments with the outcomes

of the different models to further adjust the input parameters and establish stronger correlations to adjust the thermal and optical properties of different dopants configurations and applied to more coating microstructures. With unique efforts initiated using doped bond coats, *in-situ* TGO tracking using the instrumentation developed can provide significant insight into the lifetime prediction of TBCs.

LIST OF REFERENCES

[1] L. Yang, D. Peng, C. Zhao, C. Xing, F. Guo, Z. Yao, Y. Liu, X. Zhao, and P. Xiao, "Evaluation of the in-depth temperature sensing performance of Eu-and Dy-doped YSZ in air plasma sprayed thermal barrier coatings," *Surface and Coatings Technology*, vol. 316, pp. 210–218, 2017.

[2] Y. Shen, M. Chambers, and D. Clarke, "Effects of dopants and excitation wavelength on the temperature sensing of Ln^{3+}-doped 7YSZ," *Surface and Coatings Technology*, vol. 203, no. 5-7, pp. 456–460, 2008.

[3] A. Stuke, H. Kassner, J.-L. Marqués, R. Vassen, D. Stöver, and R. Carius, "Suspension and air plasma-sprayed ceramic thermal barrier coatings with high infrared reflectance," *International Journal of Applied Ceramic Technology*, vol. 9, no. 3, pp. 561–574, 2012.

[4] A. M. Limarga and D. R. Clarke, "Characterization of electron beam physical vapor-deposited thermal barrier coatings using diffuse optical reflectance," *International Journal of Applied Ceramic Technology*, vol. 6, no. 3, pp. 400–409, 2009.

[5] G. Yang and C. Zhao, "A comparative experimental study on radiative properties of eb-pvd and air plasma sprayed thermal barrier coatings," *Journal of Heat Transfer*, vol. 137, no. 9, p. 091024, 2015.

[6] ——, "Infrared radiative properties of eb-pvd thermal barrier coatings," *International Journal of Heat and Mass Transfer*, vol. 94, no. 9, pp. 199–210, 2016.

[7] R. A. Miller, "Thermal barrier coatings for aircraft engines: history and directions," *Journal of Thermal Spray Technology*, vol. 6, no. 1, p. 35, 1997.

[8] ——, "Ceramic thermal barrier coatings for electric utility gas turbine engines," 1986.

[9] C. H. Liebert, R. E. Jacobs, S. Stecura, and C. R. Morse, "Durability of zirconia thermal-barrier ceramic coatings on air-cooled turbine blades in cyclic jet engine operation," *NASA Report*, 1976.

[10] N. P. Padture, M. Gell, and E. H. Jordan, "Thermal barrier coatings for gas-turbine engine applications," *Science*, vol. 296, no. 5566, pp. 280–284, 2002.

[11] S. Lakiza, M. Grechanyuk, O. Ruban, V. Redko, M. Glabay, O. Myloserdov, O. Dudnik, and S. Prokhorenko, "Thermal barrier coatings: current status, search, and analysis," *Powder Metallurgy and Metal Ceramics*, vol. 57, no. 1-2, pp. 82–113, 2018.

[12] P. G. Hill and C. R. Peterson, "Mechanics and thermodynamics of propulsion," *Reading, MA, Addison-Wesley Publishing Co., 1992, 764 p.*, 1992.

[13] A. Khalid, K. Kontis, and H. Behtash, "Phosphor thermometry in gas turbines: consideration factors," *Proceedings of the Institution of Mechanical Engineers, Part G: Journal of Aerospace Engineering*, vol. 224, no. 7, pp. 745–755, 2010.

[14] M. Peters, K. Fritscher, G. Staniek, W. Kaysser, and U. Schulz, "Design and properties of thermal barrier coatings for advanced turbine engines," *Materialwissenschaft und Werkstofftechnik*, vol. 28, no. 8, pp. 357–362, 1997.

[15] L. Xu, S. Bo, Y. Hongde, and W. Lei, "Evolution of rolls-royce air-cooled turbine blades and feature analysis," *Procedia Engineering*, vol. 99, pp. 1482–1491, 2015.

[16] J. Brandon and R. Taylor, "Phase stability of zirconia-based thermal barrier coatings part i. zirconia-yttria alloys," *Surface and Coatings Technology*, vol. 46, no. 1, pp. 75–90, 1991.

[17] R. Sobhanverdi and A. Akbari, "Porosity and microstructural features of plasma sprayed yttria stabilized zirconia thermal barrier coatings," *Ceramics International*, vol. 41, no. 10, pp. 14 517–14 528, 2015.

[18] A. Abdul-Aziz, "Durability modeling review of thermal-and environmental-barrier-coated fiber-reinforced ceramic matrix composites part i," *Materials*, vol. 11, no. 7, p. 1251, 2018.

[19] L. Rossmann, "Analysis of residual stress and damage mechanisms of thermal barrier coatings deposited via ps-pvd and eb-pvd," 2019.

[20] X. Cao, R. Vassen, and D. Stoever, "Ceramic materials for thermal barrier coatings," *Journal of the European Ceramic Society*, vol. 24, no. 1, pp. 1–10, 2004.

[21] M. Schutze, *Corrosion and environmental degradation*. Wiley-Vch, 2000.

[22] X. Li, X. Huang, Q. Yang, and Z. Tang, "Effects of substrate material and tbc structure on the cyclic oxidation resistance of tbc systems," *Surface and Coatings Technology*, vol. 258, pp. 49–61, 2014.

[23] B. Saeedi, A. Sabour, A. Ebadi, and A. Khoddami, "Influence of the thermal barrier coatings design on the oxidation behavior," *Journal of materials science & technology*, vol. 25, no. 4, p. 499, 2009.

[24] N. Czech, H. Fietzek, M. Juez-Lorenzo, V. Kolarik, and W. Stamm, "Studies of the bond-coat oxidation and phase structure of tbcs," *Surface and Coatings Technology*, vol. 113, no. 1-2, pp. 157–164, 1999.

[25] E. P. Busso, Z. Qian, M. Taylor, and H. Evans, "The influence of bondcoat and topcoat mechanical properties on stress development in thermal barrier coating systems," *Acta materialia*, vol. 57, no. 8, pp. 2349–2361, 2009.

[26] A. Heuer, "Oxygen and aluminum diffusion in α-al2o3: how much do we really understand?" *Journal of the European Ceramic Society*, vol. 28, no. 7, pp. 1495–1507, 2008.

[27] R. D. Jackson, "The effect of bond coat oxidation on the microstructure and endurance of two thermal barrier coating systems," Ph.D. dissertation, University of Birmingham, 2010.

[28] P. Fauchais, "Understanding plasma spraying," *Journal of Physics D: Applied Physics*, vol. 37, no. 9, p. R86, 2004.

[29] V. Postolenko, "Failure mechanisms of thermal barrier coatings for high temperature gas turbine components under cyclic thermal loading," Ph.D. dissertation, Universitätsbibliothek, 2008.

[30] D. Stöver, G. Pracht, H. Lehmann, M. Dietrich, J.-E. Döring, and R. Vassen, "New material concepts for the next generation of plasma-sprayed thermal barrier coatings," *Journal of thermal spray technology*, vol. 13, no. 1, pp. 76–83, 2004.

[31] N. R. Muktinutalapati, "Materials for gas turbines–an overview," in *Advances in Gas Turbine Technology*. InTech, 2011.

[32] R. C. Reed, *The superalloys: fundamentals and applications*. Cambridge university press, 2008.

[33] A. Vardelle, C. Moreau, N. J. Themelis, and C. Chazelas, "A perspective on plasma spray technology," *Plasma Chemistry and Plasma Processing*, vol. 35, no. 3, pp. 491–509, 2015.

[34] E. Bakan and R. Vassen, "Ceramic top coats of plasma-sprayed thermal barrier coatings: materials, processes, and properties," *Journal of Thermal Spray Technology*, vol. 26, no. 6, pp. 992–1010, 2017.

[35] S. Stecura, "Optimization of the nicrai-y/zro2-y2o3 thermal barrier system," *NASA, Lewis Research Center, Cleveland, OH*, 1985.

[36] A. Guignard, *Development of thermal spray processes with liquid feedstocks*. Forschungszentrum Jülich, 2012, vol. 141.

[37] Y. Liu, Y. Liu, P. Lours, T. Sentenac, V. Vidal, Z. Wang, and K. Ding, "Influence of isothermal aging conditions on aps tbc's interfacial fracture toughness," *Surface and Coatings Technology*, vol. 313, pp. 417–424, 2017.

[38] R. B. Dinwiddie, S. C. Beecher, W. D. Porter, and B. A. Nagaraj, "The effect of thermal aging on the thermal conductivity of plasma sprayed and eb-pvd thermal barrier coatings," in *ASME 1996 International Gas Turbine and Aeroengine Congress and Exhibition*. American Society of Mechanical Engineers, 1996, pp. V005T13A006–V005T13A006.

[39] S. Aruna, B. A. Paligan, N. Balaji, and V. P. Kumar, "Properties of plasma sprayed yttria stabilized zirconia thermal barrier coating prepared from co-precipitation synthesized powder," *Ceramics International*, vol. 40, no. 7, pp. 11 157–11 162, 2014.

[40] T. Kakuda, *Phase of Photothermal Emission Analysis as a Diagnostic Tool for Thermal Barrier Coatings on Serviceable Engine Components*. University of California, Santa Barbara, 2010.

[41] D. Renusch, M. Schorr, and M. Schütze, "The role that bond coat depletion of aluminum has on the lifetime of aps-tbc under oxidizing conditions," *Materials and corrosion*, vol. 59, no. 7, pp. 547–555, 2008.

[42] C. Bargraser, P. Mohan, K. Lee, B. Yang, J. Suk, S. Choe, and Y. Sohn, "Life approximation of thermal barrier coatings via quantitative microstructural analysis," *Materials Science and Engineering: A*, vol. 549, pp. 76–81, 2012.

[43] J. Singh and D. E. Wolfe, "Review nano and macro-structured component fabrication by electron beam-physical vapor deposition (eb-pvd)," *Journal of materials Science*, vol. 40, no. 1, pp. 1–26, 2005.

[44] J. A. Thornton, "High rate thick film growth," *Annual review of materials science*, vol. 7, no. 1, pp. 239–260, 1977.

[45] R. F. Bunshah, *Deposition technologies for films and coatings: developments and applications*, 1982.

[46] H. Lau, "Influence of yttria on the cyclic lifetime of ysz tbc deposited on eb-pvd nicocraly bondcoats and its contribution to a modified tbc adhesion mechanism," *Surface and Coatings Technology*, vol. 235, pp. 121–126, 2013.

[47] G. Goward, "Protective coatings for high temperature gas turbine alloys a review of the state of technology," in *Surface Engineering*. Springer, 1984, pp. 408–426.

[48] J. Liu, "Mechanisms of lifetime improvement in thermal barrier coatings with hf and/or y modification of cmsx-4 superalloy substrates," 2007.

[49] F. Cernuschi, C. Guardamagna, S. Capelli, L. Lorenzoni, D. Mack, and A. Moscatelli, "Solid particle erosion of standard and advanced thermal barrier coatings," *Wear*, vol. 348, pp. 43–51, 2016.

[50] X. Bi, H. Xu, and S. Gong, "Investigation of the failure mechanism of thermal barrier coatings prepared by electron beam physical vapor deposition," *Surface and Coatings Technology*, vol. 130, no. 1, pp. 122–127, 2000.

[51] K. Von Niessen and M. Gindrat, "Plasma spray-pvd: a new thermal spray process to deposit out of the vapor phase," *Journal of thermal spray technology*, vol. 20, no. 4, pp. 736–743, 2011.

[52] W. Y. Lee, D. P. Stinton, C. C. Berndt, F. Erdogan, Y.-D. Lee, and Z. Mutasim, "Concept of functionally graded materials for advanced thermal barrier coating applications," *Journal of the American Ceramic Society*, vol. 79, no. 12, pp. 3003–3012, 1996.

[53] G. Lim and A. Kar, "Radiative properties of thermal barrier coatings at high temperatures," *Journal of Physics D: Applied Physics*, vol. 42, no. 15, p. 155412, 2009.

[54] J. R. Nicholls, K. Lawson, A. Johnstone, and D. Rickerby, "Methods to reduce the thermal conductivity of eb-pvd tbcs," *Surface and Coatings Technology*, vol. 151, pp. 383–391, 2002.

[55] R. Steenbakker, "Phosphor thermometry in an eb-pvd tbc," *PhD Thesis*, 2008.

[56] A. Rabiei and A. Evans, "Failure mechanisms associated with the thermally grown oxide in plasma-sprayed thermal barrier coatings," *Acta materialia*, vol. 48, no. 15, pp. 3963–3976, 2000.

[57] L. Yang, F. Yang, Y. Long, Y. Zhao, X. Xiong, X. Zhao, and P. Xiao, "Evolution of residual stress in air plasma sprayed yttria stabilised zirconia thermal barrier coatings after isothermal treatment," *Surface and Coatings Technology*, vol. 251, pp. 98–105, 2014.

[58] P. Planques, V. Vidal, P. Lours, V. Proton, F. Crabos, J. Huez, and B. Viguier, "Mechanical and thermo-physical properties of plasma-sprayed thermal barrier coatings: a literature survey," *Oxidation of Metals*, vol. 88, no. 1-2, pp. 133–143, 2017.

[59] J. Petit, "Monocristaux dopés ytterbium et matériaux assemblés pour lasers de fortes puissances," Ph.D. dissertation, Paris 6, 2006.

[60] H. Dong, G.-J. Yang, C.-X. Li, X.-T. Luo, and C.-J. Li, "Effect of tgo thickness on thermal cyclic lifetime and failure mode of plasma-sprayed tbc s," *Journal of the American Ceramic Society*, vol. 97, no. 4, pp. 1226–1232, 2014.

[61] R. T. Wu, "Mechanisms of high temperature degradation of thermal barrier coatings." 2009.

[62] M. Shahid and M. Abbas, "Investigation of failure mechanism of thermal barrier coatings (tbcs) deposited by eb-pvd technique," in *Journal of Physics: Conference Series*, vol. 439, no. 1. IOP Publishing, 2013, p. 012021.

[63] R. Kumar, "Low thermal conductivity yag-based thermal barrier coatings with enhanced cmas resistance," 2018.

[64] L. Wang, Y. Zhao, X. Zhong, S. Tao, W. Zhang, and Y. Wang, "Influence of island-like oxides in the bond-coat on the stress and failure patterns of the thermal-barrier coatings fabricated by atmospheric plasma spraying during long-term high temperature oxidation," *Journal of thermal spray technology*, vol. 23, no. 3, pp. 431–446, 2014.

[65] W. Chen, X. Wu, B. Marple, D. Nagy, and P. Patnaik, "Tgo growth behaviour in tbcs with aps and hvof bond coats," *Surface and Coatings Technology*, vol. 202, no. 12, pp. 2677–2683, 2008.

[66] N. Yanar, M. Helminiak, G. Meier, and F. Pettit, "Comparison of the failures during cyclic oxidation of yttria-stabilized (7 to 8 weight percent) zirconia thermal barrier coatings fabricated via electron beam physical vapor deposition and air plasma spray," *Metallurgical and Materials Transactions A*, vol. 42, no. 4, pp. 905–921, 2011.

[67] N. Cheruvu, K. Chan, and R. Viswanathan, "Evaluation, degradation and life assessment of coatings for land based combustion turbines," *Energy Materials*, vol. 1, no. 1, pp. 33–47, 2006.

[68] R. Vaßen, M. O. Jarligo, T. Steinke, D. E. Mack, and D. Stöver, "Overview on advanced thermal barrier coatings," *Surface and Coatings Technology*, vol. 205, no. 4, pp. 938–942, 2010.

[69] J. D. Osorio, A. Toro, and J. P. Hernandez-Ortiz, "Thermal barrier coatings for gas turbine applications: failure mechanisms and key microstructural features," *Dyna*, vol. 79, no. 176, pp. 149–158, 2012.

[70] B. Franke, "Nondestructive evaluation of thermal barrier coatings with thermal wave imaging and photostimulated luminescence spectroscopy," 2005.

[71] M. Madhwal, E. H. Jordan, and M. Gell, "Failure mechanisms of dense vertically-cracked thermal barrier coatings," *Materials Science and Engineering: A*, vol. 384, no. 1-2, pp. 151–161, 2004.

[72] G. Witz, V. Shklover, W. Steurer, S. Bachegowda, and H. Bossmann, "Monitoring the phase evolution of yttria stabilized zirconia in thermal barrier coatings using the rietveld method," in *Advanced ceramic coatings and interfaces II: a collection of papers presented at the 31st International Conference on Advanced Ceramics and Composites, January 21-26, 2007, Daytona Beach, Florida*, vol. 28, no. 3. John Wiley, 2008, pp. 41–51.

[73] G. Witz, V. Shklover, W. Steurer, S. Bachegowda, and H.-P. Bossmann, "Phase evolution in yttria-stabilized zirconia thermal barrier coatings studied by rietveld refinement of x-ray powder diffraction patterns," *Journal of the American Ceramic Society*, vol. 90, no. 9, pp. 2935–2940, 2007.

[74] N. Song, Z. Wang, Y. Xing, M. Zhang, P. Wu, F. Qian, J. Feng, L. Qi, C. Wan, and W. Pan, "Evaluation of phase transformation and mechanical properties of metastable yttria-stabilized zirconia by nanoindentation," *Materials*, vol. 12, no. 10, p. 1677, 2019.

[75] J. D. Osorio, A. Lopera-Valle, A. Toro, and J. P. Hernández-Ortiz, "Phase transformations in air plasma-sprayed yttria-stabilized zirconia thermal barrier coatings," *Dyna*, vol. 81, no. 185, pp. 13–18, 2014.

[76] J. Chevalier, L. Gremillard, A. V. Virkar, and D. R. Clarke, "The tetragonal-monoclinic transformation in zirconia: lessons learned and future trends," *Journal of the American Ceramic Society*, vol. 92, no. 9, pp. 1901–1920, 2009.

[77] A. H. Khalid and K. Kontis, "Thermographic phosphors for high temperature measurements: principles, current state of the art and recent applications," *Sensors*, vol. 8, no. 9, pp. 5673–5744, 2008.

[78] R. Singh and F. CEng, "Civil aero gas turbines: Technology & strategy," *Aero India*, 2003.

[79] M. R. Reyhani, M. Alizadeh, A. Fathi, and H. Khaledi, "Turbine blade temperature calculation and life estimation-a sensitivity analysis," *Propulsion and power Research*, vol. 2, no. 2, pp. 148–161, 2013.

[80] R. J. Steenbakker, J. P. Feist, R. G. Wellman, and J. R. Nicholls, "Sensor thermal barrier coatings: Remote in situ condition monitoring of EB-PVD coatings at elevated temperatures," *Journal of Engineering for Gas Turbines and Power*, vol. 131, no. 4, p. 041301, 2009.

[81] J. Ruud, Y. Lau, and V. Kwasniewski, "Increased fuel efficiency and decreased emissions through tbcs," *Published in Performance of the Third*, vol. 50, pp. 950–4, 2003.

[82] G. Lipiak, S. Bussmann, C. Steinwachs, and A. Luttenberg, "Lifetime extension for siemens gas turbines," in *Power Gen Europe*, 2006.

[83] J. Thapa, B. Liu, S. D. Woodruff, B. T. Chorpening, and M. P. Buric, "Raman scattering in single-crystal sapphire at elevated temperatures," *Applied optics*, vol. 56, no. 31, pp. 8598–8606, 2017.

[84] Y. Zhang, D. E. Mack, G. Mauer, and R. Vaßen, "Laser cladding of embedded sensors for thermal barrier coating applications," *Coatings*, vol. 8, no. 5, p. 176, 2018.

[85] Y. Tan, J. P. Longtin, S. Sampath, and D. Zhu, "Temperature-gradient effects in thermal barrier coatings: An investigation through modeling, high heat flux test,

and embedded sensor," *Journal of the American Ceramic Society*, vol. 93, no. 10, pp. 3418–3426, 2010.

[86] J. Feist, A. Heyes, and S. Seefelt, "Thermographic phosphor thermometry for film cooling studies in gas turbine combustors," *Proceedings of the Institution of Mechanical Engineers, Part A: Journal of Power and Energy*, vol. 217, no. 2, pp. 193–200, 2003.

[87] R. A. Hansel, *Phosphor thermometry using rare-earth doped materials*. Vanderbilt University, 2010.

[88] C. Lempereur, R. Andral, and J. Prudhomme, "Surface temperature measurement on engine components by means of irreversible thermal coatings," *Measurement Science and Technology*, vol. 19, no. 10, p. 105501, 2008.

[89] M. Jahanmiri, "Pressure sensitive paints: the basics & applications," Chalmers University of Technology, Tech. Rep., 2011.

[90] C. Knappe, *Phosphor Thermometry on Surfaces-A Study of its Methodology and its Practical Applications*, 2013.

[91] A. Yañez Gonzalez, "Phosphorescent thermal history sensors for extreme environments," 2015.

[92] F. E. Pfefferkorn, F. P. Incropera, and Y. C. Shin, "Surface temperature measurement of semi-transparent ceramics by long-wavelength pyrometry," in *ASME 2002 International Mechanical Engineering Congress and Exposition*. American Society of Mechanical Engineers Digital Collection, 2008, pp. 137–146.

[93] A. Y. Gonzalez, C. Pilgrim, P. Sollazzo, A. Heyes, J. Feist, J. Nicholls, and F. Beyrau, "Temperature sensing inside thermal barrier coatings using phosphor thermometry," 2014.

[94] S. Alaruri, L. Bianchini, and A. Brewington, "Effective spectral emissivity measurements of superalloys and ysz thermal barrier coating at high temperatures using a 1.6 μm single wavelength pyrometer," *Optics and lasers in engineering*, vol. 30, no. 1, pp. 77–91, 1998.

[95] S. D. Alaruri, L. Bianchini, and A. Brewington, "Emissivity measurements for ysz thermal barrier coating at high temperatures using a 1.6-um single-wavelength pyrometer," *Optical Engineering*, vol. 37, no. 2, pp. 683–688, 1998.

[96] L. M. Chepyga, A. Osvet, C. J. Brabec, and M. Batentschuk, "High-temperature thermographic phosphor mixture yap/yag: Dy3+ and its photoluminescence properties," *Journal of Luminescence*, vol. 188, pp. 582–588, 2017.

[97] A. Heyes, "On the design of phosphors for high-temperature thermometry," *Journal of Luminescence*, vol. 129, no. 12, pp. 2004–2009, 2009.

[98] E. Hertle, L. Chepyga, M. Batentschuk, and L. Zigan, "Influence of codoping on the luminescence properties of yag: Dy for high temperature phosphor thermometry," *Journal of Luminescence*, vol. 182, pp. 200–207, 2017.

[99] V. Lojpur, S. Ćulubrk, M. Medić, and M. Dramicanin, "Luminescence thermometry with eu3+ doped gdalo3," *Journal of Luminescence*, vol. 170, pp. 467–471, 2016.

[100] J. Feist, S. Karmakar Biswas, C. Pilgrim, P. Sollazzo, and S. Berthier, "Off-line temperature profiling utilizing phosphorescent thermal history paints and coatings," *Journal of Turbomachinery*, vol. 137, no. 10, 2015.

[101] C. Pilgrim, A. Y. Gonzalez, R. Saggese, R. Krewinkel, M. Blaswich, J. Feist, U. Orth, M. Rabs, D. Frank, and S. A. Rodriguez, "Surface temperature measurements in an industrial gas turbine using thermal history paints," in *12 th European Conference on Turbomachinery Fluid dynamics & Thermodynamics*. EUROPEAN TURBOMACHINERY SOCIETY, 2017.

[102] A. Heyes, A. Rabhiou, J. Feist, and A. Kempf, "Thermal history sensing with thermographic phosphors," in *AIP Conference Proceedings*, vol. 1552, no. 1. AIP, 2013, pp. 891–896.

[103] C. Kerr and P. Ivey, "An overview of the measurement errors associated with gas turbine aeroengine pyrometer systems," *Measurement science and technology*, vol. 13, no. 6, p. 873, 2002.

[104] C. Bird, J. Mutton, R. Shepherd, M. Smith, and H. Watson, "Surface temperature measurement in turbines," in *AGARD conference proceedings*. AGARD, 1998, pp. 21–4.

[105] E. Copin, Y. Le Maoult, T. Sentenac, F. Blas, T. Tran, and P. Lours, "Comparison of ir thermography and reflectance-enhanced photoluminescence for early quantitative diagnostic of thermal barrier coatings spallation," in *12th International Conference on Quantitative InfraRed Thermography (QIRT 2014), Bordeaux, 07-11 July*, 2014.

[106] S. Allison, S. Goedeke, M. Cates, T. Bonsett, D. Smith, A. Brewington, and T. Bencic, "Phosphor thermometry in an operating turbine engine," in *41st AIAA/ASME/SAE/ASEE Joint Propulsion Conference & Exhibit*, 2005, p. 4374.

[107] J. Feist, A. Heyes, K. Choy, and B. Su, "Phosphor thermometry for high temperature gas turbine applications," in *ICIASF 99. 18th International Congress on Instrumentation in Aerospace Simulation Facilities. Record (Cat. No. 99CH37025)*. IEEE, 1999, pp. 6–1.

[108] F. A. Nada, A. Lantz, J. Larfeldt, N. Markocsan, M. Aldén, and M. Richter, "Remote temperature sensing on and beneath atmospheric plasma sprayed thermal barrier coatings using thermographic phosphors," *Surface and Coatings Technology*, vol. 302, pp. 359–367, 2016.

[109] A. Yañez Gonzalez, C. Pilgrim, J. Feist, P. Sollazzo, F. Beyrau, and A. Heyes, "Online temperature measurement inside a thermal barrier sensor coating during engine operation," *Journal of Turbomachinery*, vol. 137, no. 10, 2015.

[110] M. Aldén, A. Omrane, M. Richter, and G. Särner, "Thermographic phosphors for thermometry: a survey of combustion applications," *Progress in energy and combustion science*, vol. 37, no. 4, pp. 422–461, 2011.

[111] J. Brübach, C. Pflitsch, A. Dreizler, and B. Atakan, "On surface temperature measurements with thermographic phosphors: a review," *Progress in Energy and Combustion Science*, vol. 39, no. 1, pp. 37–60, 2013.

[112] D. Witkowski and D. A. Rothamer, "A methodology for identifying thermographic phosphors suitable for high-temperature gas thermometry: application to ce3+ and pr3+ doped oxide hosts," *Applied Physics B*, vol. 123, no. 8, p. 226, 2017.

[113] Q. Fouliard, S. Haldar, R. Ghosh, and S. Raghavan, "Modeling luminescence behavior for phosphor thermometry applied to doped thermal barrier coating configurations," *Applied Optics*, vol. 58, no. 13, pp. D68–D75, 2019.

[114] C. Pilgrim, J. Feist, and A. Heyes, "On the effect of temperature gradients and coating translucence on the accuracy of phosphor thermometry," *Measurement Science and Technology*, vol. 24, no. 10, p. 105201, 2013.

[115] M. Gentleman, J. Eldridge, D. Zhu, K. Murphy, and D. Clarke, "Non-contact sensing of TBC/BC interface temperature in a thermal gradient," *Surface and Coatings Technology*, vol. 201, no. 7, pp. 3937–3941, 2006.

[116] K. N. Shinde, S. Dhoble, H. Swart, and K. Park, "Basic mechanisms of photoluminescence," in *Phosphate Phosphors for Solid-State Lighting*. Springer, 2012, pp. 41–59.

[117] N. Ishiwada, E. Fujii, and T. Yokomori, "Evaluation of Dy-doped phosphors (YAG: Dy, Al_2O_3: Dy, and Y_2SiO_5: Dy) as thermographic phosphors," *Journal of Luminescence*, 2017.

[118] X. Wang, Q. Liu, Y. Bu, C.-S. Liu, T. Liu, and X. Yan, "Optical temperature sensing of rare-earth ion doped phosphors," *RSC Advances*, vol. 5, no. 105, pp. 86 219–86 236, 2015.

[119] N. Ishiwada, T. Ueda, and T. Yokomori, "Characteristics of rare earth (RE= Eu, Tb, Tm)-doped Y_2O_3 phosphors for thermometry," *Luminescence*, vol. 26, no. 6, pp. 381–389, 2011.

[120] N. Fuhrmann, J. Brübach, and A. Dreizler, "Phosphor thermometry: a comparison of the luminescence lifetime and the intensity ratio approach," *Proceedings of the Combustion Institute*, vol. 34, no. 2, pp. 3611–3618, 2013.

[121] S. Allison, L. Boatner, and G. Gillies, "Characterization of high-temperature thermographic phosphors: spectral properties of $LuPO_4$:Dy (1%), Eu (2%)," *Applied Optics*, vol. 34, no. 25, pp. 5624–5627, 1995.

[122] L. Mannik, S. Brown, and S. Campbell, "Phosphor-based thermometry of rotating surfaces," *Applied Optics*, vol. 26, no. 18, pp. 4014–4017, 1987.

[123] B. Heeg and T. Jenkins, "Precision and accuracy of luminescence lifetime-based phosphor thermometry: A case study of Eu (III): YSZ," in *AIP Conference Proceedings*, vol. 1552, no. 1. AIP, 2013, pp. 885–890.

[124] Y. Su, R. Trice, K. Faber, H. Wang, and W. Porter, "Thermal conductivity, phase stability, and oxidation resistance of y 3 al 5 o 12 (yag)/y 2 o 3–zro 2 (ysz) thermal-barrier coatings," *Oxidation of metals*, vol. 61, no. 3-4, pp. 253–271, 2004.

[125] M. Gell, J. Wang, R. Kumar, J. Roth, C. Jiang, and E. H. Jordan, "Higher temperature thermal barrier coatings with the combined use of yttrium aluminum garnet and the solution precursor plasma spray process," *Journal of Thermal Spray Technology*, pp. 1–13, 2018.

[126] M. Gentleman and D. Clarke, "Concepts for luminescence sensing of thermal barrier coatings," *Surface and coatings technology*, vol. 188, pp. 93–100, 2004.

[127] P. Ramanujam, "Synthesis and processing of nanocrystalline yag (yttrium aluminium garnet) ceramics," Ph.D. dissertation, © Prabhu Ramanujam, 2014.

[128] S. Skinner, J. Feist, I. Brooks, S. Seefeldt, and A. Heyes, "Yag: Ysz composites as potential thermographic phosphors for high temperature sensor applications," *Sensors and Actuators B: Chemical*, vol. 136, no. 1, pp. 52–59, 2009.

[129] M. S. Majewski, *Optical Diagnostics of Thermal Barrier Coatings*. University of Connecticut, 2010.

[130] A. H. Khalid, "Development of phosphor thermometry systems for use in development gas turbine engines," Ph.D. dissertation, University of Manchester, 2011.

[131] J. P. Feist, "Development of phosphor thermometry for gas turbines," Ph.D. dissertation, University of London, 2001.

[132] E. Hertle, L. Chepyga, M. Batentschuk, S. Will, and L. Zigan, "Temperature-dependent luminescence characteristics of dy 3+ doped in various crystalline hosts," *Journal of Luminescence*, vol. 204, 07 2018.

[133] A. Hashemi, A. Vetter, G. Jovicic, M. Batentschuk, and C. Brabec, "Temperature measurements using yag: Dy and yag: Sm under diode laser excitation (405 nm)," *Measurement Science and Technology*, vol. 26, no. 7, p. 075202, 2015.

[134] J. I. Eldridge, T. P. Jenkins, S. W. Allison, S. Cruzen, J. Condevaux, J. Senk, and A. Paul, "Real-time thermographic-phosphor-based temperature measurements of thermal barrier coating surfaces subjected to a high-velocity combustor burner environment," 2011.

[135] A. Rabhiou, A. Kempf, and A. Heyes, "Examination of eu-doped thermographic phosphors for surface temperature measurements," in *European Combustion Meeting, Vienna, Austria*. Citeseer, 2009.

[136] M. D. Dramićanin, "Sensing temperature via downshifting emissions of lanthanide-doped metal oxides and salts. a review," *Methods and applications in fluorescence*, vol. 4, no. 4, p. 042001, 2016.

[137] J. Feist, P. Sollazzo, S. Berthier, B. Charnley, and J. Wells, "Precision temperature detection using a phosphorescence sensor coating system on a rolls-royce viper engine," in *ASME Turbo Expo 2012: Turbine Technical Conference and Exposition*. American Society of Mechanical Engineers, 2012, pp. 917–926.

[138] A. Khalid and K. Kontis, "Quantum efficiencies, absolute intensities and signal-to-blackbody ratios of high-temperature laser-induced thermographic phosphors," *Luminescence*, vol. 26, no. 6, pp. 640–649, 2011.

[139] K.-Y. Ko, Y. K. Lee, H. K. Park, Y.-C. Kim, and Y. R. Do, "The variation of the enhanced photoluminescence efficiency of y 2 o 3: Eu 3+ films with the thickness to the photonic crystal layer," *Optics express*, vol. 16, no. 8, pp. 5689–5696, 2008.

[140] J. Brübach, A. Dreizler, and J. Janicka, "Gas compositional and pressure effects on thermographic phosphor thermometry," *Measurement Science and Technology*, vol. 18, no. 3, p. 764, 2007.

[141] M. Chambers and D. Clarke, "Doped oxides for high-temperature luminescence and lifetime thermometry," *Annual Review of Materials Research*, vol. 39, pp. 325–359, 2009.

[142] Y. Shen and D. R. Clarke, "Effects of reducing atmosphere on the luminescence of eu3+-doped yttria-stabilized zirconia sensor layers in thermal barrier coatings," *Journal of the American Ceramic Society*, vol. 92, no. 1, pp. 125–129, 2009.

[143] S. AMIEL, E. COPIN, T. SENTENAC, Y. LE MAOULT, and P. LOURS, "Caractérisation de marqueurs photoluminescents de lhistoire thermique."

[144] J. Feist and A. Heyes, "Europium-doped yttria-stabilized zirconia for high-temperature phosphor thermometry," *Proceedings of the Institution of Mechanical Engineers, Part L: Journal of Materials: Design and Applications*, vol. 214, no. 1, pp. 7–12, 2000.

[145] D. Peng, L. Yang, T. Cai, Y. Liu, X. Zhao, and Z. Yao, "Phosphor-doped thermal barrier coatings deposited by air plasma spray for in-depth temperature sensing," *Sensors*, vol. 16, no. 10, p. 1490, 2016.

[146] X. Chen, Z. Mutasim, J. Price, J. Feist, A. Heyes, and S. Seefeldt, "Industrial sensor tbcs: Studies on temperature detection and durability," *International Journal of Applied Ceramic Technology*, vol. 2, no. 5, pp. 414–421, 2005.

[147] L. Pin, C. Pilgrim, J. Feist, Y. Le Maoult, F. Ansart, and P. Lours, "Characterisation of thermal barrier sensor coatings synthesised by sol–gel route," *Sensors and Actuators A: Physical*, vol. 199, pp. 289–296, 2013.

[148] Y. Shen, X. Wang, H. He, Y. Lin, and C.-W. Nan, "Effects of sm3+ doping on the temperature-dependent fluorescence intensity ratio of er3+, sm3+-co doped-yttria stabilized zirconia," *Journal of Alloys and Compounds*, vol. 536, pp. 161–165, 2012.

[149] M. Chambers and D. Clarke, "Terbium as an alternative for luminescence sensing of temperature of thermal barrier coating materials," *Surface and Coatings Technology*, vol. 202, no. 4-7, pp. 688–692, 2007.

[150] E. Copin, "Fonctionnalisation de barrières thermiques aéronautiques ysz issues de la voie sol-gel: mesure de température et diagnostic de l'endommagement par fluorescence," Ph.D. dissertation, Ecole des Mines d'Albi-Carmaux, 2015.

[151] E. Nakazawa, S. Shionoya, and W. Yen, "Phosphor handbook," *CRC Press, Boca Raton, Boston, London, New York, Washington, DC*, p. 102, 1999.

[152] P. D. Johnson and F. E. Williams, "The interpretation of the dependence of luminescent efficiency on activator concentration," *The Journal of Chemical Physics*, vol. 18, no. 11, pp. 1477–1483, 1950.

[153] ——, "Specific magnetic susceptibilities and related properties of manganese-activated zinc fluoride," *The Journal of Chemical Physics*, vol. 18, no. 3, pp. 323–326, 1950.

[154] M. Gentleman and D. Clarke, "Embedded optical sensors for thermal barrier coatings," *Technical Report 2004-12-16*, 2004.

[155] H. Yu, Z. Sumei, X. Jiaying, Z. Ling, Z. Xin, Z. Binglin, W. Ying, and C. Xueqiang, "Doping concentration of eu3+ as a fluorescence probe for phase transformation of zirconia," *Journal of Rare Earths*, vol. 33, no. 7, pp. 717–725, 2015.

[156] V. M. Bekale, A.-M. Huntz, C. Legros, G. Sattonnay, and F. Jomard, "Impurity diffusion of cerium and gadolinium in single-and polycrystalline yttria-stabilized zirconia," *Philosophical Magazine*, vol. 88, no. 1, pp. 1–19, 2008.

[157] B. Good, "Kinetic monte carlo simulation of oxygen and cation diffusion in yttria-stabilized zirconia," 2011.

[158] P. Kubelka, "New contributions to the optics of intensely light-scattering materials. part i," *JOSA*, vol. 38, no. 5, pp. 448–457, 1948.

[159] ——, "New contributions to the optics of intensely light-scattering materials. part ii: Nonhomogeneous layers," *JOSA*, vol. 44, no. 4, pp. 330–335, 1954.

[160] C. Sandoval and A. D. Kim, "Extending generalized Kubelka–Munk to three-dimensional radiative transfer," *Applied Optics*, vol. 54, no. 23, pp. 7045–7053, 2015.

[161] M. L. Myrick, M. N. Simcock, M. Baranowski, H. Brooke, S. L. Morgan, and J. N. McCutcheon, "The kubelka-munk diffuse reflectance formula revisited," *Applied Spectroscopy Reviews*, vol. 46, no. 2, pp. 140–165, 2011.

[162] S. Mourad, "Improved calibration of optical characteristics of paper by an adapted paper-mtf model," *Journal of Imaging Science and Technology*, vol. 51, no. 4, pp. 283–292, 2007.

[163] S. Mazauric, M. Hébert, L. Simonot, and T. Fournel, "Two-flux transfer matrix model for predicting the reflectance and transmittance of duplex halftone prints," *JOSA A*, vol. 31, no. 12, pp. 2775–2788, 2014.

[164] J. D. Kruschwitz and R. S. Berns, "First-order goniospectrophotometric spectral modeling of isotropic and anisotropic colorant mixtures," *Applied Optics*, vol. 53, no. 4, pp. A131–A141, 2014.

[165] M. Seyfried and L. Fukshansky, "Light gradients in plant tissue," *Applied Optics*, vol. 22, no. 9, pp. 1402–1408, 1983.

[166] D. Yudovsky and A. J. Durkin, "Hybrid diffusion and two-flux approximation for multilayered tissue light propagation modeling," *Applied Optics*, vol. 50, no. 21, pp. 4237–4245, 2011.

[167] S. Janchaysang, S. Sumriddetchkajorn, and P. Buranasiri, "Tunable filter-based multispectral imaging for detection of blood stains on construction material substrates. part 1. developing blood stain discrimination criteria," *Applied Optics*, vol. 51, no. 29, pp. 6984–6996, 2012.

[168] J. P. Feist and A. L. Heyes, "Photo-stimulated phosphorescence for thermal condition monitoring and nondestructive evaluation in thermal barrier coatings," *Heat Transfer Engineering*, vol. 30, no. 13, pp. 1087–1095, 2009.

[169] L. Rossmann, M. Northam, B. Sarley, L. Chernova, V. Viswanathan, B. Harder, and S. Raghavan, "Investigation of tgo stress in thermally cycled plasma-spray physical vapor deposition and electron-beam physical vapor deposition thermal barrier

coatings via photoluminescence spectroscopy," *Surface and Coatings Technology*, p. 125047, 2019.

[170] J. Peelen and R. Metselaar, "Light scattering by pores in polycrystalline materials: Transmission properties of alumina," *Journal of Applied Physics*, vol. 45, no. 1, pp. 216–220, 1974.

[171] E. R. Dobrovinskaya, L. A. Lytvynov, and V. Pishchik, "Properties of sapphire," in *Sapphire*. Springer, 2009, pp. 55–176.

[172] M. Bacos, J. Dorvaux, O. Lavigne, R. Mévrel, M. Poulain, C. Rio, and M. Vidal-Setif, "Performance and degradation mechanisms of thermal barrier coatings for turbine blades: a review of onera activities," *AerospaceLab*, vol. 3, pp. p–1, 2011.

[173] C. C. Pilgrim, P. Y. Sollazzo, S. Berthier, J. P. Feist, S. K. Biswas, and J. R. Nicholls, "Thermal barrier sensor coatings - sensing damage and ageing in critical components," in *IET ISA 60th International Instrumentation Symposium 2014*, June 2014, pp. 1–8.

[174] Y. Lee, J. Chang, S. Das, A. Dhar, M. Pal, M. C. Paul, J. Lin, and Y. Jhang, "Er^{3+}-doped nanoengineered yttria-stabilized zirconia alumino-silicate fiber for efficient cw and mode-locked laser operation," *IEEE Photonics Journal*, vol. 8, no. 4, pp. 1–13, 2016.

[175] D. Ramteke, A. Balakrishna, V. Kumar, and H. Swart, "Luminescence dynamics and investigation of judd-ofelt intensity parameters of Sm^{3+} ion containing glasses," *Optical Materials*, vol. 64, pp. 171–178, 2017.

[176] J. I. Eldridge, C. M. Spuckler, and R. E. Martin, "Monitoring delamination progression in thermal barrier coatings by mid-infrared reflectance imaging," *International journal of applied ceramic technology*, vol. 3, no. 2, pp. 94–104, 2006.

[177] J. I. Eldridge, D. Zhu, and D. E. Wolfe, "Monitoring delamination of thermal barrier coatings during interrupted high-heat-flux laser testing using luminescence imaging," 2011.

[178] C. Li, X. Fan, P. Jiang, and X. Jin, "Delamination-indicating of atmosphere-plasma-sprayed thermal barrier coating system using eu 3+ luminescence mapping," *Materials Letters*, 2018.

[179] J. I. Eldridge and T. J. Bencic, "Monitoring delamination of plasma-sprayed thermal barrier coatings by reflectance-enhanced luminescence," *Surface and Coatings Technology*, vol. 201, no. 7, pp. 3926–3930, 2006.

[180] J. I. Eldridge and D. E. Wolfe, "Monitoring thermal barrier coating delamination progression by upconversion luminescence imaging," *Surface and Coatings Technology*, p. 124923, 2019.

[181] J. I. Eldridge, J. Singh, and D. E. Wolfe, "Erosion-indicating thermal barrier coatings using luminescent sublayers," *Journal of the American Ceramic Society*, vol. 89, no. 10, pp. 3252–3254, 2006.

[182] J. I. Eldridge, "Optical diagnostics for high-temperature thermal barrier coatings," 2009.

[183] *Progress in Thermal Barrier Coatings*, ser. Progress in Ceramic Technology. Wiley, 2009. [Online]. Available: https://books.google.com/books?id=p-uhDwAAQBAJ

[184] J. I. Eldridge, T. J. Bencic, C. M. Spuckler, J. Singh, and D. E. Wolfe, "Delamination-indicating thermal barrier coatings using ysz: Eu sublayers," *Journal of the American Ceramic Society*, vol. 89, no. 10, pp. 3246–3251, 2006.

[185] R. Siegel and J. R. Howell, *Thermal Radiation Heat Transfer, 4th Edition*. Taylor & Francis, New York, 2002.

[186] C. Spuckler and R. Siegel, "Refractive index and scattering effects on radiative behavior of a semitransparent layer," *Journal of Thermophysics and Heat transfer*, vol. 7, no. 2, pp. 302–310, 1993.

[187] I. Hanhan, E. Durnberg, G. Freihofer, P. Akin, and S. Raghavan, "Portable piezospectroscopy system: non-contact in-situ stress sensing through high resolution photo-luminescent mapping," *Journal of Instrumentation*, vol. 9, no. 11, p. P11005, 2014.

[188] A. Manero II, A. Selimov, Q. Fouliard, K. Knipe, J. Wischek, C. Meid, A. M. Karlsson, M. Bartsch, and S. Raghavan, "Piezospectroscopic evaluation and damage identification for thermal barrier coatings subjected to simulated engine environments," *Surface and Coatings Technology*, vol. 323, pp. 30–38, 2017.

[189] R. Esteves, R. Hoover, K. Vo, S. Jahan, S. Haldar, and S. Raghavan, "Application of stress sensing coatings on metal substrates with a sub-surface notch," in *AIAA Scitech 2019 Forum*, 2019.

[190] R. Esteves, J. Hernandez, K. Vo, R. Hoover, G. Freihofer, and S. Raghavan, "Measurements for stress sensing of composites using tailored piezospectroscopic coatings," *AIP Advances*, vol. 9, no. 5, p. 055201, 2019.

[191] A. Stevenson, A. Jones, and S. Raghavan, "Stress-sensing nanomaterial calibrated with photostimulated luminescence emission," *Nano letters*, vol. 11, no. 8, pp. 3274–3278, 2011.

[192] G. Freihofer, J. Dustin, H. Tat, A. Schülzgen, and S. Raghavan, "Stress and structural damage sensing piezospectroscopic coatings validated with digital image correlation," *Aip Advances*, vol. 5, no. 3, p. 037139, 2015.

[193] A. Stevenson, A. Jones, and S. Raghavan, "Characterization of particle dispersion and volume fraction in alumina-filled epoxy nanocomposites using photostimulated luminescence spectroscopy," *Polymer journal*, vol. 43, no. 11, p. 923, 2011.

[194] G. Freihofer, D. Fugon-Dessources, E. Ergin, A. Van Newkirk, A. Gupta, S. Seal, A. Schulzgen, and S. Raghavan, "Piezospectroscopic measurements capturing the evolution of plasma spray-coating stresses with substrate loads," *ACS applied materials & interfaces*, vol. 6, no. 3, pp. 1366–1369, 2014.

[195] I. Hanhan, A. Selimov, D. Carolan, A. C. Taylor, and S. Raghavan, "Quantifying alumina nanoparticle dispersion in hybrid carbon fiber composites using photoluminescent spectroscopy," *Applied spectroscopy*, vol. 71, no. 2, pp. 258–266, 2017.

[196] I. Hanhan, A. P. Selimov, D. Carolan, A. Taylor, and S. Raghavan, "Characterizing mechanical properties of hybrid alumina carbon fiber composites with piezospectroscopy," in *57th AIAA/ASCE/AHS/ASC Structures, Structural Dynamics, and Materials Conference*, 2016, p. 1413.

[197] G. Freihofer, A. Schülzgen, and S. Raghavan, "Damage mapping with a degrading elastic modulus using piezospectroscopic coatings," *NDT & E International*, vol. 75, pp. 65–71, 2015.

[198] J. Kimmel, Z. Mutasim, and W. Brentnall, "Effects of alloy composition on the performance of yttria stabilized zirconia-thermal barrier coatings," *Transactions of*

the ASME-A-Engineering for Gas Turbines and Power, vol. 122, no. 3, pp. 393–400, 2000.

[199] C. C. Pilgrim, "Luminescence for the non-destructive evaluation of thermal barrier coatings," 2014.

[200] C. Weyant, J. Almer, and K. Faber, "Through-thickness determination of phase composition and residual stresses in thermal barrier coatings using high-energy x-rays," *Acta materialia*, vol. 58, no. 3, pp. 943–951, 2010.

[201] J. Thornton, S. Slater, and J. Almer, "The measurement of residual strains within thermal barrier coatings using high-energy x-ray diffraction," *Journal of the American Ceramic Society*, vol. 88, no. 10, pp. 2817–2825, 2005.

[202] X. Liu, T. Wang, C. Li, Z. Zheng, and Q. Li, "Microstructural evolution and growth kinetics of thermally grown oxides in plasma sprayed thermal barrier coatings," *Progress in Natural Science: Materials International*, vol. 26, no. 1, pp. 103–111, 2016.

[203] C. Eckert, C. Pflitsch, and B. Atakan, "Sol–gel deposition of multiply doped thermographic phosphor coatings al2o3:(cr3+, m3+)(m= dy, tm) for wide range surface temperature measurement application," *Progress in Organic Coatings*, vol. 68, no. 1-2, pp. 126–129, 2010.

[204] R. Darolia, "Thermal barrier coatings technology: critical review, progress update, remaining challenges and prospects," *International materials reviews*, vol. 58, no. 6, pp. 315–348, 2013.

[205] S. Allison and G. Gillies, "Remote thermometry with thermographic phosphors: Instrumentation and applications," *Review of Scientific Instruments*, vol. 68, no. 7, pp. 2615–2650, 1997.

[206] J. I. Eldridge, T. J. Bencic, S. W. Allison, and D. L. Beshears, "Depth-selective diagnostics of thermal barrier coatings incorporating thermographic phosphors," 2003.

[207] A. Heyes, J. Feist, X. Chen, Z. Mutasim, and J. Nicholls, "Optical nondestructive condition monitoring of thermal barrier coatings," *Journal of Engineering for Gas Turbines and Power*, vol. 130, no. 6, p. 061301, 2008.

[208] J. R. Nicholls, R. G. Wellman, R. Steenbakker, and J. Feist, "Self diagnostic eb-pvd thermal barrier coatings," in *Advances in Science and Technology*, vol. 72. Trans Tech Publ, 2010, pp. 65–74.

[209] M. Chambers and D. R. Clarke, "Effect of long term, high temperature aging on luminescence from eu-doped ysz thermal barrier coatings," *Surface and coatings technology*, vol. 201, no. 7, pp. 3942–3946, 2006.

[210] S. Amiel, E. Copin, T. Sentenac, P. Lours, and Y. Le Maoult, "On the thermal sensitivity and resolution of a ysz: Er3+/ysz: Eu3+ fluorescent thermal history sensor," *Sensors and Actuators A: Physical*, vol. 272, pp. 42–52, 2018.

[211] E. Copin, X. Massol, S. Amiel, T. Sentenac, Y. Le Maoult, and P. Lours, "Novel erbia-yttria co-doped zirconia fluorescent thermal history sensor," *Smart Materials and Structures*, vol. 26, no. 1, p. 015001, 2016.

[212] M. D. Rabasović, B. D. Murić, V. Čelebonović, M. Mitrić, B. M. Jelenković, and M. G. Nikolić, "Luminescence thermometry via the two-dopant intensity ratio of y2o3: Er3+, eu3+," *Journal of Physics D: Applied Physics*, vol. 49, no. 48, p. 485104, 2016.

[213] Q. Fouliard, J. Hernandez, B. Heeg, R. Ghosh, and S. Raghavan, "Phosphor thermometry instrumentation for synchronized acquisition of luminescence lifetime decay and intensity on thermal barrier coatings," *(In Review)*.

[214] H. Seat and J. Sharp, "Dedicated temperature sensing with c-axis oriented single-crystal ruby (cr/sup 3+: Al/sub 2/o/sub 3/) fibers: temperature and strain dependences of r-line fluorescence," *IEEE Transactions on Instrumentation and Measurement*, vol. 53, no. 1, pp. 140–154, 2004.

[215] J. Davies, *Conduction and induction heating*. IET, 1990, no. 11.

[216] L. González-Fernández, L. Del Campo, R. Pérez-Sáez, and M. Tello, "Normal spectral emittance of inconel 718 aeronautical alloy coated with yttria stabilized zirconia films," *Journal of Alloys and Compounds*, vol. 513, pp. 101–106, 2012.

[217] J. Markham and K. Kinsella, "Thermal radiative properties and temperature measurement from turbine coatings," *International journal of thermophysics*, vol. 19, no. 2, pp. 537–545, 1998.

[218] J. Manara, M. Zipf, T. Stark, M. Arduini, H.-P. Ebert, A. Tutschke, A. Hallam, J. Hanspal, M. Langley, D. Hodge *et al.*, "Long wavelength infrared radiation thermometry for non-contact temperature measurements in gas turbines," *Infrared Physics & Technology*, vol. 80, pp. 120–130, 2017.

[219] H. Kusama, O. J. Sovers, and T. Yoshioka, "Line shift method for phosphor temperature measurements," *Japanese Journal of Applied Physics*, vol. 15, no. 12, p. 2349, 1976.

[220] T. Cai, Y. Li, S. Guo, D. Peng, X. Zhao, and Y. Liu, "Pressure effect on phosphor thermometry using mg4fgeo6: Mn," *Measurement Science and Technology*, vol. 30, no. 2, p. 027001, 2019.

[221] R. Diaz, M. Mossaddad, A. Bozan, S. Raghavan, J. Almer, J. Okasinski, H. Palaez-Perez, and P. Imbrie, "In-situ strain measurements of eb-pvd thermal barrier coatings using synchrotron x-ray diffraction under thermo-mechanical loading," in *49th AIAA Aerospace Sciences Meeting including the New Horizons Forum and Aerospace Exposition*, 2011, p. 500.

[222] A. Manero, S. Sofronsky, K. Knipe, C. Meid, J. Wischek, J. Okasinski, J. Almer, A. M. Karlsson, S. Raghavan, and M. Bartsch, "Monitoring local strain in a thermal barrier coating system under thermal mechanical gas turbine operating conditions," *JOM*, vol. 67, no. 7, pp. 1528–1539, 2015.

[223] K. Knipe, A. Manero II, S. F. Siddiqui, C. Meid, J. Wischek, J. Okasinski, J. Almer, A. M. Karlsson, M. Bartsch, and S. Raghavan, "Strain response of thermal barrier coatings captured under extreme engine environments through synchrotron x-ray diffraction," *Nature communications*, vol. 5, p. 4559, 2014.

[224] V. Kumar and K. Balasubramanian, "Progress update on failure mechanisms of advanced thermal barrier coatings: a review," *Progress in Organic Coatings*, vol. 90, pp. 54–82, 2016.

[225] B. B. He, *Two-dimensional X-ray diffraction*. Wiley Online Library, 2009, vol. 2.

[226] J. Matejicek and S. Sampath, "In situ measurement of residual stresses and elastic moduli in thermal sprayed coatings: Part 1: apparatus and analysis," *Acta Materialia*, vol. 51, no. 3, pp. 863–872, 2003.

[227] J. Matejicek, S. Sampath, D. Gilmore, and R. Neiser, "In situ measurement of residual stresses and elastic moduli in thermal sprayed coatings: Part 2: processing effects on properties of mo coatings," *Acta Materialia*, vol. 51, no. 3, pp. 873–885, 2003.

[228] K. Knipe, I. Manero, S. F. Siddiqui, C. Meid, J. Wischek, J. Okasinski, J. Almer, A. M. Karlsson, M. Bartsch, S. Raghavan *et al.*, "Inside the engine environment–

synchrotrons reveal secrets of high-temperature ceramic coatings," *American Ceramic Society Bulletin*, vol. 94, no. 1, p. 22, 2015.

[229] C. Li, S. Jacques, Y. Chen, P. Xiao, A. Beale, M. di Michiel, N. Markossan, P. Nylen, and R. Cernik, "Precise strain profile measurement as a function of depth in thermal barrier coatings using high energy synchrotron x-rays," *Scripta Materialia*, vol. 113, pp. 122–126, 2016.

[230] J. A. Krogstad, M. Lepple, Y. Gao, D. M. Lipkin, and C. G. Levi, "Effect of yttria content on the zirconia unit cell parameters," *Journal of the American Ceramic Society*, vol. 94, no. 12, pp. 4548–4555, 2011.

[231] A. Hammersley, "Fit2d v9. 129 reference manual v3. 1," *Inter Rep ESRF98HA01, ESRF, Grenoble*, 1998.

[232] A. Hammersley, S. Svensson, and A. Thompson, "Calibration and correction of spatial distortions in 2d detector systems," *Nuclear Instruments and Methods in Physics Research Section A: Accelerators, Spectrometers, Detectors and Associated Equipment*, vol. 346, no. 1-2, pp. 312–321, 1994.

[233] A. Lunt, M. Xie, N. Baimpas, S. Zhang, S. Kabra, J. Kelleher, T. Neo, and A. Korsunsky, "Calculations of single crystal elastic constants for yttria partially stabilised zirconia from powder diffraction data," *Journal of Applied Physics*, vol. 116, no. 5, p. 053509, 2014.

[234] J. Almer, U. Lienert, R. L. Peng, C. Schlauer, and M. Odén, "Strain and texture analysis of coatings using high-energy x-rays," *Journal of applied physics*, vol. 94, no. 1, pp. 697–702, 2003.

[235] T. Manns and B. Scholtes, "Deccalc-a program for the calculation of diffraction elastic constants from single crystal coefficients," in *Materials Science Forum*, vol. 681. Trans Tech Publ, 2011, pp. 417–419.

[236] J. Matejicek, S. Sampath, P. Brand, and H. Prask, "Quenching, thermal and residual stress in plasma sprayed deposits: Nicraly and ysz coatings," *Acta Materialia*, vol. 47, no. 2, pp. 607–617, 1999.

[237] S. Karthikeyan, V. Balasubramanian, and R. Rajendran, "Developing empirical relationships to estimate porosity and microhardness of plasma-sprayed ysz coatings," *Ceramics International*, vol. 40, no. 2, pp. 3171–3183, 2014.

[238] L. Qu and K.-L. Choy, "Thermophysical and thermochemical properties of new thermal barrier materials based on dy2o3–y2o3 co-doped zirconia," *Ceramics International*, vol. 40, no. 8, pp. 11 593–11 599, 2014.

[239] L. Qu, K.-L. Choy, and R. Wheatley, "Theoretical and experimental studies of doping effects on thermodynamic properties of (dy, y)-zro2," *Acta Materialia*, vol. 114, pp. 7–14, 2016.